UNIVERSITÀ DEGLI STUDI DI PALERMO
Energia e Tecnologie dell'Informazione
Dipartimento di Energia, Ingegneria dell'Informazione e modelli Matematici (DEIM)
ING-IND/33

DESIGN OF A FAULT AND PARTIAL DISCHARGES LOCATION DEVICE FOR CABLE POWER NETWORK

IL DOTTORE
VINCENZO LI VIGNI

IL COORDINATORE
MARIA STELLA MONGIOVÌ

IL TUTOR
ELEONORA RIVA SANSEVERINO

IL CO TUTOR
ROBERTO CANDELA

CICLO XXIX
2017

A mia nonna Lena.

Contents

List of Figures

List of Tables

Abstract

In this thesis, a digital device for fault and on line partial discharge location is presented. The device employs the traveling wave method for two or multiple ends. The designed prototype shows interesting features connected to the low cost and to the possibility to collect data from different locations thus providing additional functionalities deriving from pre-fault and data analysis, relating the existence of defects to the subsequent fault event. The device also enables the acquisition of the temperature on the cable section where the sensor is installed.

Such installation can also support DSO and TSO for carrying out both on-event and condition based maintenance, discovering the causality between pre-fault condition and fault condition, thus strongly reducing costs and increasing the quality of supplied service.

Acknowledgments

Many people deserve my sincere gratitude for this thesis. First of all, I would like to thank my tutor, Prof. Eleonora Riva Sanseverino. This PhD could not be possible without her endless patience, support and precious advices.

Roberto Candela deserves special thanks for being such an inspirational boss. I have learned a lot from him and there is still more to learn - probably I will never stop.

I owe Antonio Di Stefano a large debt of gratitude for providing his uncountable experience and much appreciated help.

Giuseppe Fiscelli thinks he did not help during this thesis but he is wrong. His name deserves a place here.

I cannot forget Stefano Franchi, Ivan Troia, Simone Giannini, Pietro Romano, Antonino Madonia, Giuseppe Presti. Thank you gentlemen!

Thanks to Eng. Giovanni Filippone, Giuseppe Gennusa and Angelo Castiglione of Terna Rete Italia Spa, for their contribution in carrying out the measurements on the plants.

I thank my family who has always given me unconditional love, encouraging and supporting me in every aspect. Grazie mamma, papà, Ale.

Thanks Ornella for supporting me. Even when the Sicilian sun was shining (very often of course) and I had to study, she never complained. Thanks for all that you are.

This PhD was supported by Prysmian Electronics.

Introduction

With the increasing growth in complexity and size of power transmission and distributions networks, electric utilities must put efforts into handling failure related problems. When a failure in the electric network occurs, the cause of the fault shall be understood and the faulty part localized and disconnected from the rest of the grid. In fact, generally a set of protection relays and switches automatically isolate the faulty section of line and safely restore its functionality. The utility should also locate the position of the fault along the line in order to minimize the outage time thus avoiding to negatively affect service reliability. At the same time, effective ways for estimating the health status of the power system before a defect may eventually become a permanent fault already exist. Condition based maintenance allows to asses the power system via a set of indicators which suggest the corrective actions to be performed. Those indicator can be extracted by performing specific measurements on the system. One of the more consolidated methods for assessing power accessories consists in performing partial discharges measurements.

In this thesis, a digital device for fault and on line partial discharge location is presented. The device employs the traveling wave method for two or multiple ends. The designed prototype shows interesting features connected to the low cost and to the possibility to collect data from different locations thus providing additional functionalities deriving from pre-fault and data analysis, relating the existence of defects to the subsequent fault event. The device also enables the acquisition of the temperature on the cable section where the sensor is installed.

Such installation can also support DSO and TSO for carrying out both on-event and condition based maintenance, discovering the causality between pre-fault condition and fault condition, thus strongly reducing costs and increasing the quality of supplied service.

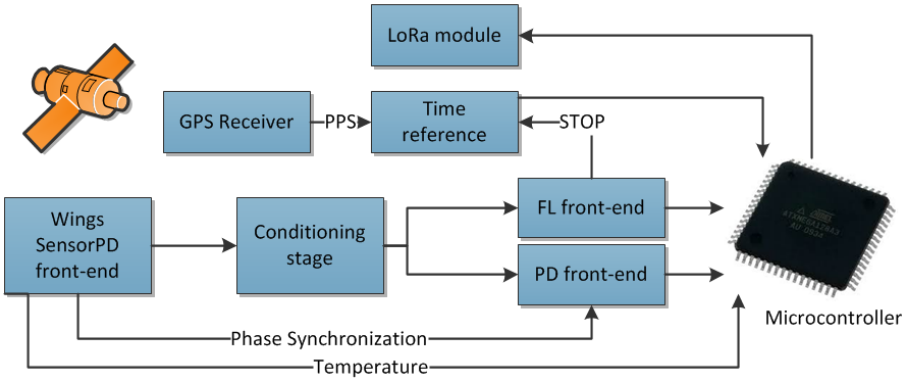

(a)

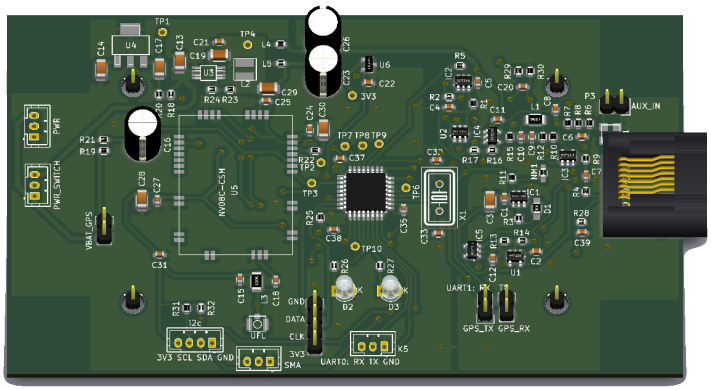

(b)

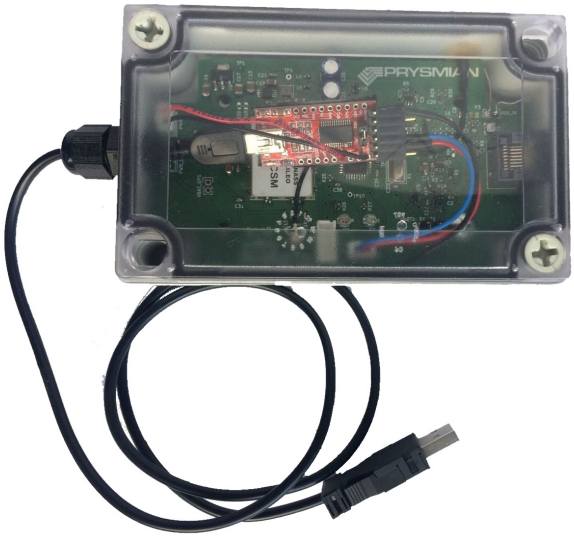

(c)

Figure 1: Block diagram (a), rendering (b) and final realization (c) of the presented device.

Chapter 1

Fault-location techniques

A big difference exists between FL devices and protective relays in terms of their main functionality. In the first case, the aim is to provide an exact point of the fault, while in the second case, the aim is to provide safe operation for people and for apparatus connected to the network.

Fault Location, FL, devices have different requirements compared to fault detection ones [1, 2], in fact:

- a few milliseconds are requested to protective relays for detecting the fault and tripping, while FL devices do not have so strict time requirements and may use more accurate and slower algorithms for performing their task;
- in FL devices, digital filtering on the acquired voltage and current may be used; on the contrary this would add undesired delay on fault detection relays operation;
- FL devices should be as accurate as possible in order to give precise information to the utility for finding the right line section to carry out the reparation, while protective relays must roughly determine if the fault is in a certain zone and, if required, interrupt its supply accordingly to the selectivity of the protection system;
- with FL devices, data can be transmitted to centralized servers for a better analysis of the fault condition and a better estimation of its location.

It should be noted that in some cases, microprocessor fault detection devices also include fault location functionalities. Extensive reviews regarding FL methods are available in the literature such as in [3, 4, 2].

1.1 Fault location methods classification

FL devices process voltage and current waveforms in order to obtain an accurate estimation of the fault position along the line. This process is usually automatically performed by the FL system. The main methodologies for performing this task are:

1. impedance-based techniques;
2. traveling-wave techniques;

Depending from the point of the line at which the line voltage and current waveforms are acquired, FL methods may be categorized in:

1. one-end (single-end) methods;
2. two-end (double-end) methods;
3. multi-end and wide area methods.

Indeed, with one-end methods, only data from one terminal of the electric line are available, while with double-end methods data from both sides of the line are used. In the multi-end case, data is acquired in multiple points of the transmission or distribution line [3, 5, 6]. Synchronized or unsynchronized samples or phasor measurements can be used for double and multi-end techniques.

Furthermore, it is important to distinguish between FL methods designed for transmission and those dedicated to distribution lines; the differences of the two types of networks usually do not allow to use the method without important changes to the FL method.

1.2 Impedance-based methods

These methods use fundamental-frequency voltage and current waveforms acquired at the line ends during the fault and calculate the impedance of the faulted-line segment to obtain the position of the fault. Essentially, impedance-based methods rely on measurements of post-fault line impedance as time-domain samples or phasors [3, 6, 7, 8, 9].

Impedance-based methods also require lumped parameters model of the line [4]. These methods are in some cases simple and economical and may be integrated into some protective relays. The position of the fault is usually estimated with respect of the total impedance of the line, under the assumption that the electric line is homogeneous (generally true for transmission lines).

1.2.1 One-end methods

Simple reactance method

This FL method is introduced with respect to the simplified case of a single-phase line with power source connected at one end only. In Fig. 1.1, the schematic of such line is shown. In the specific, the single-phase line A-B has a power source in A. Lumped-line model without considering shunt capacitances is used in this discussion.

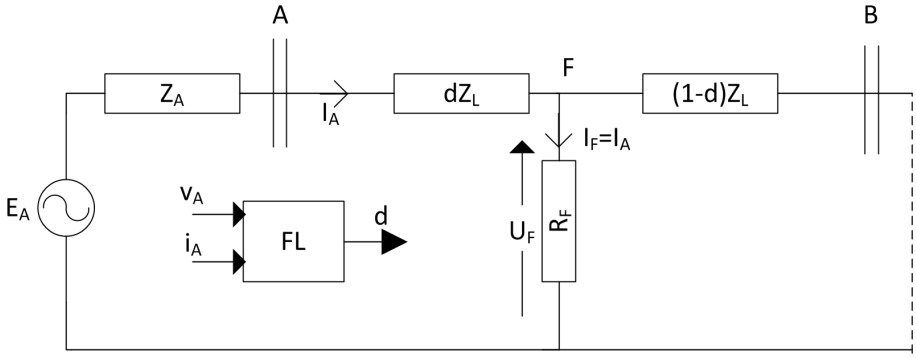

Figure 1.1: Analysis of impedance-based FL method for a single-phase line with source only at one end.

The distance between where the fault locator is installed (A) and the fault point (F) is unknown (d). To simplify the analysis, the charging current is neglected, so the current at the A end $\overline{I}_A$ is equal to the current at the fault $\overline{I}_F$. Under this assumption, one can calculate the impedance seen from the FL terminal $\overline{Z}_{FL}$ by the formula:

$$\overline{Z}_{FL} = \frac{\overline{U}_A}{\overline{I}_A} = d\overline{Z}_L + R_F \tag{1.1}$$

where:

$\overline{U}_A$ is the voltage at A terminal;

R_F is the fault resistance;

$\overline{Z}_L$ is the impedance per unit of length of the line.

The unknown distance to the fault is obtained by taking the imaginary part from (1.1):

$$d = \frac{\Im\{\overline{Z}_{FL}\}}{\Im\{\overline{Z}_L\}}$$

We assumed here that the fault impedance is a pure resistance. Actually, depending on the currents at the ends A and B, the fault impedance can be seen as pure resistance or as resistive and capacitive reactance or as resistive and inductive reactance. In the the last two cases, the contribution of the reactance of the fault impedance creates the reactance effect [1, 10, 6].

Takagi method

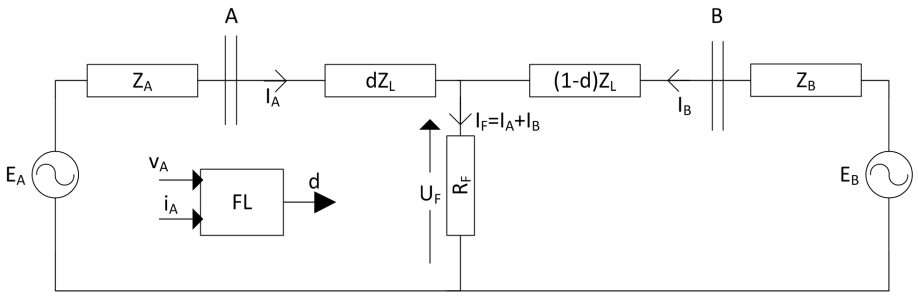

Figure 1.2: Analysis of impedance-based FL method for a single-phase line with two sources.

In the less simple case in which the line is fed by the two ends A and B (Fig. 1.2), in general $\overline{I}_A \neq \overline{I}_F$ since the source in B provides a current $\overline{I}_B$, hence $\overline{I}_F = \overline{I}_A + \overline{I}_B$. The FL system installed in A sees an impedance with a not-null reactance part, and so reactance error arises (Fig. 1.3).

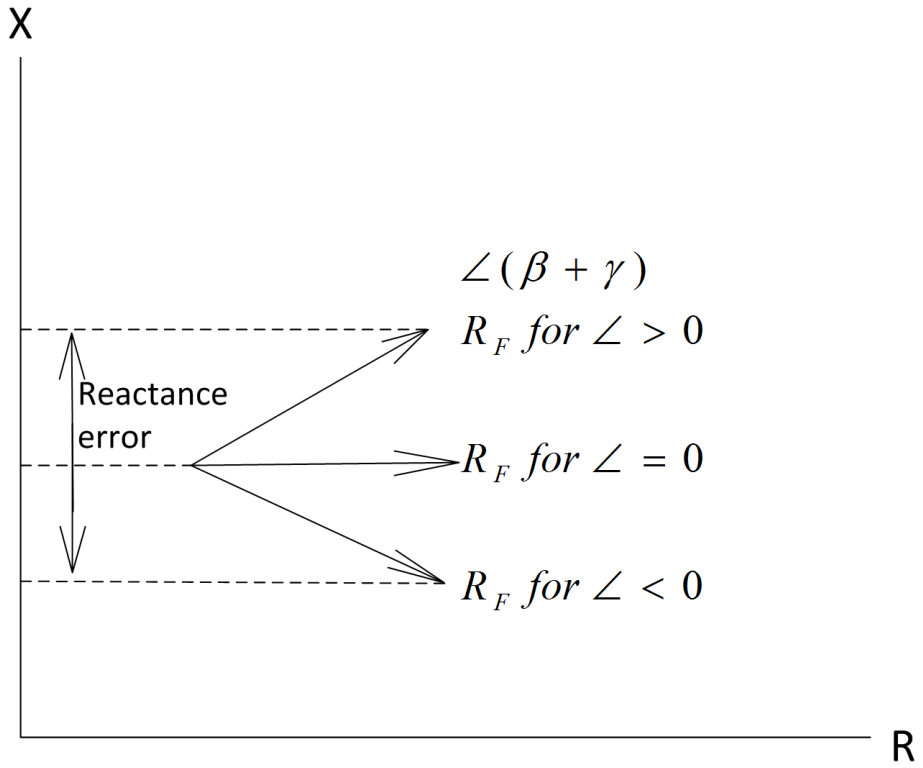

Figure 1.3: Reactance error.

In such cases, a two-end FL technique avoids the reactance error by acquiring also the required unknown current values ($\overline{I}_B$). On the other hand, it is advantageous to have simpler devices which do not require other communication link from the two ends of the line. In a classic work of the literature [11], Takagi *et al* separated the circuit shown in Fig. 1.2 into two equivalent circuits: the pre-fault network and the pure-fault network (Fig. 1.4). The idea is that the superimposition of the two networks generates the original starting one of the single phase circuit with a fault.

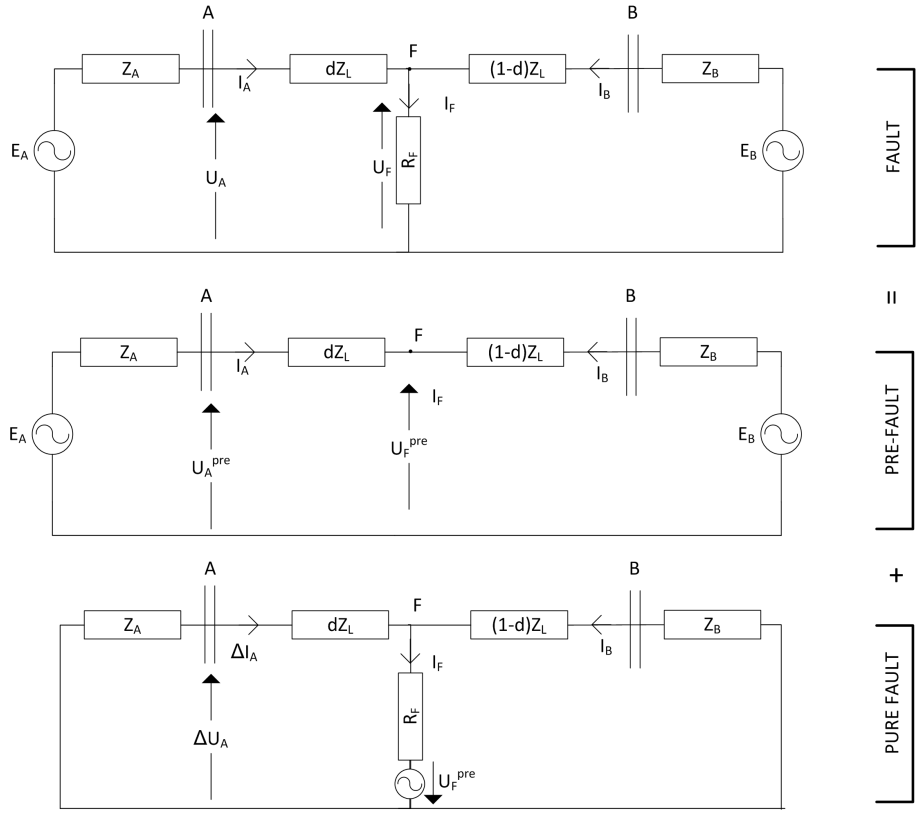

Figure 1.4: Equivalent circuit (top) during the fault which may be obtained by superimposition of pre-fault network (center) and pure fault equivalent network (bottom).

By following the mathematical discussion in [2] and [11], the distance d may be given by:

$$d = \frac{\Im\{\overline{U}\Delta\overline{I}_A^*\}}{\Im\{\overline{Z}_L\overline{I}_A\Delta\overline{I}_A^*\}} \tag{1.2}$$

where:

$$\Delta\overline{I}_A = \overline{I}_A - \overline{I}_A^{PRE} = \overline{k}_F\overline{I}_F \tag{1.3}$$

is the incremental current (in (1.2) appears as conjugate), obtained by the difference of the current in A, when the fault occurs, and the value of the pre-fault current in A. It is assumed that the load current is approximately the same before and during the fault.

$$\overline{k}_F = \frac{-d\overline{Z}_L + \overline{Z}_L + \overline{Z}_B}{\overline{Z}_A + \overline{Z}_L + \overline{Z}_B} \tag{1.4}$$

is the fault current distribution factor [1, 12, 13].

In (1.2) it was made the simplification that $\overline{k}_F$ is a real number, relying on the assumption that the impedances shown in (1.4) have approximately the same phases. The error in (1.2) depends on the degree of non-homogeneity of the line [8].

Modified Takagi method

When the pre-fault current is unknown, a modified Takagi method can be adopted for estimating the fault distance. In this method, the zero-sequence current $\overline{I}_{A0}$ is used in place of $\Delta\overline{I}_A$, considering the system load in a single line-to-ground fault [8, 14, 15]. In fact, in a ground fault, $\overline{I}_{G0}$ is close to $\Delta\overline{I}_G$ and virtually equal to zero ($\overline{I}_{G0} = 0$) in balanced operating conditions. The distance d is thus given by:

$$d = \frac{\Im\{\overline{U}_A 3\overline{I}^*_{G0}\}}{\Im\{\overline{Z}_L \overline{I}_A 3\overline{I}^*_{G0}\}} \tag{1.5}$$

while the current distribution factor is:

$$k_s = |k_s|\, e^{-j\gamma} = \frac{\overline{Z}_{G0} + \overline{Z}_{L0} + \overline{Z}_{B0}}{(1-d)\overline{Z}_{L0} + \overline{Z}_{B0}} \tag{1.6}$$

where γ is the degree of non-homogeneity. Applying $e^{-j\beta}$ to 1.5 improves the accuracy of the estimation, by forcing the system to be homogeneous. The modified Takagi method first calculates d through 1.5 and then this value is used for obtaining γ in the 1.6. The final expression of the fault distance takes into account load and system non-homogeneity:

$$d = \frac{\Im\{\overline{U}_A 3\overline{I}^*_{G0} e^{-j\beta}\}}{\Im\{\overline{Z}_L \overline{I}_A 3\overline{I}^*_{G0} e^{-j\beta}\}} \tag{1.7}$$

This method can be very accurate as long the source impedance parameters are well known. An estimation of the zero-sequence impedance of the local source can be calculated as $\overline{Z}_A = -\frac{\overline{U}_{A0}}{\overline{I}_{A0}}$, but $\overline{Z}_B$ must be known.

1.3 Traveling-wave methods

Traveling-wave (TW) methods have the high advantage, compared to impedance based FL methods, to be generally insensitive with respect to load conditions, high

ground resistance, fault resistance, fault type, fault inception phase angle and power system source configuration; at the same time they provide very high accuracy in the FL estimation [16]. Recently, the interest on TW fault-location methods has increased due to improvements in smart electronic devices for data acquisition, relatively cheap time synchronization techniques and availability of effective data communication systems [17, 18, 19, 20, 21, 22, 23].

TW FL systems make use of transient signals in power lines. Those transient signals can actually be generated by different causes such as electrical faults, partial discharges, switching relays, lightning or external noise induced into the power system. The abrupt variation of the voltage in a certain point of the power line, where the fault insists, creates a high frequency pulse which travels in the two directions, upstream and downstream the fault point [24, 25]. The speed of the traveling wave depends on the line's features and may be very close to the speed of light for transmission lines and about the half (around $150\,m/\mu s$) for distribution lines. The fault point is derived by precisely time-tagging the TW pulse captured by the FL device(s) and performing the comparison between the time difference of two acquired pulses and the total propagation time of the line.

Traveling wave technique may also be integrated in protective relays. The greatest part of relays currently available on the market are mostly based on voltage and current phasors, that is they operate based on steady-state fault signals. This means that at least one line cycle is required by such devices in order to precisely measure the phasors. By adopting TW methods for protecting the power system, shorter time to achieve the power system protection can be expected [26].

1.3.1 Accuracy

The accuracy of the fault position estimation depends on many factors:

1. the precision and accuracy of the time-tagging of the pulses;
2. detection of the rising edge of the fault pulse;
3. analog-to-digital conversion.

System clocks in all the FL devices should be precisely synchronized in order to have an effective FL system. Different ways exist for synchronizing a certain number of devices such as a synchronization cable bus, fiber optic, radio, Global Position System (GPS).

Another source of inaccuracy is related to how the HF pulse arrives at the input of the sensor of the FL system. The TW moves along the line and will be subject to attenuation because of the losses (both resistive and radiated), distortion due to dispersion phenomena and low-pass filtering of the transmission line itself. The combined effects of these phenomena deteriorate the pulse shape of the TW, in particular the rising-edge of the pulse may be significantly affected by degradation, so that the FL system may be inaccurate about the interpretation of the time at which the pulse is detected. In order to reduce such effects, the maximum distance between two FL devices (for two- or multi-end methods) should be chosen accordingly.

Many TWs techniques uses analog to digital converter (ADC) in order to sample the phase current or voltage. It is worth noting that the sampling rate determines the accuracy of the FL. In fact, in order to properly locate the fault it is important to precisely discriminate the start of the fault condition. The higher the sampling rate, the lower the time interval between two consecutive current or voltage samples. This means that, at higher sampling rates, the arrival of the traveling wave generated by the fault condition can be found with a much higher precision. For instance, in order to have a theoretical precision of 1 meter in the FL estimation, on a transmission line where the propagation speed v_p is close to $c = 3 \cdot 10^8 m/s$, the sampling rate has to be at least:

$$f_s = \left(\frac{1\,m}{3 \cdot 10^8 m/s} \right)^{-1} = 300\,\text{Mhz}$$

ADCs with such high sampling rate are usually expensive and difficult to handle by cheap microcontrollers, so often Field Programmable Gate Array (FPGA) must be used to control the acquisition process and buffer the acquired samples. In fact, the use of high sampling rate ADCs produces a big amount of data which need to be quickly saved on the device memory and processed.

The acquired data contains both the fundamental frequency components and the transients associated with the fault, hence the data need to be high-pass filtered in order to eliminate the 50/60 Hz components, not useful for the FL.

1.3.2 Travelling-wave theory

In this section, the theory behind traveling waves in three-phase power lines is discussed [27, 17]. The equivalent circuit of a transmission line of infinitesimal length is shown in Fig. 1.5, where R, L and G respectively are resistance, inductance and

conductance per unit of length. By applying Kirchhoff's laws to this circuit we have:

$$v(x,t) - v(x+\Delta x,t) = R \cdot \Delta x \cdot i(x,t) + L \cdot \Delta x \frac{\partial i(x,t)}{\partial t} \tag{1.8}$$

$$i(x,t) - i(x+\Delta x,t) = G \cdot \Delta x \cdot v(x+\Delta x,t) + C \cdot \Delta x \frac{\partial v(x+\Delta x,t)}{\partial t} \tag{1.9}$$

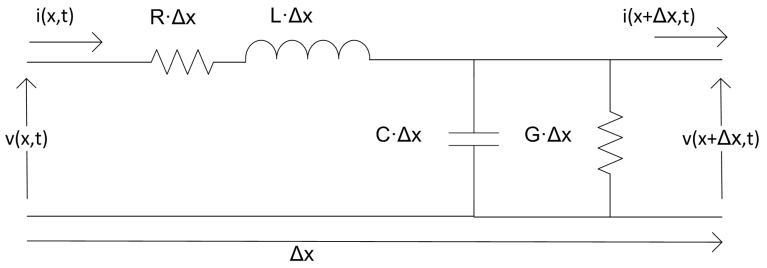

Figure 1.5: Equivalent circuit for a segment of transmission line made of two conductors.

By assuming infinitesimal Δx and by dividing (1.8) and (1.9) for this quantity, the derivatives of the two electrical quantities with respect to the position are obtained. The results are the following equations:

$$\frac{\partial v(x,t)}{\partial x} = -R \cdot i(x,t) - L \frac{\partial i(x,t)}{\partial t} \tag{1.10}$$

$$\frac{\partial i(x,t)}{\partial x} = -G \cdot v(x,t) - C \frac{\partial v(x,t)}{\partial t} \tag{1.11}$$

Equations (1.10) and (1.11) represent voltage and current in a two-conductor transmission line as a function of position x and time t. The presence of the minus sign in (1.10) and (1.11) is explained by the fact that as we proceed along the line (increasing x), the amplitudes of the two waves decrease.

Now we move to the Laplace domain by substitution [28]:

$$s = \frac{\partial}{\partial t}$$

$$\frac{\partial v(x,s)}{\partial x} = -Z \cdot i(x,s) \tag{1.12}$$

$$\frac{\partial i(x,s)}{\partial x} = -Y \cdot v(x,s) \tag{1.13}$$

where $Z = (R + sL)$ and $Y = (G + sC)$.

We take the derivative with respect to the position of (1.12) and (1.13):

$$\frac{\partial^2 v(x,s)}{\partial^2 x} = -Z \cdot \frac{\partial i(x,s)}{\partial x} \tag{1.14}$$

$$\frac{\partial^2 i(x,s)}{\partial^2 x} = -Y \cdot \frac{\partial v(x,s)}{\partial x} \tag{1.15}$$

By substituting (1.12) and (1.13) in (1.14) and (1.15), we obtain the voltage and current wave equations in which only one quantity, voltage or current, appears.

$$\frac{\partial^2 v(x,s)}{\partial^2 x} = \gamma^2 \cdot v(x,s) \tag{1.16}$$

$$\frac{\partial^2 i(x,s)}{\partial^2 x} = \gamma^2 \cdot i(x,s) \tag{1.17}$$

where $\gamma = \sqrt{Z \cdot Y}$ is the propagation constant.

Traveling waves are hence described in the Laplace domain by (1.16) and (1.17), whose solutions are given by:

$$v(x,t) = v_I e^{-\gamma x} + v_R e^{\gamma x} \tag{1.18}$$

$$i(x,t) = i_I e^{-\gamma x} + i_R e^{\gamma x} \tag{1.19}$$

The first components of (1.18) and (1.19) are referred to as incident voltage and current waves ($v_I e^{-\gamma x}$ and $i_I e^{-\gamma x}$), while the latter components are the reflected waves ($v_R e^{\gamma x}$ and $i_R e^{\gamma x}$).

For a given position of the transmission line, it is possible to calculate the line characteristic impedance as the ratio of the voltage and current for both incident and reflected waves:

$$Z_C = \frac{v_I}{i_I} = -\frac{v_R}{i_R} = \sqrt{\frac{Z}{Y}} \tag{1.20}$$

hence we can obtain an equation for $i(x,t)$ in terms of v_I, v_R and Z_C:

$$i(x,t) = \frac{1}{Z_C}(v_I e^{-\gamma x} - v_R e^{\gamma x}) \tag{1.21}$$

As we said, a traveling wave is composed of a voltage component and of a current

component, these two being linked by the characteristic impedance of the line as expressed by (1.20).

Let's assume to have a traveling wave which travels on a line with Z_C characteristic impedance (Fig. 1.6).

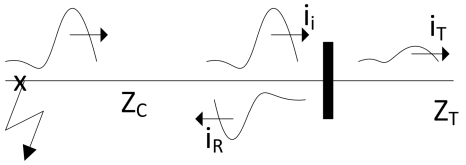

Figure 1.6: Example of incident (i_i), transmitted (i_T) and reflected (i_R) wave.

The incident voltage v_I and current i_I of the traveling wave will reach one of the terminals of the line, where a certain part will be transmitted as v_T and i_T, while another portion will be reflected as v_R and i_R. If Z_T is the line characteristic impedance after the terminal, the amount of energy transmitted and reflected depends from Z_C and Z_T. At the transition we have:

$$\frac{v}{i} = \frac{v_I + V_R}{i_I + i_R} = Z_T \tag{1.22}$$

By using (1.20) and (1.22) we obtain:

$$v_R = \frac{Z_T - Z_C}{Z_T + Z_C} v_I = \rho_v v_I \tag{1.23}$$

$$\rho_v = \frac{Z_T - Z_C}{Z_T + Z_C} \tag{1.24}$$

with ρ_v the voltage reflection coefficient.

At the same way, the current reflection coefficient may be expressed as:

$$\rho_I = \frac{Z_C - Z_T}{Z_C + Z_T} \tag{1.25}$$

We hence obtained useful relationships between incident and reflected waves. In particular, if:

1. $Z_C = Z_T$, there is no energy reflected back hence $v_I = v_T$ and $i_I = i_T$.
2. $Z_T = 0$, we have $v_I = -v_R$ and $i_I = i_R$.
3. $Z_T = \infty$, we have $i_I = -i_R$ and $v_I = v_R$.

In the latter two cases, all the energy is reflected back, none is transmitted.

1.3.3 Modal Analysis

The phase current and voltage signals may be decoupled as different independent propagation modes by using modal transformation. This involves a linear transformation which simplifies the analysis by making use of some specific relations involving the phase signals on the three-phase system. One of the most used transformations applied to current and voltage phasors are the symmetrical components, which are used in fault analysis and in general in power system analysis. While symmetrical components cannot be applied to instantaneous values, which is the case of traveling waves, Clarke transformation may be used [29]. The modes are usually referred to as zero 0, alpha α and beta β.

$$\begin{bmatrix} I_\alpha \\ I_\beta \\ I_0 \end{bmatrix} = T_{\alpha\beta 0} \begin{bmatrix} I_A \\ I_B \\ I_C \end{bmatrix} = \frac{1}{3} \begin{bmatrix} 2 & -1 & -1 \\ 0 & \sqrt{3} & -\sqrt{3} \\ 1 & 1 & 1 \end{bmatrix} \begin{bmatrix} I_A \\ I_B \\ I_C \end{bmatrix} \tag{1.26}$$

Equation (1.26) represents the Clarke components of the phase current for Phase A. It can be noted that if the whole current flows through conductor A and half returns through B and C, this will excite the alpha mode only, so $I_\alpha = \frac{1}{3}(2 \cdot I_A - I_B - I_C)$ (first row of the matrix). The current flowing trough B and returning from C excites the beta mode only, hence $I_\beta = \frac{1}{3}(\sqrt{3}I_B - \sqrt{3}I_C)$ (second row only of the matrix). If the same current flows trough conductors A, B and C and returns to earth, the only mode that will be excited is the zero mode, that is $I_0 = \frac{1}{3}(I_A + I_B + I_C)$ (third row of the matrix).

Three sets of Clarke components, for A, B and C conductors, must be used for covering all fault types. In fact, (1.26) only works fine for Phase A to ground fault or Phase B to Phase C faults [17]. The three transformation matrices for phases A, B and C are:

$$T^A_{\alpha\beta 0} = \frac{1}{3} \begin{bmatrix} 2 & -1 & -1 \\ 0 & \sqrt{3} & -\sqrt{3} \\ 1 & 1 & 1 \end{bmatrix} \tag{1.27}$$

$$T^B_{\alpha\beta 0} = \frac{1}{3} \begin{bmatrix} -1 & 2 & -1 \\ \sqrt{3} & 0 & -\sqrt{3} \\ 1 & 1 & 1 \end{bmatrix} \tag{1.28}$$

$$T^C_{\alpha\beta 0} = \frac{1}{3} \begin{bmatrix} -1 & -1 & 2 \\ -\sqrt{3} & \sqrt{3} & 0 \\ 1 & 1 & 1 \end{bmatrix} \tag{1.29}$$

Single line-to-ground (SLG) faults are the natural application of alpha components, while, for line-to-line (LL) faults, beta components are more appropriate.

The characteristic impedances, as well as attenuation and dispersion, are not the same for modes $\alpha\beta 0$. The selection of the more appropriate mode for traveling wave FL depends mainly on propagation speed, dispersion and attenuation. For instance, the 0 mode is not well suited for traveling wave FL due to more important attenuation and dispersion than α and β modes. This is related to the higher losses of the earth, compared to the losses on the conductors.

In [17] it is reported that alpha components are in many cases the best selection for working with traveling waves associated with faults, when data from the electrical system is sampled and acquired. Beta components provide slightly higher amplitudes for some particular cases of LL faults.

1.3.3.1 Attenuation and dispersion

In general, the wave propagation constant of each mode m can be expressed in a real part (α), which represents the attenuation constant, and an imaginary part (β), which represents the phase constant[1].

$$\gamma_m = \alpha_m + j\beta_m \tag{1.30}$$

This means that each mode can have its own attenuation and propagation speed, that may be different for other modes. A non-zero value of α_m means that the line has losses due to resistance and conductance of the line, R and G. In other words, the traveling wave will attenuate its amplitude as it travels along the line.

A non-zero value of β_m means that we have dispersion or distortion, i.e. the propagation speed v_m of mode m depends on the frequency ω:

$$v_m = \frac{\omega}{\beta_m} \tag{1.31}$$

In case of lines without any losses ($\alpha_m = 0$), the propagation speed depends on L and C of the line.

An ideal step signal applied as input of the line (or a very sharp and fast fault signal) is composed ideally by an infinite number of frequency components, which will travel at different propagation speed as per (1.31). The original waveform will

[1]Please note that α and β in this context do no refer to alpha and beta modes previously introduced, but the way adopted in the literature to express the real and imaginary part of the wave propagation constant.

be distorted while the TW moves along the line. By virtually looking at the signal at increasing position x of the line, the wave will look more and more "slow", with smoother rising-edge and consequently reduced frequency contents.

1.3.4 Classification of traveling-wave methods

Traditionally the TW method have been classified in five types: A, B, C, D, E [1].

1.3.4.1 Type A

In this type the FL system calculates the time difference of the first captured TW and its reflection (single-end method). The estimated fault distance is given by:

$$d = v_p \cdot \frac{\Delta t}{2}$$

where:

Δt is the difference between the arrival of the first TW and the reflection;

v_p is the propagation speed of the TW in the line.

The beauty of this method is that a remote unit is not necessary. Hence, there is not critical time synchronization between two devices at the two ends of the line and neither a data communication link between them. On the other side, from the lattice diagram it is clear how reflection can be hard to be distinguished (i.e. the reflection from the other terminal may arrive first). When the fault is exactly in the middle of the line, the traveling wave will reach the two ends at the same time and, in this case, the time difference between the arrival times is ideally zero.

In Fig. 1.7, the fault, section F, is imagined not in the middle of the line, i.e. $m < l - m$. For this reason, the traveling wave will reach the L end first and then the R one. In L, part of the energy will be transmitted to the left side of section L, part will be reflected back and part will be absorbed. Same considerations can be made for R.

The problems arises when the device is misled by the other reflected pulses arriving one after the other. For instance, if at certain distance on the left of section L there is another line (B end), which is closer to L so that $\overline{BL} < \overline{LF}$, the TW reflected from B will reach L before the reflected wave from the fault section reaches L t_{L2}. This incorrect result could be avoided if the direction of the TW pulse can be detected by the instrument, e.g, by using two sensors per side, it could be possible to discriminate which sensor is "hit" first, thus understanding the propagation direction.

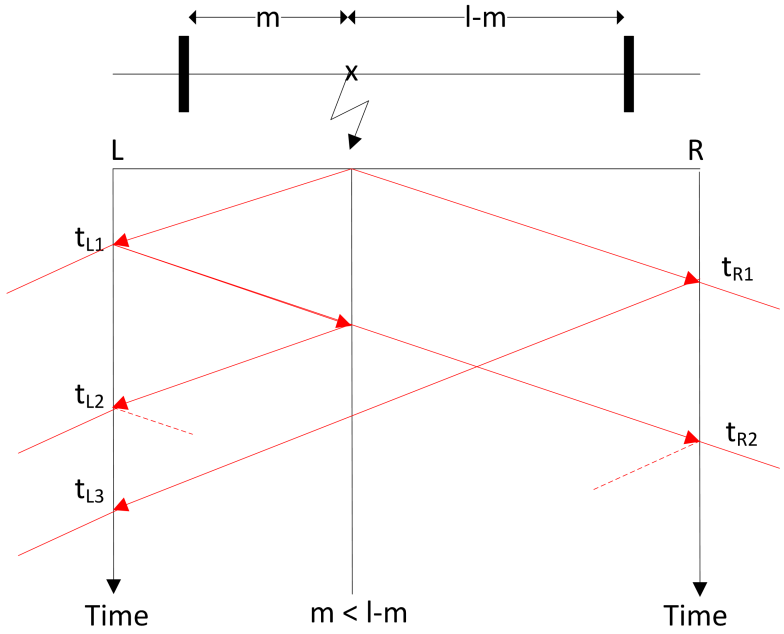

Figure 1.7: Lattice diagram showing incident, transmitted and reflected travelling-waves.

1.3.4.2 Type B

This type of TW fault locator is dual-ended, thus it measures the time difference between the arrival of the first TW at one end and the arrival of the other TW at the other end of the line, in this case the FL devices are installed at the two ends [30]. The two units are supposed to have a communication link between them since the arrival of the first pulse at one end starts a counter that is then stopped by the other device when it receives the second pulse. The fault position is hence given by:

$$d = \frac{L}{2} + \frac{v_p \cdot \Delta t}{2}$$

where:

L is the distance between the two FL units;

Δt is the time difference between the arrival of the TW at the first and the second end;

v_p is the propagation speed of the TW along the line.

1.3.4.3 Type C

Type C differentiate from the previous two methods being an active method. In particular, type C is a single-end method where an impulse is generated and injected

into the line after a fault is detected. This is probably one of the most common TW method for fault-location and it is also known as Time Domain Reflectometry (TDR). The fault distance is given by:

$$d = v_p \cdot \frac{\Delta t}{2}$$

where Δt is the time difference between the injecting time of the impulse and the detection of the reflected TW from the fault point.

1.3.4.4 Type D

In type D, different TW fault-locator devices have very accurate time synchronization and time-tagging capabilities [1]. They also are provided with a data link to a central site where all the time-tagged pulses are collected. The fault point distance can be calculated in different ways depending on the approach used.

One possibility is to calculate the time difference between the time-tags of two FL devices installed on the same section of the line. The device installed in L knows the arrival time t_L of the traveling wave generated in the the fault point F, neglecting any further reflections. The same applies to R, where the arrival time of the TW is t_R. The two devices will communicate t_L and t_R respectively and the algorithm at the central remote side calculates the estimate of the FL. The formula for calculating d in this simple case could be similar to the one of Type B.

1.3.4.5 Type E

Type E uses the transients generated after the line is re-energized, in consequence of a fault, from one terminal only [2]. By supplying voltage to the system, the faulty component will cause again the trip of the line, so that a new fault pulse will be generated from the defect, which will travel along the line. The advantage of this method is that multiple reenergizations may be performed, thus more data can be collected and average algorithms calculated, thing that will increase the accuracy of the estimated fault distance. A similar approach is often used for FL in underground cables, especially in power distribution, for the search of the fault point.

Chapter 2

Partial Discharges theory

2.1 Introduction

Partial discharges are localized electrical discharges that only partially bridge the insulation between conductors and which can or cannot occur adjacent to a conductor [31]. PD induces pulses featured by a fast rising time and appearing as short bursts in the cable main conductor and shield. The use of specialized sensors and instruments allows to acquire and process these pulses. PD measurement can be considered one of the most valuable non-destructive means for assessing the quality and the integrity of HV and MV power apparatus and cables. The diagnosis allows to assess the overall state of the system, thus providing an indication about the probability of developing weak points. The time between PD ignition and final breakdown depends on the discharge type and the point where PDs take place. A PD event is a complex phenomenon which has a stochastic nature and its features can give information about defect type.

Many faults can be prevented by exploiting partial discharge diagnostic. Most of these failures can be caused by manufacturing imperfections, such as voids and contaminants in the insulation, or poor workmanship during installations, such as cuts or and missing components. Clearly, not all the possible failures can be prevented by PD analysis, such as the case of cable cuts by ground excavators during civil works.

Partial discharges can occur mainly:

- In cavities
- On the insulation surface
- In gases surrounding metallic protrusions

(a) (b)

Figure 2.1: Effects of partial discharge activity prior to fault.

Gaseous regions have generally a lower dielectric permittivity than solid insulation. A local electric field increase favors PD inception and leads to a degradation process. PDs can be accompanied by emission of UV light, sound, heat and electromagnetic fields.

The components generally affected by PD are:

- Switchgear buses
- Cable joints
- Bus duct Cables
- Cable terminations
- Transformers
- Insulators
- Rotating machines

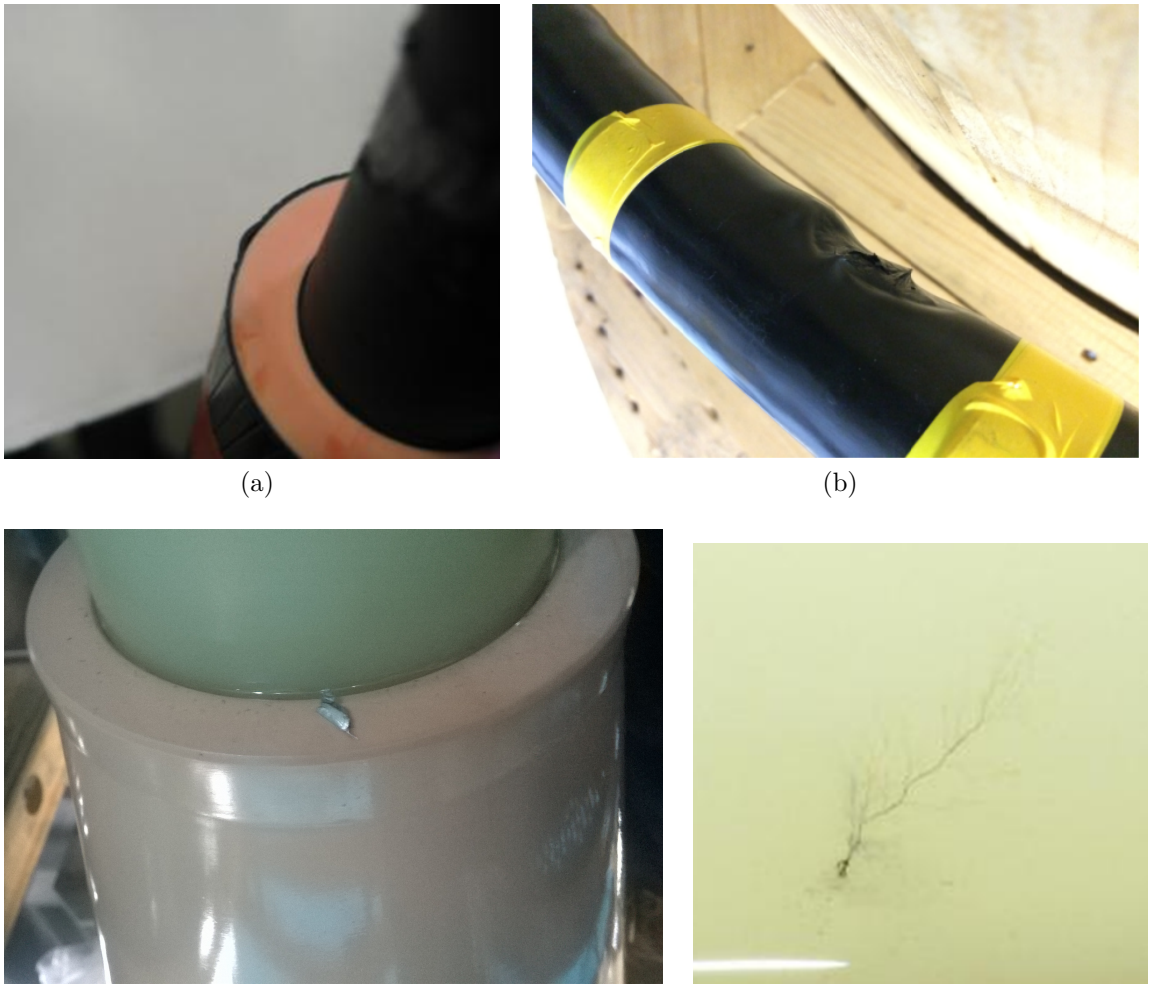

(a) (b)

(c) (d)

Figure 2.2: Irregularities on cable semi-conductive layer.

It should be said that defects in the insulation can be detected also from other indicators. For instance, dissolved gas analysis (DGA) is a consolidated method for understanding the actual working status of transformers [32].

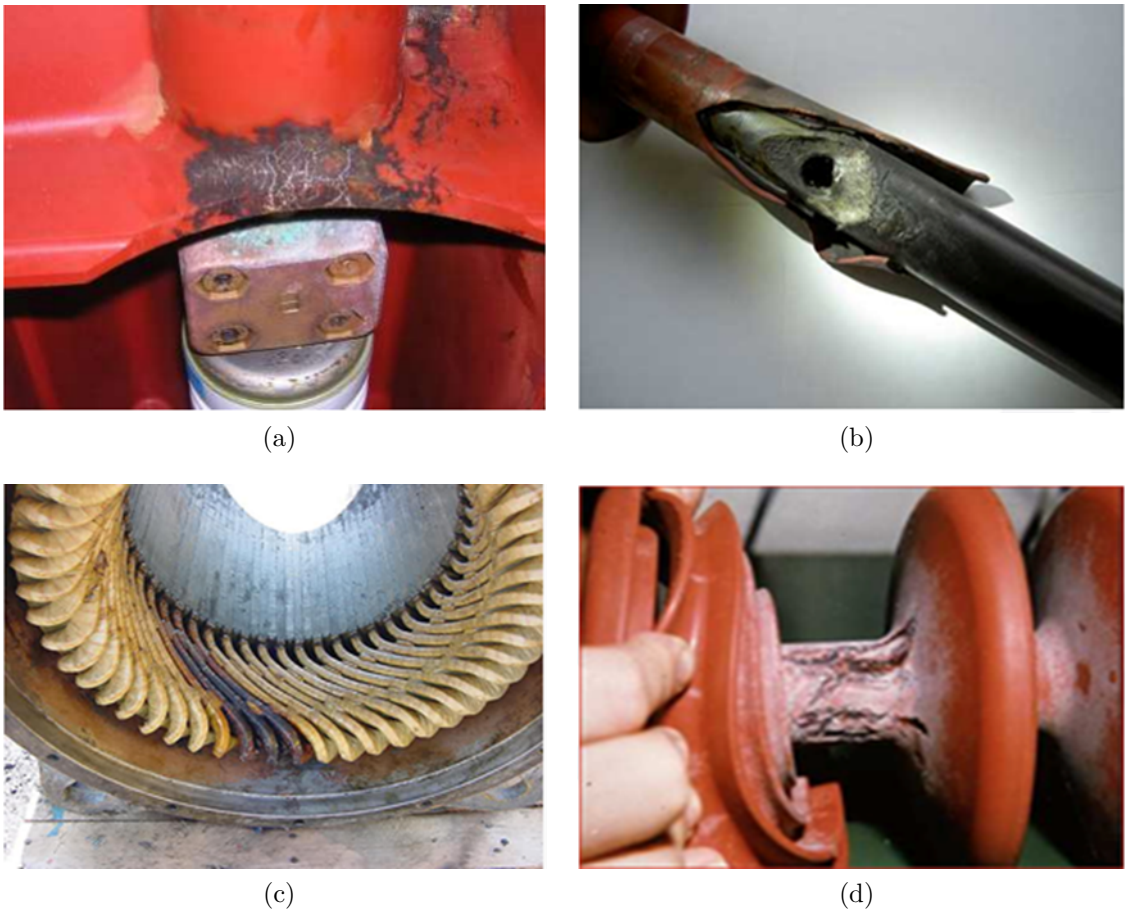

(a) (b)

(c) (d)

Figure 2.3: Failures.

2.2 Partial Discharge Physics

In order to clarify how partial discharges take place on real electrical components, a short analysis of physical mechanisms can be useful [33]. In this section, the inception process of a discharge in embedded gas cavities and the inception conditions under AC voltage will be explained [34]. Townsend and Streamer theories, described shortly below, suggest to distinguish between three different kind of discharge.

2.2.1 Townsend discharge

The inception of a Townsend discharge is based on the "Townsend avalanche" concept [35], referred to a gas embedded cavity inside a dielectric layer between two electrodes (anode and cathode), under well-defined pressure condition, shape and dimension. If a starting electron is accelerated toward the anode by the electric field inside the cavity, a collision between the electron and a gas molecule can occurs and a

new electron/positive ion couple is created [36]. The number of collisions generated by the first one is elevated and this process leads to a self-sustaining discharge.

Discharge features are listed below:

- High rise time and decay time
- Low frequency content
- Low amplitude.

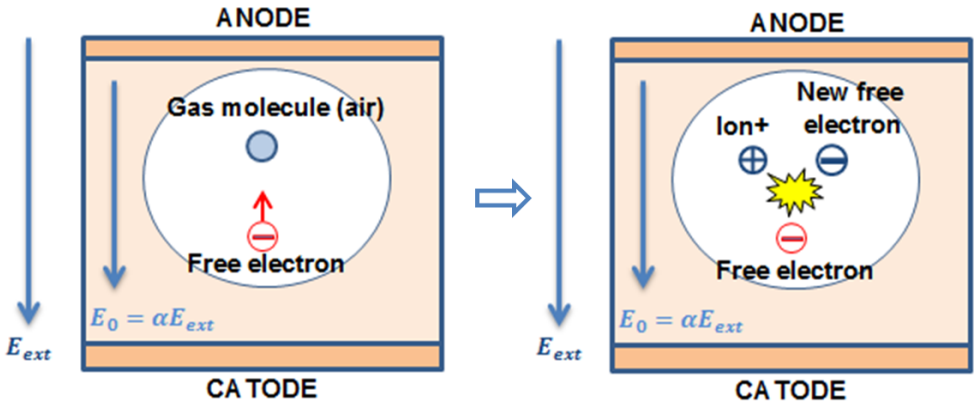

(a)

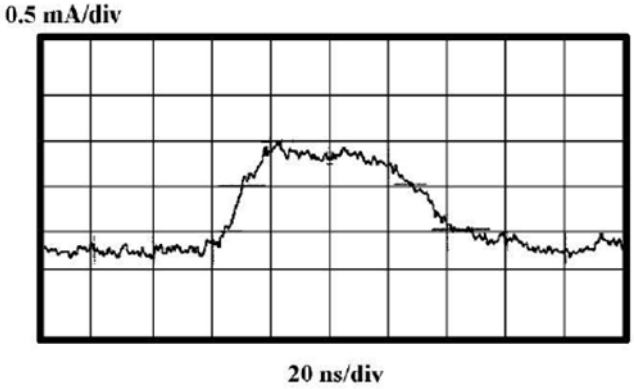

(b)

Figure 2.4: Townsend discharge: (a) principle and typical pulse shape (b).

2.2.2 Streamer discharge

The Townsend theory preserves its validity only under certain pressure conditions and cavity dimension [35]. For values of the product $p \cdot d$ lower than $300kPa \cdot mm$, the streamer theory can better explain the phenomenon. The electrons accelerated toward the anode (primary avalanche) leave behind a positive space charge region

and secondary electronic avalanches can head towards this region under the attraction force. If this process continues, the ionizing channel reaches the cathode and leads to the short circuit of the cavity [37].

Discharge features:

- Low rise time and decay time (fast discharge)
- High frequency content
- High amplitude

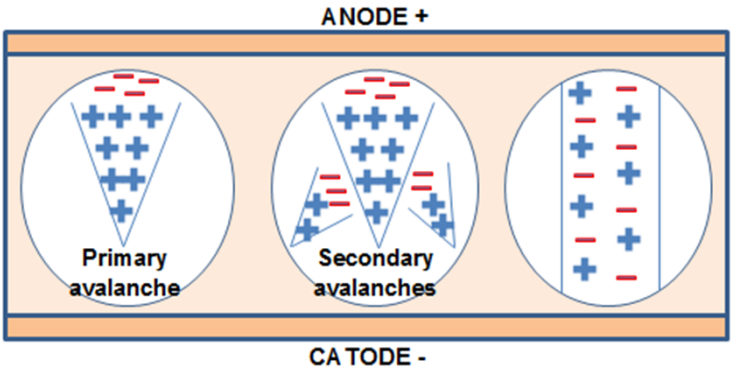

(a)

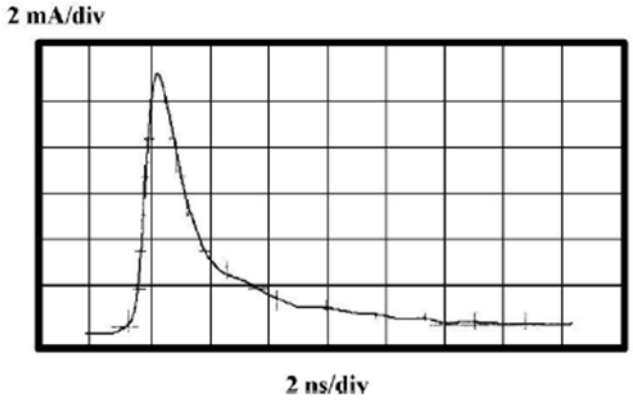

(b)

Figure 2.5: Streamer discharge: (a) principle and typical pulse shape (b).

2.2.3 Pitting discharge

Pitting discharges take place in correspondence to crystals on the cavity surface, caused by the accumulation of charged particles during the Townsend process. The waveform looks like a sequence of two Townsend discharges.

Discharge features:

- Low rise time and high decay time
- Low frequency content
- Low amplitude

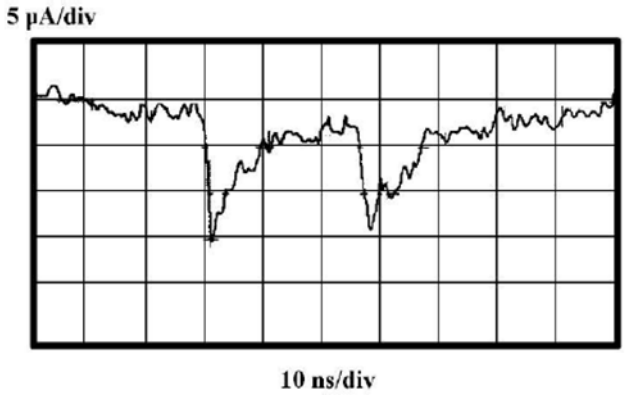

Figure 2.6: Pitting discharge: typical pulse shape.

2.2.4 Conditions for discharge inception in cavities

A discharge can take place only if two starting conditions are satisfied.

1. Deterministic conditions: the field inside the cavity exceed the inception field. The breakdown field value (Inception Field) depends on pressure condition and cavity geometry. It can be obtained by means of the Paschen law, which gives the voltage for starting a breakdown arc between two electrodes in a gas in dependence of pressure and gap distance. In fact, inception field is a function of the product $p \cdot d$, where p is pressure and d is the distance between two plane electrodes at different potential. Each curve has a minimum: for air this value is about 327 V at $0.756 Pa \cdot m$. A streamer discharge can be self-sustaining only if the working point on the curve is in the right side with respect to the minimum. Paschen curves [35] are shown in Fig. (2.7) for different type of gas.

2. Stochastic conditions: free electron available for starting the electronic avalanche. The availability of a starting free electron has a stochastic nature and depends on:

   - Presence of background ionizing radiations.
   - Schottky emission of electrons from metal electrodes and/or dielectric surface.

The applied electric field must allow free electron to acquire enough kinetic energy for the collisions with gas molecules. The ionizing process can start only in this condition.

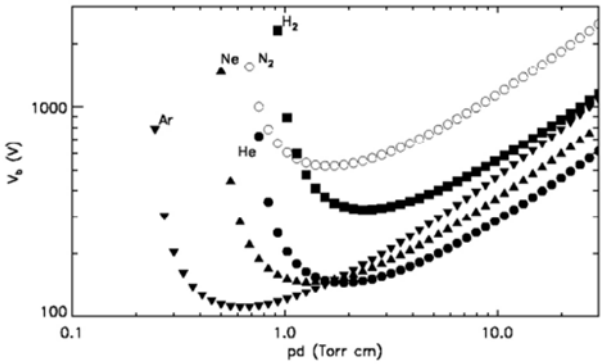

Figure 2.7: Paschen curves for different gases.

2.2.5 Inception mechanism under AC voltages

The inception mechanism of PDs inside a cavity under sinusoidal voltages can be clarified by observing Fig. 2.8.

where symbols meaning is:

- E_0: portion of the external field applied to the cavity;
- E_q: local field due to charges separation;
- E_i: resulting internal field ($E_i = E_0 - E_q$).

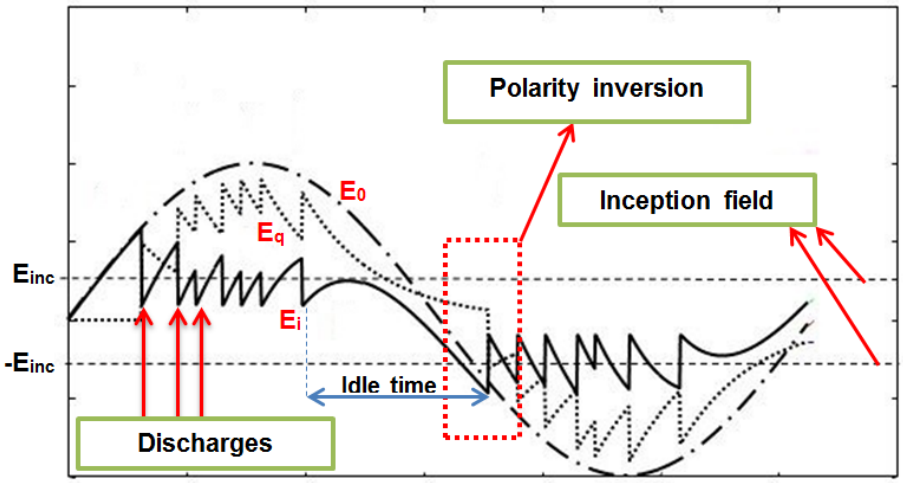

(a)

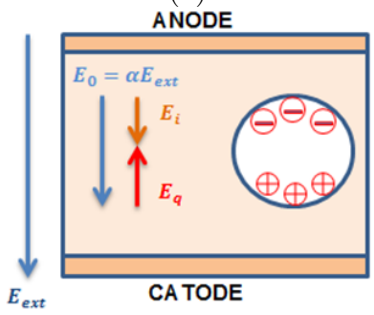

(b)

Figure 2.8: Inception mechanism under sinusoidal voltage.

The presence of E_0 causes the separation between opposite charges inside the cavity. The resulting internal field E_i is equal to the difference between the field applied to the cavity E_0 and the local field due to charges separation E_q. Referring to the first half-period, in correspondence of each discharge, E_q increases very quickly, E_i decreases under extinction field and the discharge extinguishes. After a discharge the local field decreases because of the recombination phenomenon of positive and negative accumulated charges, or due to drifting on the cavity surface. If E_i increases over inception field and a free electron is available, another partial discharges can occur.

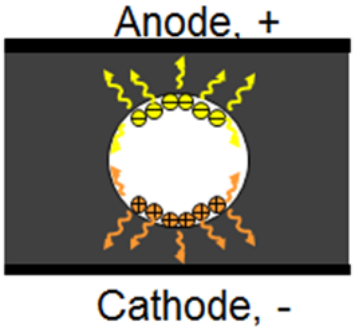

Figure 2.9: Charges recombination and drifting.

It is possible to note that PDs occur randomly after E_i exceeds the inception field value (positive or negative). The stochastic nature of a free electron availability results in a time delay between the crossing of the inception field value and the discharge inception, so PDs occur with different amplitudes. Due to this stochastic delay it is impossible to measure the true PD inception voltage (PDIV). For this reason the conventional definition of PDIV is defined according to standard IEC 60270 [31]:

"Applied voltage at which repetitive PD are first observed in the test object when the voltage applied to the object is gradually increased from a lower value at which no PD are observed".

Similarly, the PD extinction voltage (PDEV) definition is :

"Applied voltage at which repetitive PD cease to occur in the test object when the voltage applied to the object is gradually decreased from a higher value at which PD are observed".

During the first discharge on each semi-period, E_0 becomes negative (or positive) and E_i and E_q have the same polarity. In this condition, available starting electrons are in smaller number because of the recombination process during the idle time. Moreover, E_i polarity does not facilitate the charge separation. This phenomenon is called "polarity inversion". It results in a larger stochastic delay time and in a partial discharge with a larger amplitude. The effect is the well-known pattern shape called "rabbit ears" shown in Fig. 2.10. The concept of "phase resolved PD pattern" will be clarified in the next section.

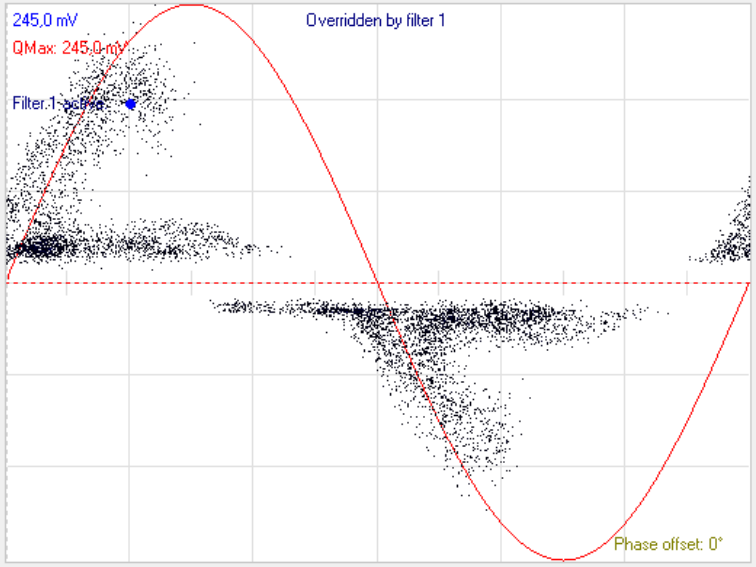

Figure 2.10: Typical internal partial discharge pattern with rabbit ears shape.

2.3 Phase Resolved Partial Discharge Pattern

The most common and effective way for evaluating the presence of dangerous partial discharge activities on power systems is through the analysis of the Phase Resolved PD pattern (PRPD). In this representation, the amplitude of the pulses acquired by the sensing device is graphed in the vertical axis of the plot; in the horizontal axis the phase angle at which the PD pulse occurs is represented. Each dot in a PRPD pattern (shortly referred as PD pattern) thus represents a PD pulse and its occurrence phase angle [38]. It is clear that the PD pattern can be generated only if the measurement system is correctly synchronized with the voltage frequency.

Usually synchronization is provided via specialized sensors (e.g, rogowski coil or current clamp). In some cases, the sensor used for acquiring the PD pulses also offers the synchronization signal. There are cases where it is not easy or possible to get a reliable synchronization. For such cases, an innovative method is presented in Appendix A.

Different kinds of defects usually show different specific PD patterns. The correct understanding of these patterns can indeed help TSO and DSO's engineers understanding the health status of the electrical system. The analysis of PD measurements further relies on parameters such as partial discharge amplitude, inception voltage and phase angle of the discharge [39].

The colors of the dots depend on the number of PD occurrences at the same magnitude and phase. The analysis of a PD pattern can give information about the

observed phenomenon and about the defect type on the component under test [40]. In this way it is possible to associate with each pulse the following information:

- Occurrence phase: defined as the phase value, with respect to applied voltage, where a discharge incepts.
- Pulse amplitude: defined as the peak value of a partial discharge pulse waveform.

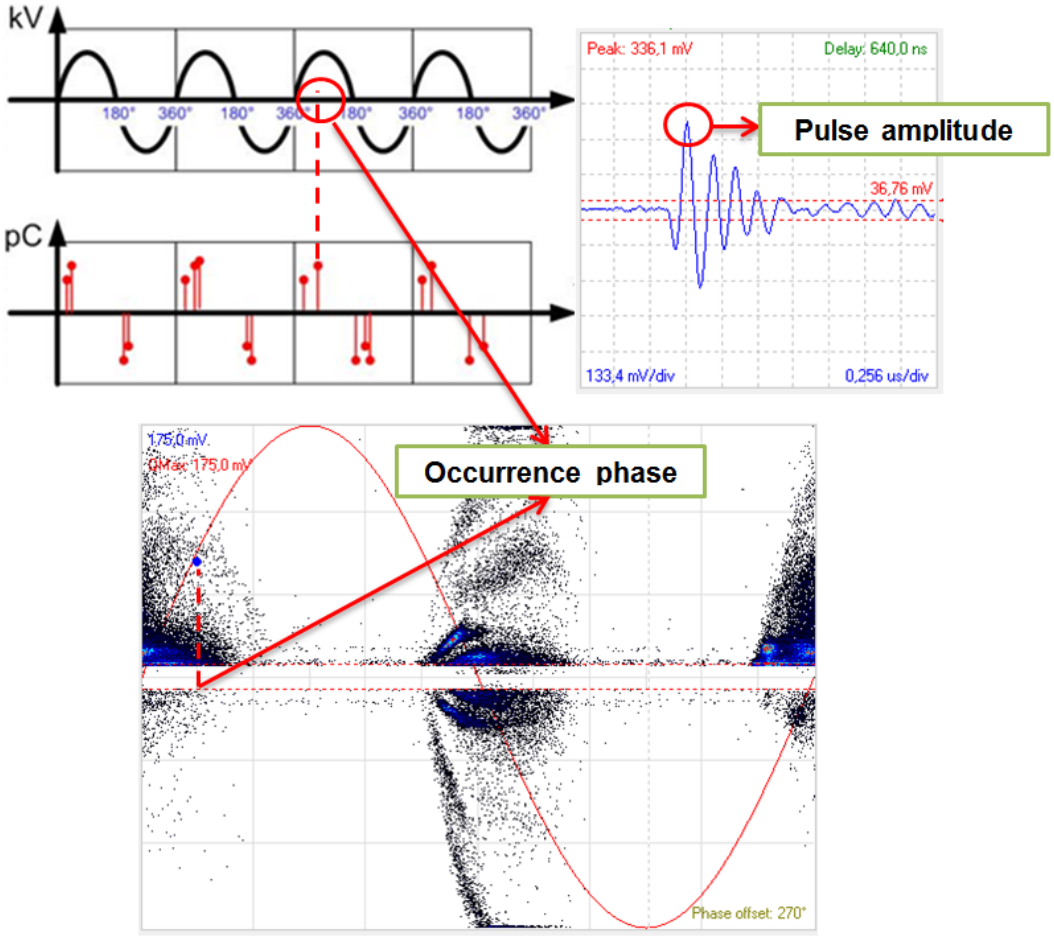

Figure 2.11: Build-up of a phase resolved PD pattern.

2.4 PDs analysis and classification

Partial discharges can be classified in four different categories:

- Internal discharges
- Surface discharges

- Corona discharges
- Floating mass discharges

In order to investigate an insulation degradation process and eventually recognize the presence of a defect on an electric component, it is very important to distinguish between different discharge phenomena [41]. This investigation can be carried out through the analysis of:

- PD pattern, as discussed in section 2.3;
- waveform of each PD pulse: critical pulses are often associated with higher rise-time;
- frequency content (FFT) of the PD pulses;
- amplitude of the pulses;
- type of component under test (e.g. joint, termination, cable, transformer, etc);
- load configuration (e.g. loaded circuit or no load with just capacitive current);
- environmental condition: humidity, rain, etc...;

PD signals waveforms and patterns shape can be different for the same phenomenon type, depending on the kind of defect, and may could change during time due to aging processes induced by the discharges, i.e., physical/chemical/geometrical modifications of the discharge site [42, 43].

2.4.1 Internal PDs

Internal discharges take place in defects consisting in gas cavities surrounded by a solid dielectric. The presence of a steady phenomenon can cause the formation of an electrical tree that starts from the cavity and leads to the breakdown of insulation. This kind of discharges can be considered the most critical PD activity in an electrical component. One important behavior of internal PDs is that the PD pattern will usually incept before zero-crossing. This leading phase angle always increases when the voltage feeding the circuit increases (i.e. the PD pattern shifts to the left). In fact, when it is possible to change the voltage supplying a circuit under test where suspicious PDs are detected, if the PD pattern shifts to the left then it is certain the presence of internal PDs. The simplified typical PD pattern is shown in Fig. 2.13. In Fig. 2.12 a real case of internal PD is shown. It should be

noted the phase shift in Fig. 2.12b compared to Fig. 2.12a because of the higher voltage. The representative PD pulse and its FFT is shown in Fig. 2.12c and d.

Features of internal PDs:

- Fast pulses: low decay time.
- Frequency spectrum up to 80 MHz.
- PDs mainly occur in a phase range around the zero-crossings of the applied voltage and markedly incept before zero-crossing as the voltage increases.

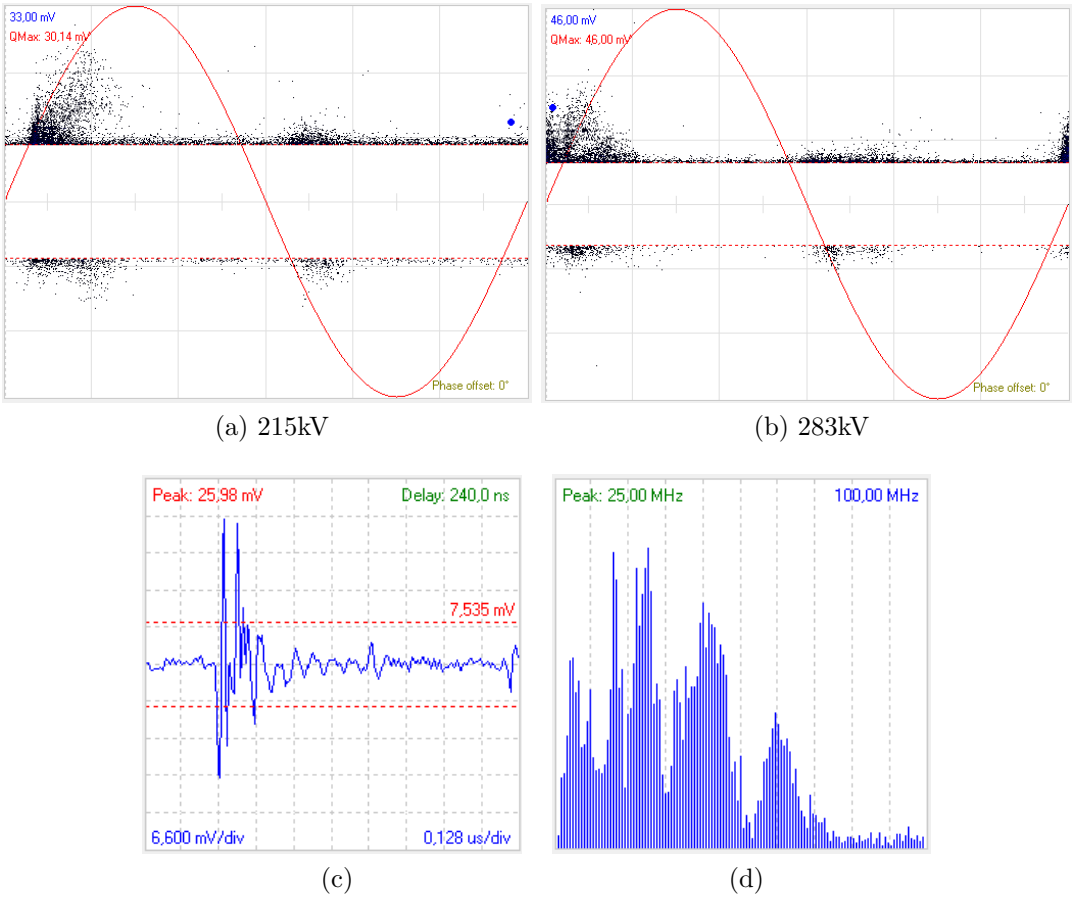

(a) 215kV (b) 283kV

(c) (d)

Figure 2.12: Example of Internal PDs in a joint: (a) PD pattern at 215kV and 284kV (b), (c) representative pulse shape in the time-domain and FFT (d).

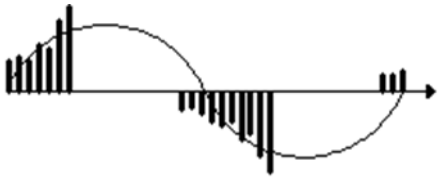

Figure 2.13: Simplified pattern of internal PDs.

2.4.2 Surface PDs

Surface PDs may be distinguished between critical and no critical surface PDs. The latter ones take place on the external dielectric surface of an electrical component and show a low frequency spectrum content, with a high decay time (slow surface discharges). The inception of this phenomenon can be favored by the presence of humidity in air or by the accumulation of dust or dirt, especially on outdoor components. Deposited particles on the surface can create a conductive path and lead to a flash-over. This event can be avoided by performing an accurate cleaning and maintenance of the component. In the other cases surface PDs are usually not usually critical. Fig. 2.14 shows a real example of low frequency surface PDs.

Features of low frequency surface PDs:

- Slow pulses: high decay time;
- Frequency spectrum lower than 20-30 MHz;
- PDs mainly occur in correspondence of zero-crossings of the applied voltage.

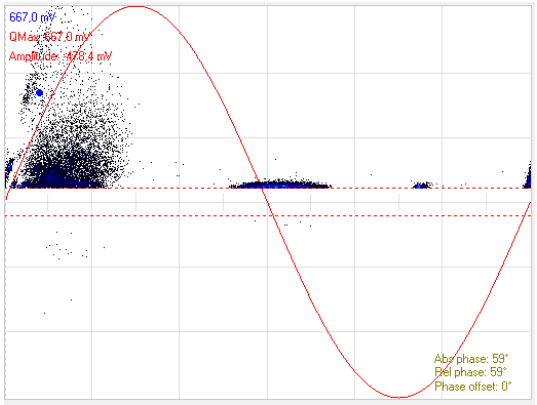

(a)

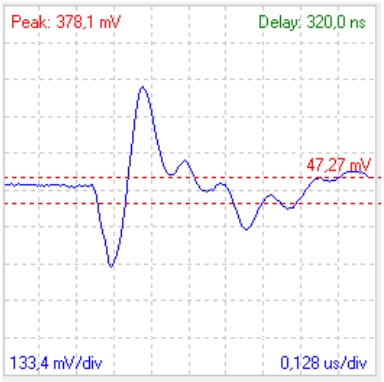

(b)

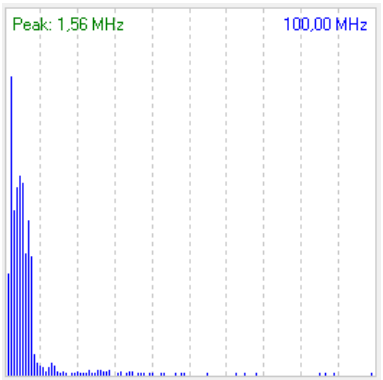

(c)

Figure 2.14: Example of slow surface PDs in a 220kV outdoor termination: (a) PD pattern, (b) representative pulse shape in the time-domain and FFT (c).

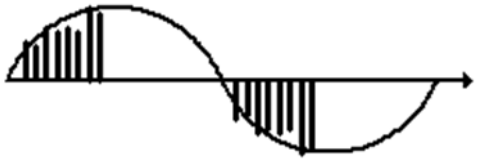

Figure 2.15: Simplified pattern of internal PDs.

Critical surface PDs can occur in correspondence of the separation surface between a conductor material and the adjacent dielectric or semi-conductive layer, generally in correspondence of mechanical defects. These discharges are often similar to an internal discharges, with a high frequency spectrum (fast surface discharges). Fig. 2.15 shows the simplified PD pattern which is valid for both slow and fast surface PDs. Fig. 2.15 shows a real example of high frequency surface PDs.

Features of high frequency surface PDs:

- Relatively fast pulses: low decay time;
- Frequency spectrum up to 40-50 MHz;
- PDs mainly occur in correspondence of zero-crossings of the applied voltage.

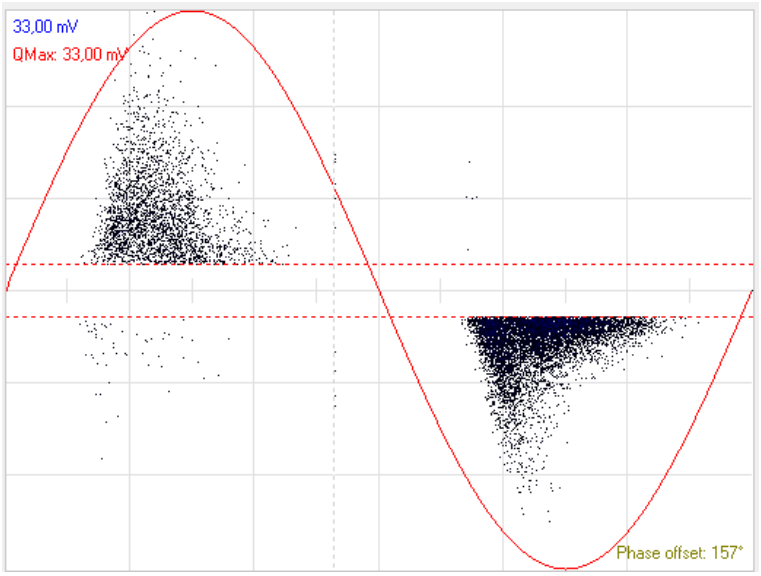

(a)

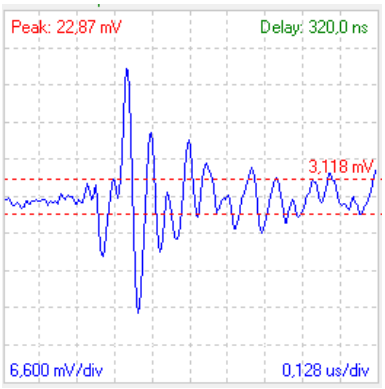

(b)

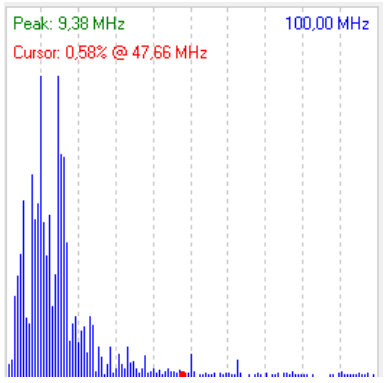

(c)

Figure 2.16: Example of fast surface PDs in a 220kV outdoor termination: (a) PD pattern, (b) representative pulse shape in the time-domain and FFT (c).

2.4.3 Corona PDs

Corona discharges take place in correspondence of exposed metallic protrusions, where the electric field is locally deformed and stronger. This condition causes the ionization of air molecules near the protrusion and the inception of partial discharges. The entity of the phenomenon depends on voltage level and environmental conditions. Corona discharges are not a dangerous phenomenon but their presence can hide other critical phenomenon and disturb the measurements activities. Therefore the presence of corona PDs must be limited as much as possible.

Features of corona PDs:

- Features: Middle-fast discharges

- Frequency spectrum usually lower than 40 MHz
- PDs occur in correspondence of the maximum value of the applied voltage. In particular:
  - Negative peak if the protrusion is under voltage (Fig. 2.17a)
  - Positive peak if the protrusion is connected to ground (Fig. 2.17b).
- Discharges generally cluster in an amplitude range over the trigger level.

Fig. 2.18 shows a real case of corona discharges, where both kinds of corona are present.

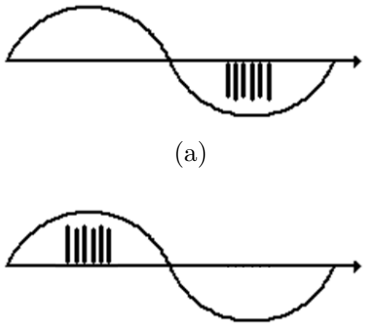

(a)

(b)

Figure 2.17: Simplified pattern of corona PDs.

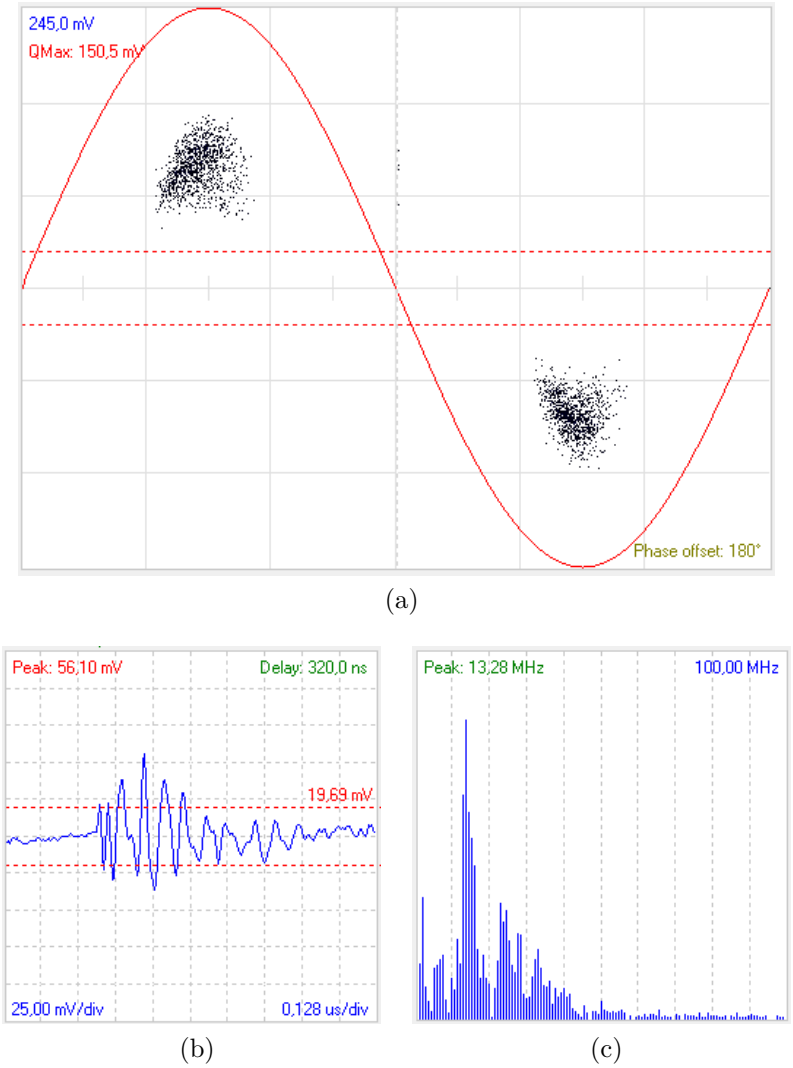

Figure 2.18: Example of corona on a 220kV outdoor termination: (a) PD pattern, (b) representative pulse shape in the time-domain and FFT (c).

2.5 Floating mass discharges

This kind of discharges take place in correspondence of metallic protrusions or objects not connected to a voltage source and isolated from ground; the electrical potential of a floating mass depends on the electric field distribution in space. Under the action of this field a charge distribution may appear on the object surface; inception is favored when voltage gradient dv/dt is maximum and discharges occurs in correspondence of zero crossings, when applied voltage changes its polarity. This phenomenon is not critical but it can disturb measurement activities. The simplified pattern is shown in Fig. 2.19, where the polarity of the pulses can be in the reality also all positive or negative.

Features of floating mass PDs:

- Features: Middle-fast discharges
- Frequency spectrum usually lower than 40 MHz
- PDs are clustered, similarly to corona discharges, in a brick-like pattern, but occur in a phase range around the zero crossings.

Figure 2.19: Simplified pattern of floating mass PDs: the polarity can be different.

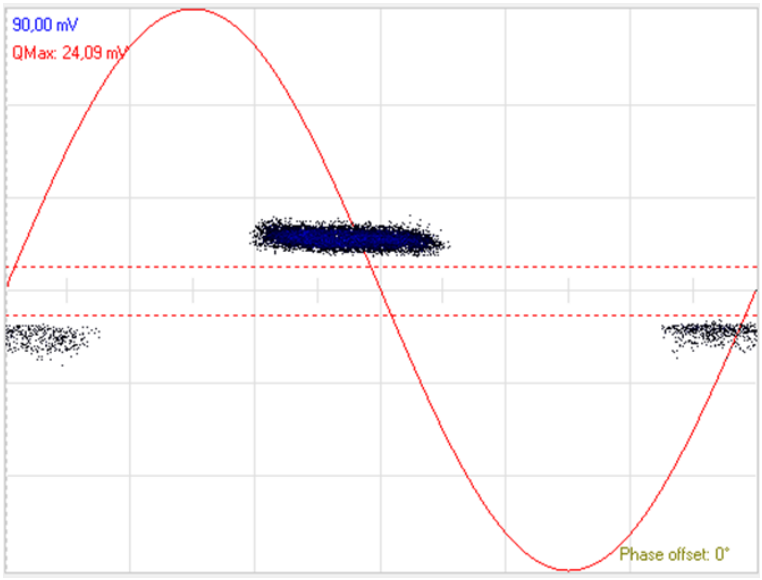

(a)

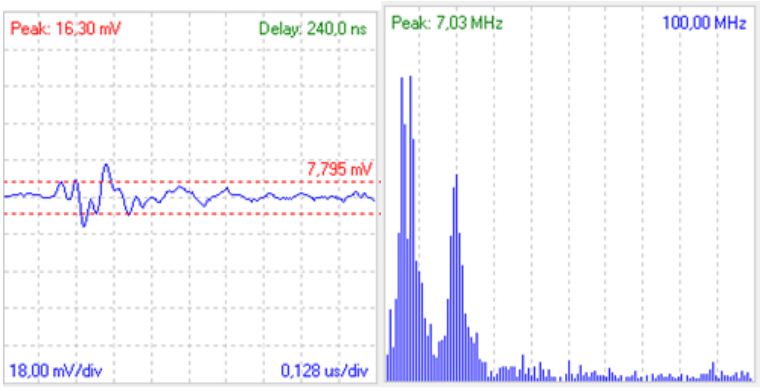

(b) (c)

Figure 2.20: Example of floating mass on a 20kV switchgear: (a) PD pattern, (b) representative pulse shape in the time-domain and FFT (c).

2.6 PD measurement

The measurement setup required for PD detection activities includes:

- HV test source;
- Sensor for PDs detection;
- A PD acquisition system or oscilloscope for pulses visualization.

Measurement activities can be performed:

- In on-line conditions: the component under test is energized at normal operating conditions. In this case the HV voltage source is the main electrical grid and the test voltage is the component rated voltage.
- In off-line conditions: the component under test is energized by means of a specific HV voltage source (HV test transformers) or with resonant generators for measurements with frequencies different from 50/60 Hz. Very low frequency (VLF) voltage generators are in some cases used for offline PD test.

The most common PD sensors are described in the following paragraphs.

2.6.1 High Frequency Current Transformers (HFCT)

Partial discharge activities in the insulation induce very small high frequency current pulses that propagate along the connections of the system under test. These currents can be detected by using high frequency current transformers, designed with a bandwidth generally ranging from hundreds of kHz to 50 MHz. A HFCT is composed of a ring-like magnetic circuit and a winding [44] (Fig. 2.21). The sensor must be clumped around an earth cable and not around a power cables, where the currents produce a magnetic field that saturates the ferromagnetic core. The high frequency currents, induced by discharges, generate a high frequency magnetic field in space that is concatenated to the magnetic circuit. Therefore, the instrument output signal is an induced electromotive force related to the PD pulses current.

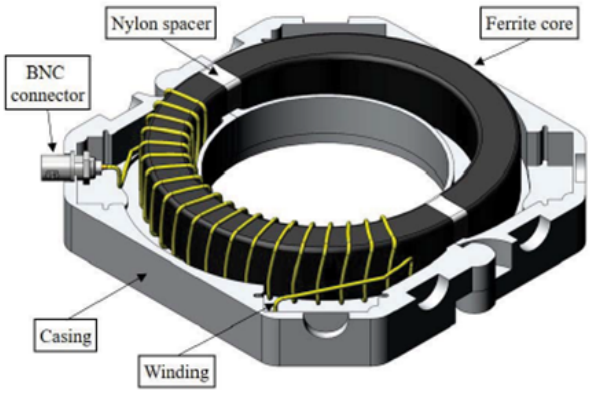

Figure 2.21: Internal structure of a HFCT.

2.6.2 Capacitive coupler

A capacitive coupler is a capacitor that works as a high-pass filter and provides to create a low-impedance path for partial discharges pulses. This capacitor must be connected in parallel with the object under test (Fig. 2.22), so this kind of PD detection cannot be adopted for on line measurements on real systems and is more suitable for experimental measurements carried out in the laboratory. Capacitive couplers are designed to stop 50/60 Hz frequencies and generally allow only high frequencies up to 0.5 MHz. These capacitors are often connected in series with a measurement impedance, generally a 50 Ω resistor. The voltage drop on this impedance represent the signal for the phase resolved pattern build up.

Figure 2.22: Laboratory capacitive divider.

2.6.3 Capacitive sensor

A capacitive sensor is a metallic electrode that allows to obtain a capacitive coupling effect by placing the sensor closer to the external surface of a cable. The coupling takes place between the electrode and the metallic shield of the cable. In this case the output signal of the sensor is related to PDs electrical charge.

2.6.4 Electromagnetic field sensor

When a partial discharge activity takes place in an insulation defect, a part of the pulses energy is irradiated in space through the propagation of an electromagnetic field generated by impulsive charge recombination currents associated to PDs. This field can be detected by using an antenna geometrically designed in order to obtain the optimal bandwidth for PD detection. This kind of sensors allows to perform more safely PD measurements, without galvanic connections with the system under test, but is subjected to the action of disturbing external electromagnetic noise.

2.6.5 Prysmian Pry-Cam Wings

The Pry-Cam Wings is an electromagnetic PD sensor designed to sense the electromagnetic radiation generated by PD phenomena. The sensor is composed by two metallic plane electrodes: the first one allows to obtain a capacitive coupling with the cable shield, the second one - placed above the first one - detects the background noise. The active circuit embedded on the sensor allows to overcome the problems related to the degradation of the detected signal due to a) the attenuation effect depending on the connecting cable length and b) the reflection phenomena that cause the distortion of the real PD pulse waveform. The frequency bandwidth is from 5kHz to 50 MHz. The sensor provides also the synchronization signal and the temperature of the component where it is installed.

Chapter 3

System design and implementation

In this chapter, a custom electronic board implementing a fault-location technique and partial discharge detection is presented. The prototype henceforth will be named "Volo".

Volo is a microcontroller-based system implementing a dual-end or multi-end TW fault and PD location method and at the same time enabling to acquire a standard PD pattern. These capabilities combined in a single instrument are novel to the author's knowledge. Furthermore, also the local temperature of the point where the sensor is attached is registered.

The instrument was designed to work on both HV and MV cable lines. Even if the presented prototype can be seen as a proof-of-concept, much attention was paid in order to keep the total cost of the whole system reasonably low. The reason mainly relies on the desire to target also the distribution line market. In fact, medium-voltage utilities deal with a huge number of lines, hence many monitoring devices should be bought and installed in the grid. Even without performing a detailed cost-benefit analysis associated with the adoption of the presented asset monitoring tool, it is clear that a fault-location system should be not only effective, but also sustainable. Other similar system are reported in the literature such as in [45, 46].

The design of the proposed device is described in this section and the block diagram is shown in Fig. 3.1 and will be detailed in the next paragraphs.

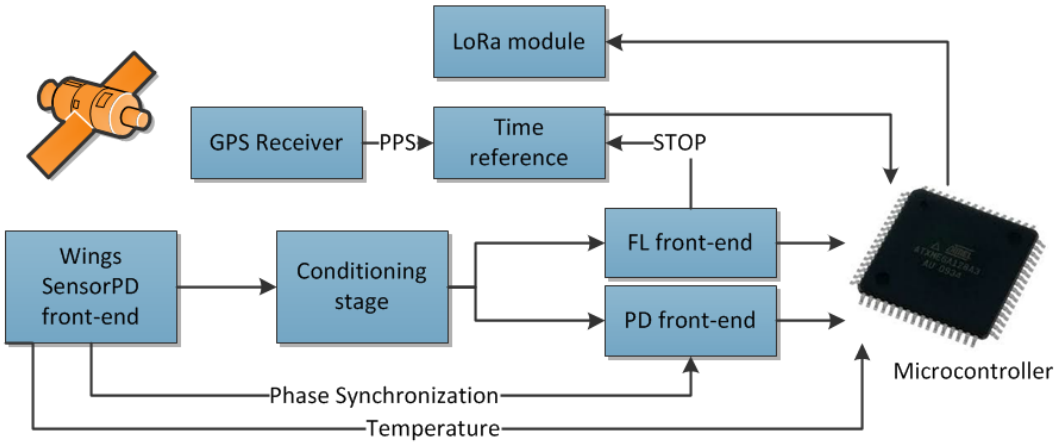

Figure 3.1: Block diagram of the proposed device.

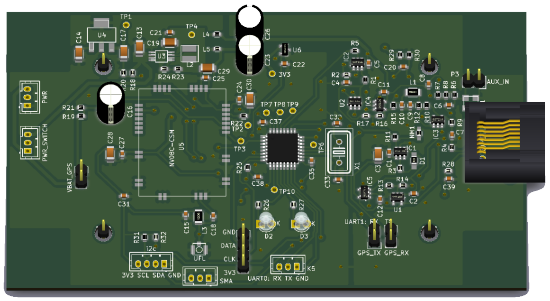

Figure 3.2: Rendering of the proposed device.

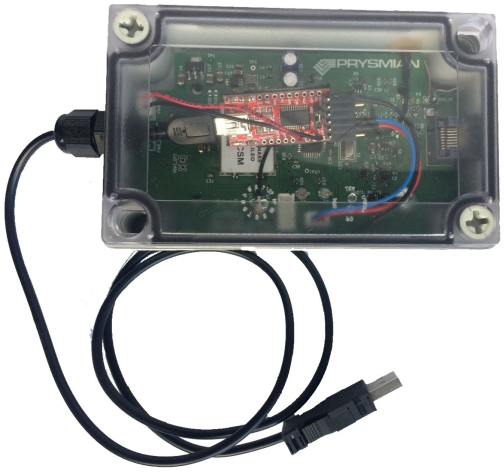

Figure 3.3: The prototype realized for the tests.

3.1 Sensor

Similar systems in the market make use of high frequency current transformers (HFCT), capacitive coupled sensors or current and voltage transformers (TA and TV). Volo has been designed to sense both PDs and fault pulses by using Wings sensors developed by Prysmian [47]. Wings sensors have wide bandwidth (500kHz-50MHz), good sensitivity (below 1pC for PDs) and a built-in digital temperature sensor. Volo has also an auxiliary input so it can be connected to other sensors without requiring, in many cases, further signal conditioning.

While Wings are generally used as partial discharge sensors, in this case, they will be used also for sensing traveling wave pulses associated to faults. In fact, fault pulses and partial discharges pulses observe similar behavior while propagating in transmission lines. When a fault occurs on a line, a fast transient is generated, which travels along the line and can be sensed by Wings sensors.

One big difference between PD and fault pulses is related to the signal amplitude, usually much higher for fault pulses. In fact, the way Volo discriminates between the two different pulses is based on the fact that a fault pulse will be perceived as higher amplitude pulse compared to the average amplitude of the PD pulses continuously acquired by the instrument. Of course, fault pulses which are generated far from the monitoring point will be attenuated by the line and could be mislead as PD pulses. However, this phenomenon will not be significant for lower distances between two Volo devices, in the normal scenario equal to maximum 1000 meters. Anyway, after a fault pulse, the intervention of the protection relays of the line will occur interrupting the power supply, hence the 50Hz (or 60Hz) synchronization signal will be lost and the fault pulses can be undoubtedly individuated.

Disturbances can generate other pulses which will be sensed as possible PDs as well. In this cases, the PD pattern representation can help the engineer to understand the nature of the pulses.

3.2 Analog front-end

The analog front-end designed for the Volo will be discussed from the point of view of each functional sub-part. As it can be seen from the signal conditioning block diagram in Fig. 3.1, the first stage of the chain is common for both PD and fault

parts. This stage converts the differential signal to single-end signal by means of a HF transformer as well as providing a small $\times 2$ additional gain to the input signal. In fact, the signal coupled to the Wing sensor is internally amplified by the active circuit of the sensor itself, so a high gain stage in the Volo is not needed. A final CLC pi-network provides a low-pass filter with a cut-off frequency of 30MHz.

The signal goes to the next conditioning stage directly or by passing through an inverting amplifier, by acting on a dual-pole single-throw analog switch driven by the MCU (`inv_pulse` signal). In this way both positive and negative pulses can be acquired. The resulting bandwidth of the first stage is 1-30Mhz.

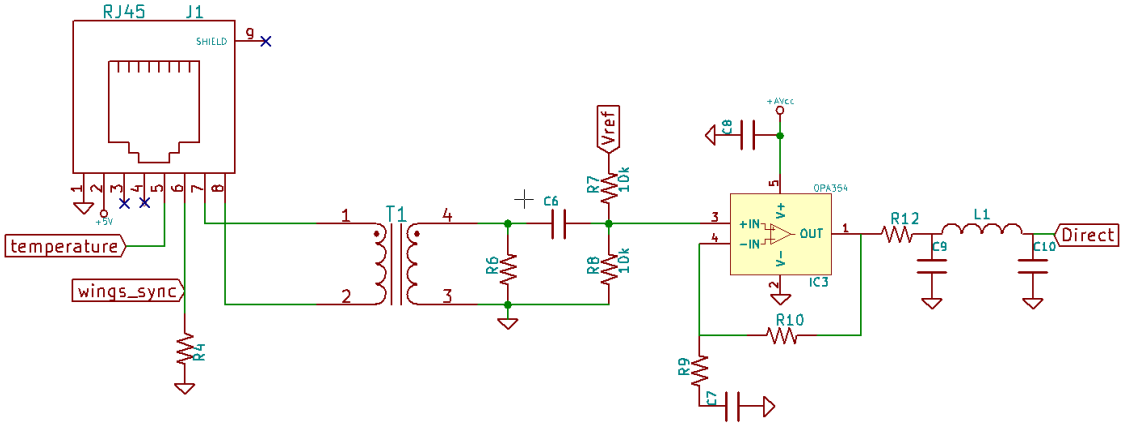

Figure 3.4: First stage of the analog chain.

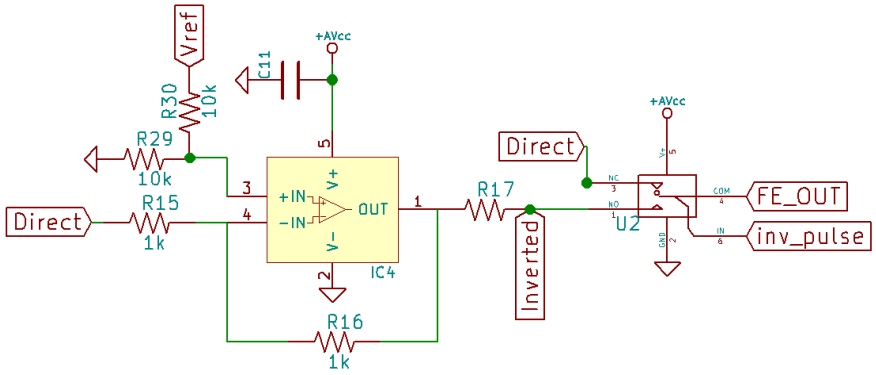

Figure 3.5: Inverting amplifier and analog switch.

3.2.1 PD pattern

Partial discharges pulses are processed by a peak detector. This stage consists in the proper peak detector cascaded with a buffer (Fig. 3.6). In Fig. 3.7 the screenshots acquired with the oscilloscope are shown. For testing this stage, a $200\,mV$ and $100\,ns$-wide pulse was applied at the input of the peak detector stage (yellow line). It can be noted a settling-time of less than $150\,ns$, while the value is kept for $50\,us$ (or $100\,us$ with some attenuation). The circuit can be reset by the microcontroller by activating the `DISCHARGE` signal, connected to an analog switch. In this way, the next input pulse can be quickly acquired. The MCU will in fact acquire via the 12bit ADC the hold value of the peak detector and discharge it. This operation is continuously performed every $1\,us$, which for a $50Hz$ supplying voltage corresponds to a phase resolution of:

$$PH_R = \frac{360°}{20\,ms} \times 1\,us = 0.018°$$

This means that a PD pattern can be acquired with a 12 bit vertical resolution with phase resolution of 0.018° by using a relatively low-end hardware. Furthermore, at each supplying voltage cycle (e.g. $20\,ms$), the input signal is inverted so both positive and negative pulses are acquired. In Fig. 3.8 it is shown an injected positive pulse acquired at the direct and inverted output of the first stage.

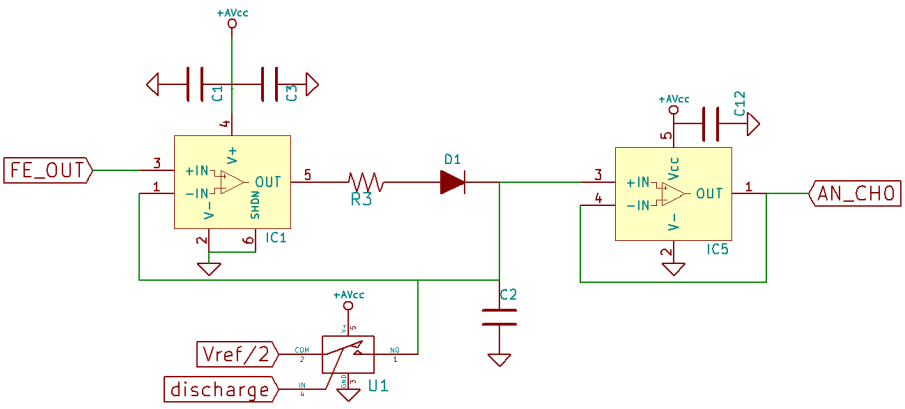

Figure 3.6: Schematic of the peak-detector stage.

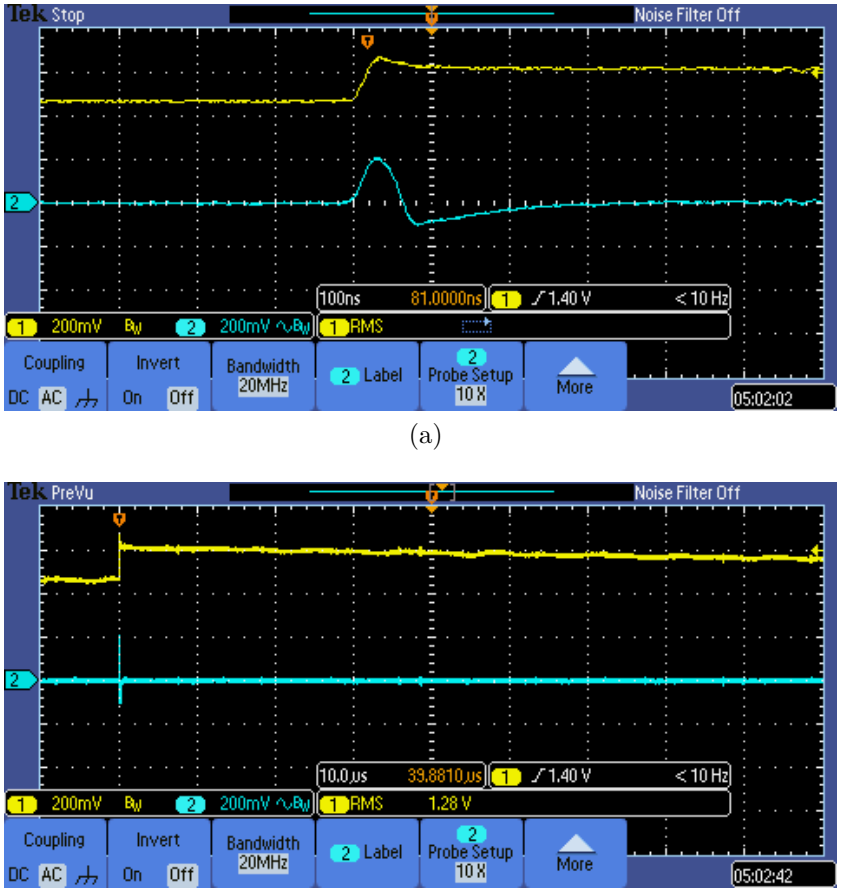

Figure 3.7: Peak-detector for PD pulses: (a) time-division at $100ns$ and (b) $10\mu s$, the input pulse is depicted in blue while the output peak is the yellow line.

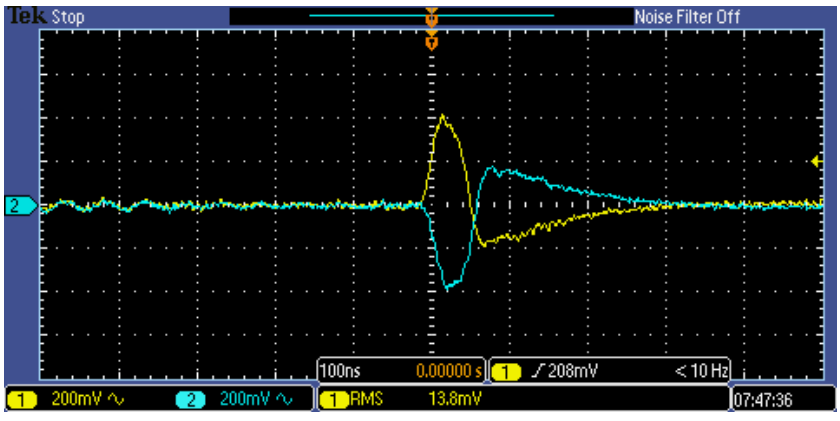

Figure 3.8: An injected positive pulse acquired at the direct and inverted output of the first stage.

3.2.2 Synchronization

As it is known, the phase resolved partial discharge pattern is basically a chart where the amplitude of each acquired pulse is plotted with respect to the phase angle at which the pulse was detected by the instrument. It is clear that a reliable phase synchronization is needed. Wings sensor is able to detect the phase angle of the voltage applied to the equipment where the sensor is placed. The 50/60Hz (or whatever the supplying frequency is) is sensed by the Wings, conditioned and given to the output as a square wave. In fact, the synch output of the Wing sensor is given as input to a GPIO of the MCU and thus used for drawing the pattern. Each pulse amplitude digitized by the ADC is saved in memory together with the phase angle.

3.2.3 Fault and PD pulses location

The signal conditioning of the fault pulses is performed by the first stage, already discussed above, cascaded with a analog comparator (Fig. 3.9). The threshold of the comparator is set by the DAC output of the MCU. In the current Volo implementation, threshold can be software configured via the UART interface depending by the noise level. When an input signal reaches the threshold level, the comparator provides a high output which is sensed by a GPIO input pin of the MCU, which triggers an interrupt routine. It can be noted that it was chosen not to acquire the pulse shape of the fault pulse. In fact, the approach followed for this FL method does not require any processing of the time-domain signal associated to the fault. The rising-edge of the fault pulse is detected by the comparator and the absolute time-stamp is taken. When two fault pulses are detected by two Volos installed at the two ends of the line and sent to the central server, the position of the fault is there calculated as in a Type D dual-end or multi-end TW FL method described in 1.3.4.4 on page 29.

This approach clearly simplifies the signal processing and the required hardware. A high-performance analog-to-digital converter is not requested since the rising-edge is detected with a threshold method as described in [48] (as well as other methods for estimating the time-of-arrival of PD pulses). At the same time, the high-resolution of the time-reference enables high-accuracy estimation of FL.

If the threshold of the comparator is set to a lower value also the PD pulses can be located. The threshold is decided in consideration of the noise level, in the way that it is as low as the noise level permits in order to have the minimum number of false triggers. This localization must be made in a certain phase angle range, i.e. if

PDs are detected from both Volos at the two ends of the line and on the same phase range, thus, per each phase value, the difference of the time-stamps of those pulses can be calculated and thus the estimation of the defect locations can be found. The accuracy can be significantly higher as compared to the localization of the fault, because PDs are a repetitive phenomenon so the average on multiple measurements can be successfully performed. In fault events up to three measurements could be performed, namely 1) the actual fault event, 2) reenergization of the line to seek for temporary fault and 3) final reenergization with consequent trip.

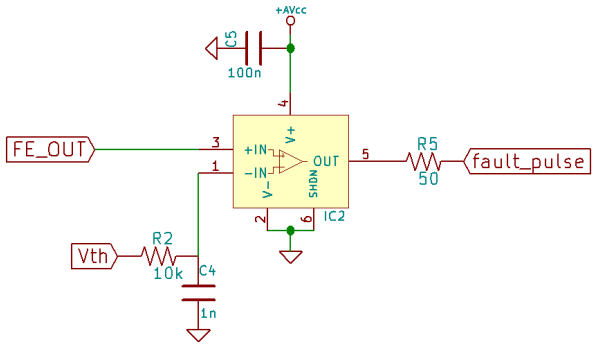

Figure 3.9: Fault-pulse stage.

3.3 Time-reference

As discussed, the proposed FL method does not involve high sampling rate/resolution ADC. On the other side, Volo achieves high performances by precisely time-stamping the arrival time of the fault pulse. Two important issues need to be discussed at this stage.

The first is how to synchronize two (or many) devices placed in relative far positions. One possibility is distributing a synchronization signal by using for instance a fiber optic link. Another possibility is having a very precise local clock on each device so, after a calibration in fab, they will keep the time with the certain level of precision needed by the particular application. Chip scale atomic clock (CSAC) are nowadays available on the market at reasonable prices for a military UAV, but unfortunately these prices are not as reasonably low for the distribution networks application.

The easiest way to keep devices synchronized is undoubtedly by taking advantage of GPS satellites. Modern GPS receivers can also use the signal of the Russian satellite navigation system, GLONASS. Many are already compatible with the future European system GALILEO. Most of the receivers, once the fixing process is established with a minimum number of satellites, can output a precise 1Hz PPS signal. These

pulses can be used by a MCU as reset for an internal timer. For instance, in the Volo, a GPS/GLONASS/GALILEO receiver is adopted with a PPS time accuracy of $15\,ns$ in the worst case.The PPS is used for resetting an internal timer that is configured to run at $64\,MHz$. When a fault pulse is received, the interruption freezes the timer and locally saves the current time-stamp. This is formed by last date and time received by the GPS plus the timer value. The result is a theoretical time resolution of $15.625\,ns$.

3.4 Communication

Devices like the Volo can be thought as the current implementation of the Internet-of-Things (IoT) applied to the industry - the so called Industry 4.0. Many Volo devices should be installed in different point of the HV or MV network and report critical information for the network asset management. Clearly, a suitable way for establishing the communication between a certain number of devices and the central site of the utility needs to be provided. In this paragraph, some possibilities are briefly discussed.

3.4.1 Local link

The microcontroller unit has two universal asynchronous serial receiver and transmitter (UART) units. One is internally used for communicating with the internal GPS receiver, while another is used as link to the external world. In particular, when the instrument is used as a standalone instrument, a PC can be connected directly to the device via a common USB-to-UART interface readily available on the market. A custom application, described in 3.6, has been developed for interfacing a Volo unit to the operator. This direct link to the operator PC is clearly extremely useful for calibration and testing, while, since the instruments are supposed to be installed in not safely accessible sites and should communicate between each other, other more suitable communication links are provided.

3.4.2 Bluetooth

Another possibility is offered by Bluetooth. A UART-to-Bluetooth interface was built (see Fig. 3.10) in order to be attached to the Volo and use the device without being directly connected to it. This could be useful for safety reason in case a test with high voltage is performed and a direct link to the device should be avoided.

The selected module is a relatively cheap Microchip RN4677 which supports both Bluetooth classic and Bluetooth Low Energy. When used in classic mode with a laptop, the operative system create a virtual COM port so the same software, described in section 3.6, could be used also with a Bluetooth link without any modifications.

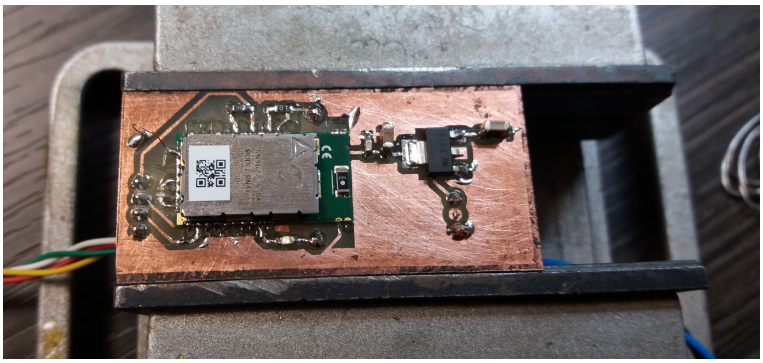

Figure 3.10: The Bluetooth module used for testing.

The Bluetooth link is still a kind of local link, only useful for testing purposes due to the very low range of its signal.

3.4.3 GSM/3G/4G

Volo units need a communication link toward a remote central site where the information coming by many (at least two) Volos are collected and analyzed. The fault-location minimum data which need to be sent to the central site, after a fault is detected, is actually quite small (i.e. down to 10 bytes), so even just an SMS could be enough for transferring the information. GSM/GPRS modem are available on the market and can be interfaced even to the cheapest microcontroller.

A more versatile communication link is offered by 3G/4G modems. These kinds of modems are usually more difficult to be handled by low-end MCUs. More advance embedded boards are requested for this task that, even if not very expensive in absolute terms, they can increase significantly the total cost of a single Volo unit.

The advantages of using mobile network for transferring information are listed here:

- wide signal coverage;
- a dedicated infrastructure is not requested;
- many modems available on the market from different supplier;
- use of the standard TCP/IP protocol.

The disadvantages are also reported:

- each unit requires a SIM card from the mobile operator;
- a suitable data plan is needed, thus increasing the total cost of ownership;
- coverage is not always reliable in rural areas;
- relatively high power consumption for battery operated devices.

3.4.4 WiFi

WiFi is probably the most widespread wireless communication link. Recently, cheap WiFi transceivers have became available on the market, allowing embedded designers to adopt WiFi communication easily. For this reason, also Volo can benefit of a WiFi link to the world. This solution has of course limitations. A WiFi access point (AP) should be available on site where Volo is installed. Nowadays public institutional WiFi access points (i.e. offered by the city for free) are spreading especially in cities down-towns. For devices installed in central zones covered by a public WiFi network, this could be probably a feasible option. However the reliability of such network is usually low as well as its security.

A more realistic infrastructure could be made by a specialized private network of WiFi access-points installed by the utility. This WiFi network could serve the many devices installed around the city. In the specific, this meshed WiFi network could be a sort of utility's local network or there could be at least one gateway to the internet. Rural areas, in the particular, could be very challenging to be covered following this method. In this case, special WiFi-to-3G/4G gateways should be adopted. Unfortunately the low coverage of standard WiFi APs makes this option difficult to be achieved, since many APs should be installed. It is worth noting that another limit consists in the maximum number of devices that can be handled by an AP: this is not actually a big problem since units do not need to be constantly connected, but they only require to be connected when it is needed sending data.

3.4.5 LoRa

LoRa® is a novel adopted wireless modulation technique perfectly suited when communication links with three characteristics are needed: low power, low bit-rate and long range. LoRa is based on a "Fractional-n synthesized chirp generator" [49], consisting in a frequency modulated (FM) chirp, which performs widely extended cover area range. An important note is that LoRa runs on unlicensed frequencies.

A single gateway provides coverage of several kilometers of radius. In an experiment performed by the author in Palermo, Italy, up to four kilometers of coverage was experienced in an urban environment. In another experiment in a rural area, up to ten kilometers of coverage was experienced. These examples simply confirm the claims of the LoRa Alliance of 2-5 km in urban environment and up to 10-20 km in rural. An entire region can be effectively covered with minimal amount of infrastructure.

Figure 3.11: The LoRa-to-UART (and USB) interface used for testing the coverage.

LoRa is in particular a physical layer (PHY- OSI Layer 1). On top on this layer, an OSI Layer 2 and above functions should be adopted in order to deploy a functioning wireless network system. LoRaWAN and Symphony Link are two standards built on top of LoRa.

In particular, LoRaWAN specifies a Low Power Wide Area Network (LPWAN) specification and system architecture based on open standards. It was created in 2015 by the non-profit LoRa Alliance, which is run by more than 190 companies, e.g. Semtech, IBM, Cisco, HP, Schneider, Bosch.

The features offered by LoRaWAN enable many applications in particular on smart grids [50]. LoRa, and in particular LoRaWAN, is a very attractive communication technique for implementing a large distributed network of asset monitoring devices, especially for the distribution network.

Volo was designed to operate with a LoRa transmitter, in particular the Microchip RN2483. This integrated module can be configured to work at 433 or 868 MHz and it is certified for the LoRa technology. The module already includes the LoRaWAN Class A protocol, thus it can operate in an existing LoRaWAN network.

It is also possible to disable the MAC and only use the LoRa physical layer. This feature was in fact used in this work for implementing a simplified communication protocol, due to the fact that there are not existing LoRaWAN networks easily available by the author and, at the same time, the complexity of the LoRaWAN protocol are not needed in this demonstrative application. It can be imagined that

the MV utility deploys its own LoRaWAN network or join the existing networks which may be active in some cities, in order to interconnect the many monitoring units installed on MV assets.

In order to test this principles, a simplified case was explored, in which two Volo units, each equipped with a LoRa module, communicate with a PC. The PC, in turn, has another LoRa module. Three USB/Uart-to-LoRa boards were designed in order to be connected to the Volo units and to the PC. One of the three units used during these test is shown in Fig. 3.11. The chosen frequency is the unlicensed 868MHz. The MAC was paused (`mac pause` command) so the LoRaWAN was not used. The two LoRa modules of the Volos were configured as transmitters while the PC one as receiver. The communication was stable in a range of 4km across the city.

3.5 Firmware

Here the firmware written for the microcontroller ATXMEGA16E5 is described. Most of the required tasks are performed by the interruption subroutines, while the main loop handles the communications and parses the commands received by the UART.

3.5.1 Initialization

Fist all the required peripherals are initialized and configured. The flow diagram is shown in Fig. 3.12 and briefly discussed.

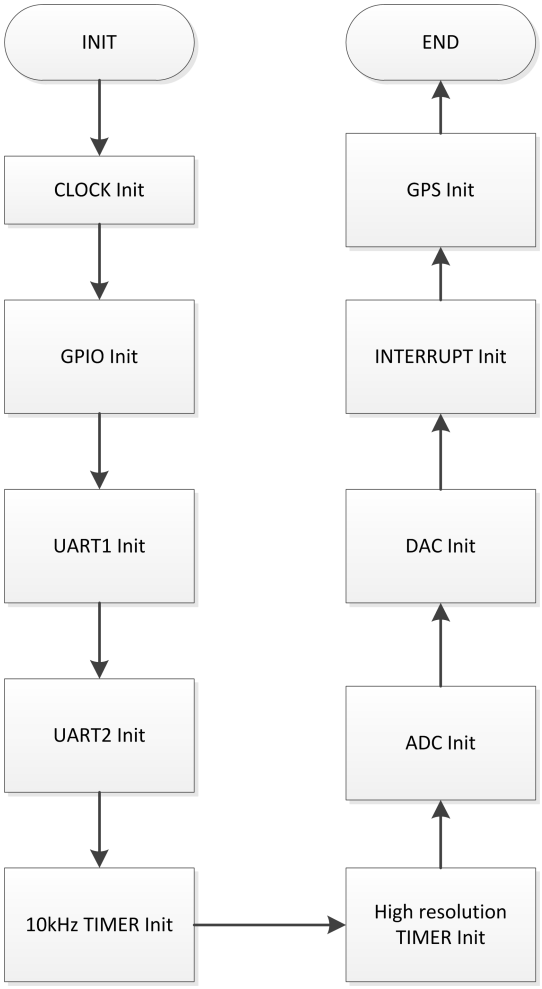

Figure 3.12: Flow diagram of initializations.

1. Clock init: this configuration is quite delicate and is shown in the flow diagram in Fig. 3.13. The 8Mhz external oscillator is used as input for the internal PLL. The multiplication factor was set to 8, hence a clock of 64 MHz was obtained. This frequency is actually above the clock limit of the microcontroller but even with this overclock the device was stable.

2. GPIO init: here the input and output pins are configured, as well as the interrupt source (PPS and Fault pulse).

3. UART1 init: the UART used for the GPS receiver is configured and a six-level buffer implemented. The configuration of the UART1 and UART2 is described in Table 3.1.

Baudrate	115200
Start bits	1
Stop bits	1
Data bits	8
Flow control	none
Parity	disabled

Table 3.1: UART1 and UART2 parameters.

4. UART2 init: the second UART is used for connecting the PC via a USB-to-UART interface, as well as the other optional modules:
   - Bluetooth module (custom made) shown in Fig. 3.10;
   - LoRa module (custom made) shown in Fig. 3.11;
   - Wifi module based on ESP8266.
5. 10kHz timer init: one timer was set in the way to have an interrupt every 100 us for the acquisition of the PD pattern.
6. High resolution timer init: the second timer was set at the maximum speed, that is the one of the CPU (64MHz). As discussed, higher is the frequency of the timer, the higher is the accuracy of the time stamp of the detected PD or fault pulse.
7. ADC init: the analog to digital converter of the microcontroller was set to 12bit of resolution and using the external 2.5V voltage reference. Gain of the internal amplifier was set at 1x and can be further changed by firmware.
8. DAC init: the digital to analog converter is used for setting the threshold for the comparator which detects the fault pulse. Also in this case, the external analog reference is used.
9. Interrupt init: the interrupt of all the levels are enabled (the global enable is then given inside the main loop). UART1 interrupt has medium priority, while UART2 has low priority. PPS and fault_pulse have highest priority.
10. GPS init: the GPS is configured to send a PPS pulse only after the proper satellites fix has been obtained.

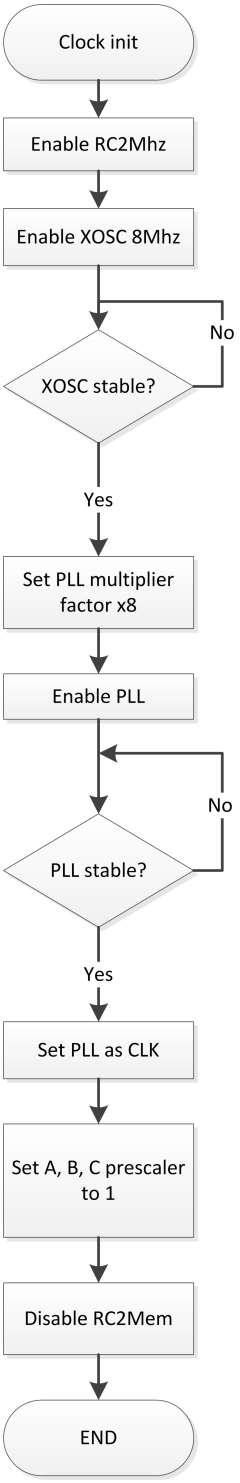

Figure 3.13: Flow diagram of clock initialization.

3.5.2 Main loop

After the initialization of all the peripherals, the main loop begins. The flow diagram is shown in Fig. 3.14. If the fault_pulse flag was set by the interrupt routine of the

high resolution timer, the time-stamp of the fault together with the counter value at the last PPS is sent via UART. Data, if any, received from the GPS receiver is then parsed for extracting the current date and time, fix status and number of satellites. Lastly, if a command was sent from the UART2 link, the parses routine implements the action requested by the user.

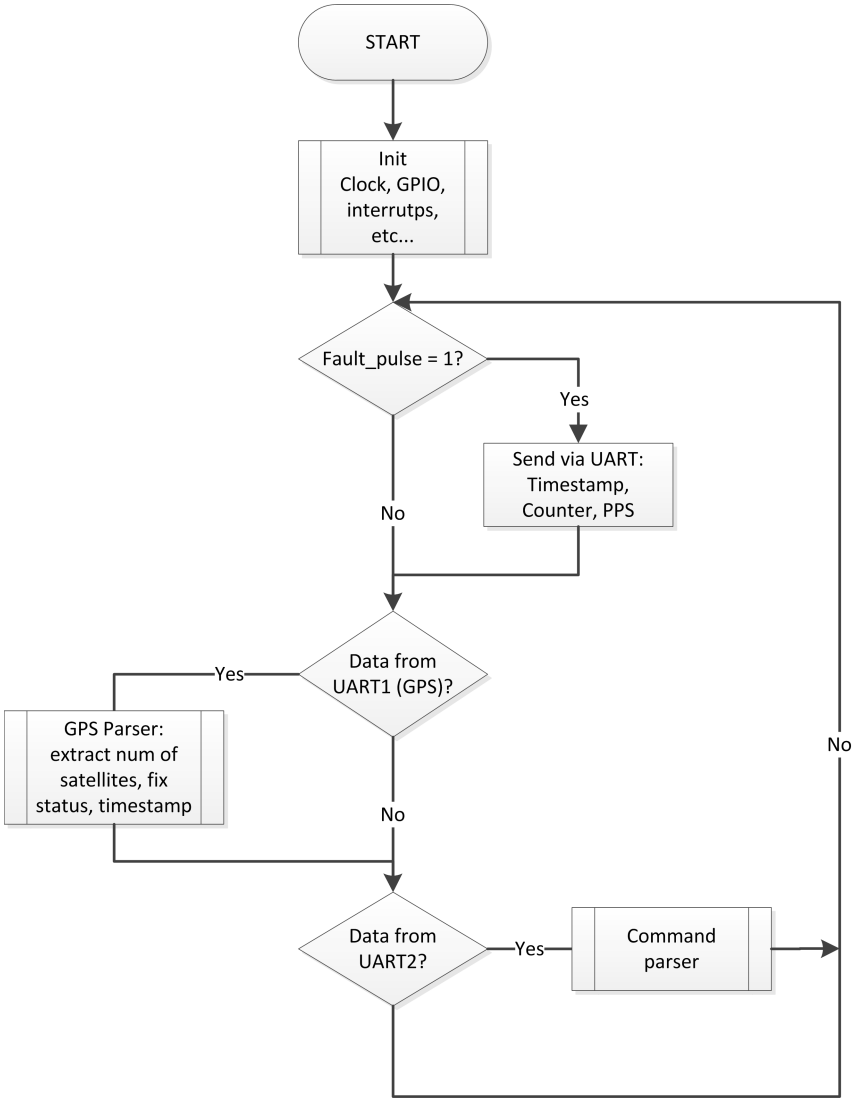

Figure 3.14: Flow diagram of main loop.

3.5.3 UART2 command parser

The flow diagram of the parser is shown in Fig. 3.15. The supported commands are:

- HI: the device responds with its name. This command is useful to see if the device responds and to check the firmware version.

– REC: the device switches to PD pattern mode, acquiring 256 pulses and then sending the resulting array via UART. Each pulse value is transmitted together with its relative phase angle value. For drawing a proper PD pattern, many REC commands will be needed. The application described in the next section implements this action.

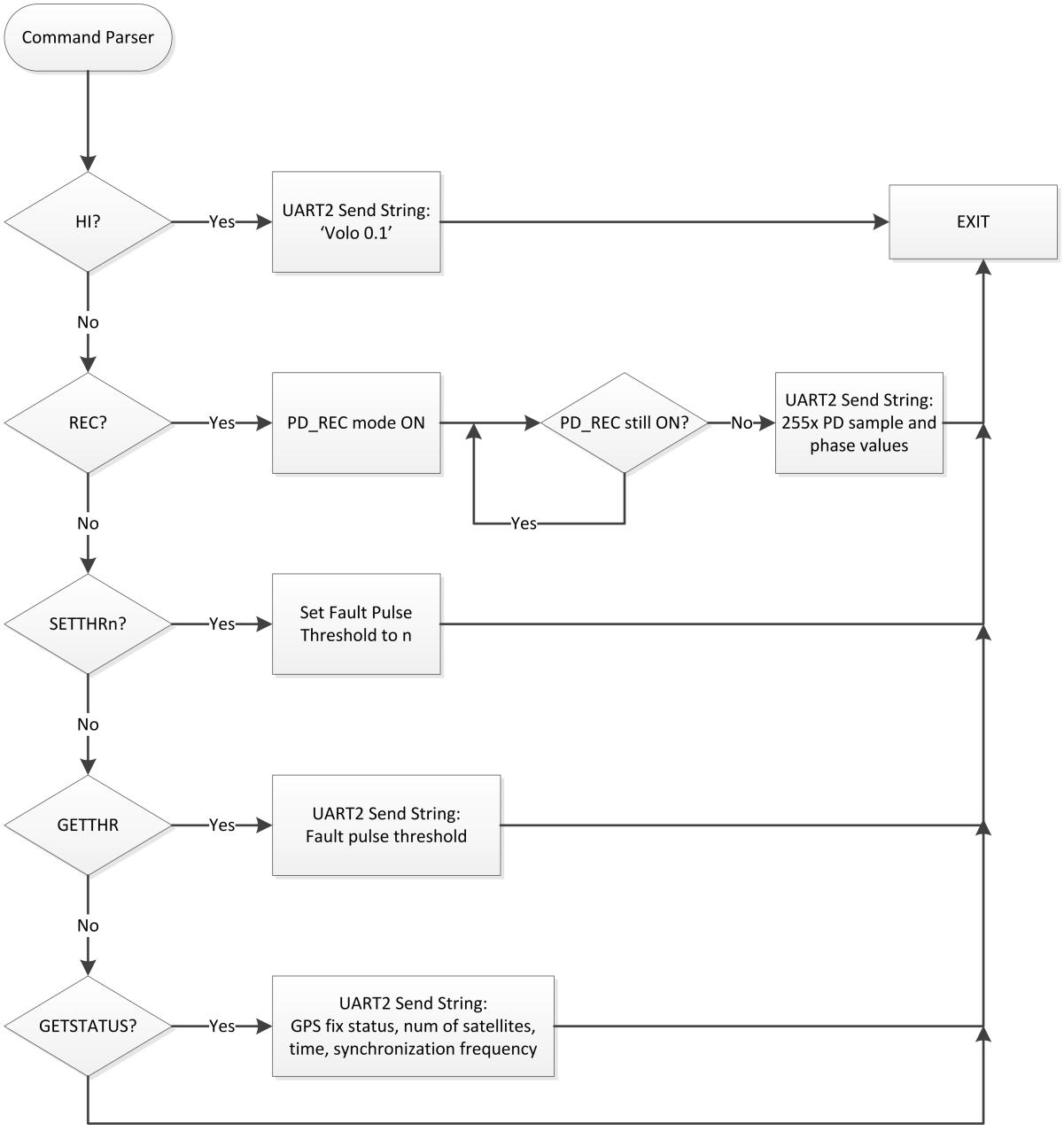

Figure 3.15: Flow diagram of the UART command parser routine.

3.5.4 10kHz Timer interrupt routine

The flow diagram is shown in Fig. 3.16. Every 100 us an interrupt request is triggered by the counter running at 1MHz and counting up to 100. The phase software counter is here first incremented. Then it is checked if the SYNC signal (coming from the sync pin of the Wings sensor) is active AND it was not during the last interrupt routine (prevSYNC variable). In this case, it means a new supplying voltage period was starting, so the period is calculated from the actual counter values: $period = phase \cdot 100 \times 10^{-6}$. Also, the phase variable is cleared.

If the PD_REC flag has been set by the UART1 command parser, following a REC request by the user, 256 samples are taken from the ADC. Between two samples, the capacitance of the peak detector is discharged for 10us. After all the sample have been taken, the PD_REC flag is cleared so the main loop sends data via UART.

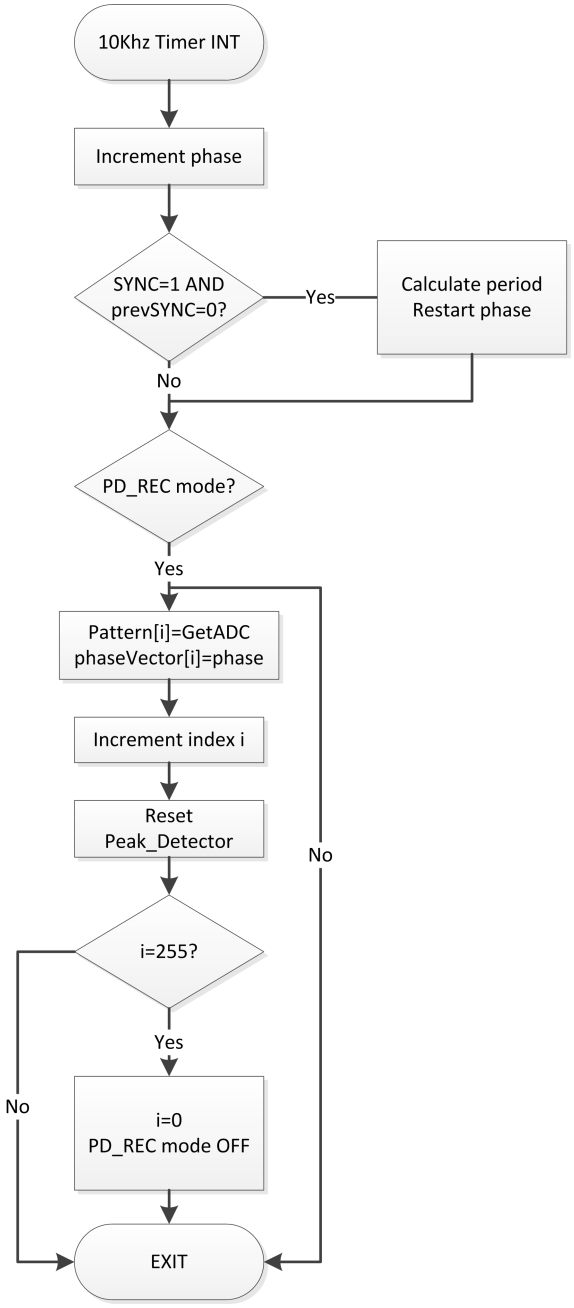

Figure 3.16: Flow diagram of the 10kHz timer interrupt routine.

3.5.5 High resolution timer interrupt routine

The flow diagram of this simple interrupt routine is shown in Fig. 3.17. The role of the high resolution (HR) timer is to provide the less significant (but most important) part of the time-stamp. The GPS sends a PPS every second and between two PPS pulses the high resolution timer running at 64MHz overflows many times due to its size (16bit). At each overflow, this interrupt routine increments a software counter, so that when a fault pulse is detected, the final time-stamp results from

the summation of the data/time obtained by the GPS NMEA messages plus the software counter (counting the overflows) plus the very value of the high resolution counter.

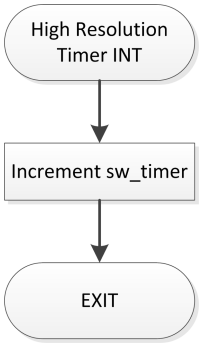

Figure 3.17: Flow diagram of the 64Mhz timer interrupt routine.

3.5.6 PPS and Fault interrupts

This interrupt may be triggered by the PPS of fault_pulse signal. Flow diagram in Fig. 3.18. The HR counter value is saved in a variable "timer_value" as first thing and then the software timer is summed up as well. Then, if the PPS signal is active, meaning that the interrupt was triggered by the PPS and not by the fault_pulse pin, the timer_value is associated to the PPS_value variable, used for correcting the counter value via the formula (4.1).

If PPS was not active, thus a fault_pulse was detected and the relative flag is set. At this point the main loop at the subsequent iteration sees the fault_pulse flag ON and will outputs the data via UART2.

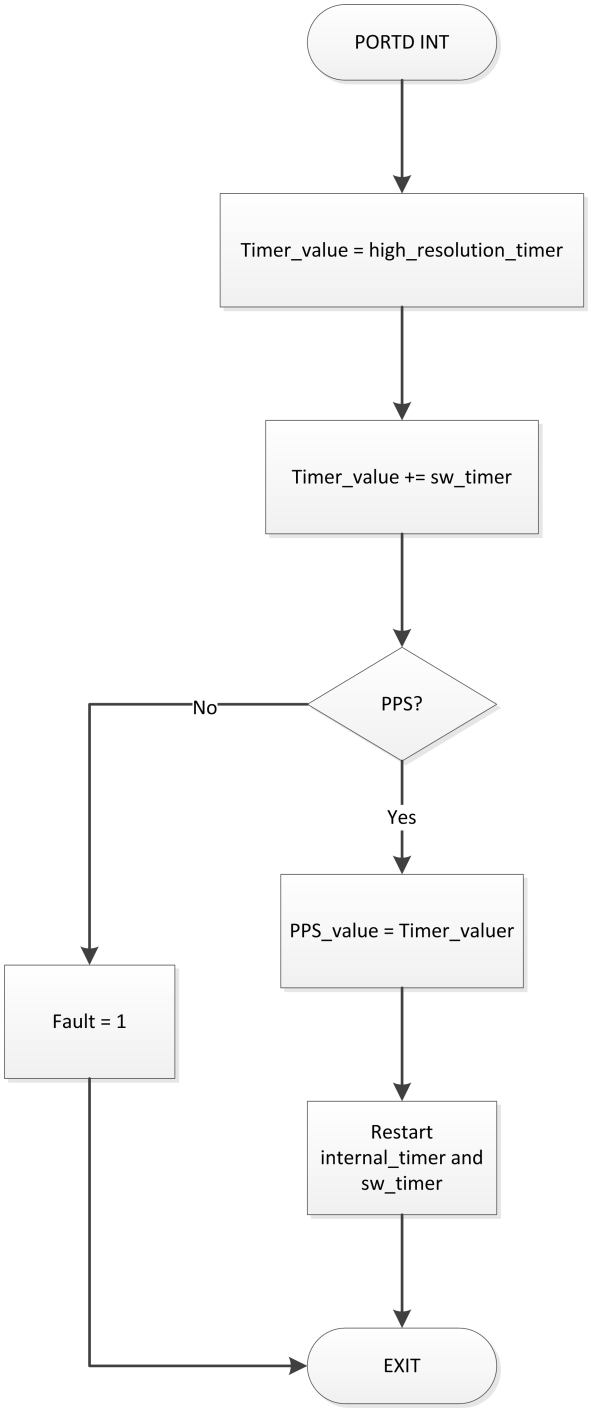

Figure 3.18: Flow diagram of PPS and Fault pulse interrupt routine.

3.6 Software

An application was developed for acquiring and drawing the PD pattern. The application was developed in Processing 3 (Fig. 3.19), an IDE based on Java which provides high level libraries and enables fast prototyping.

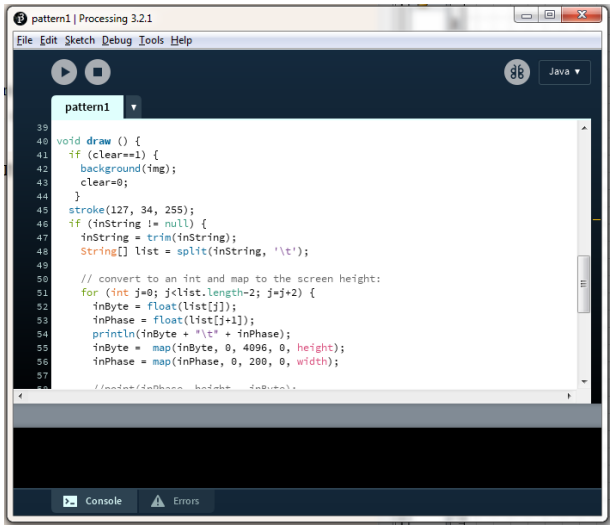

Figure 3.19: Processing 3 IDE.

The application is composed of three methods. The setup() method opens the serial port, sets the background of the window and send the first "REC" command to the Volo.

The serialEvent() method is triggered when data is received from the serial port: in this method, data composed by 256 couples of values (PD amplitude and phase angle) is read and saved to an array and another REC request is sent.

The draw() method splits the string (obtained by the serialEvent() method) after each tab character ('\t'). Each sub-string is then converted to float and a point is drawn per each coordinate (phase_angle, PD_amplitude). The flow diagram of the three methods is shown in Fig. 3.20, 3.21a and 3.21b.

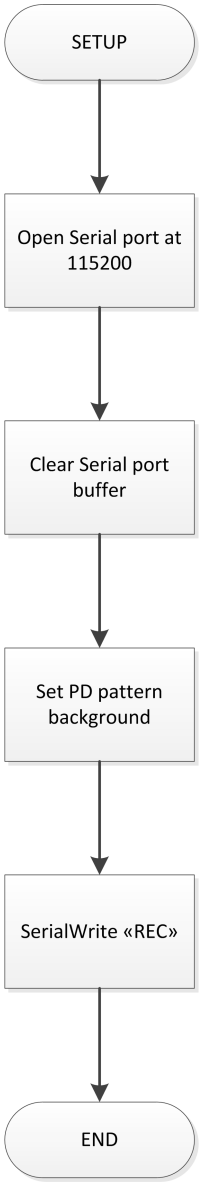

Figure 3.20: Flow diagram of setup method.

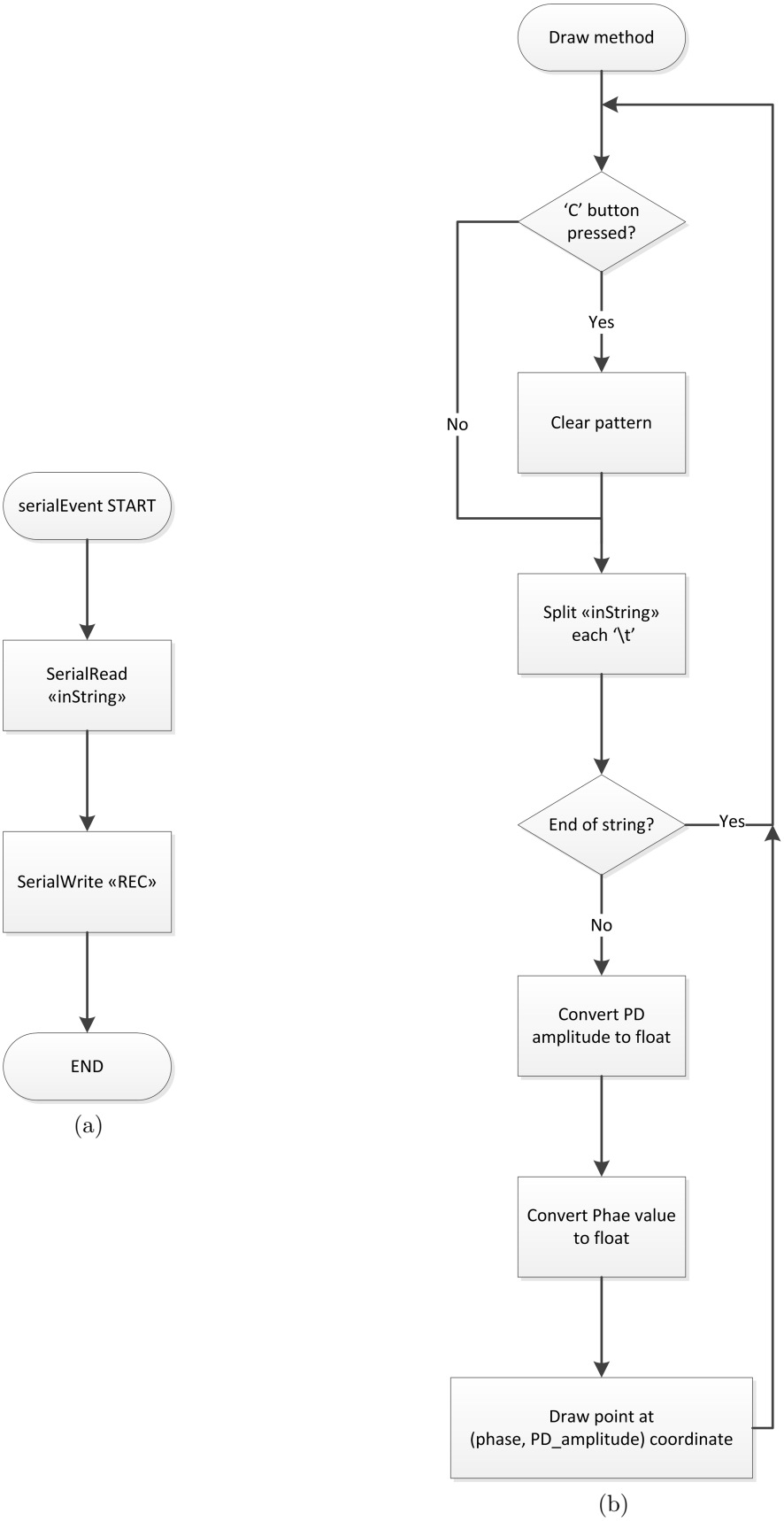

Figure 3.21: Flow diagram of SerialEvent() (a) and draw() method (b).

Chapter 4

Experimental results

In order to validate the system, different tests on the prototypes have been performed. Some simple tests could be performed in the electronics laboratory, while other advanced tests were performed in Prysmian R&D Energy laboratories in Milan. The first tests allow to prove the working principles on which the Volo is based and to make considerations about the accuracy.

4.1 Characterization of the device

The first tests involved the use of only one prototype. A single Volo was used without the GPS receiver, which was temporarily disabled. The PPS signal of the GPS was simulated by using an external arbitrary voltage signal generator; in particular a pulse signal with the parameters shown in Table 4.1 was selected. At the same time, an external PD-like pulse was injected to the input of the prototype. The parameters of the signal generator for the PD input, taken by the second output channel of the instrument, were similar to the PPS ones, with amplitude, phase and frequency changed during the tests.

Parameter	**Value**
Amplitude	3.3V
Offset	1.65V
Frequency	1Hz
Pulse duration	1us
Rise-time	20ns

Table 4.1: Parameters of the simulated PPS signal.

The prototype was powered and an UART-to-USB interface was used to connect

the unit to the PC (Fig. 4.1). The Volo provided at each PD-like pulse the value of the internal counter via the UART link. At the beginning, the frequency of the two generated signals was set at the same value so the Volo gave a null value of the counter, as expected. Then the phase of the two signals was changed and the value of the counter correctly represented the time difference between the two pulses generated at the CH1 and CH2 of the signal generator.

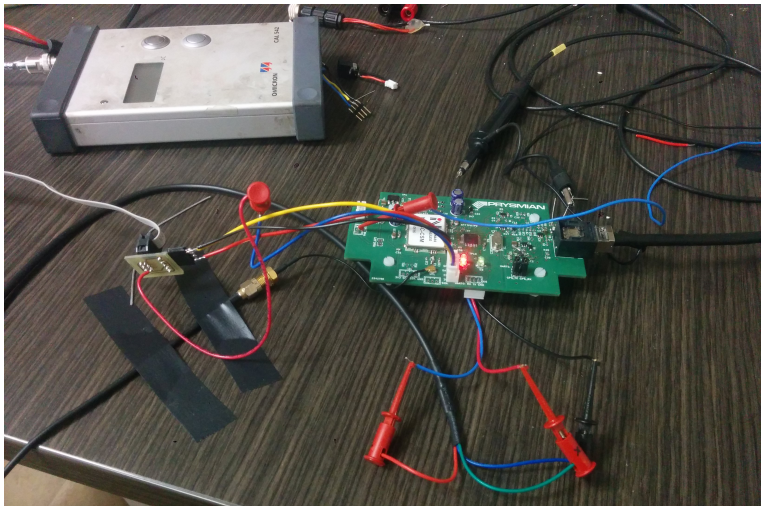

Figure 4.1: The prototype during the preliminary tests.

A second test, was carried out using two Volo units with the same applied signal. Also in this case, the GPS was disabled and the PPS supplied externally. The aim of this test was to see if two units provided the same counter output under the same conditions. As it was expected, there were significant differences on the two output values of the prototypes. Together with the value of the counter in correspondence of the fault-like signal, it was also provided, via the UART link, the value of the counter at the PPS, before resetting the counter. The result was that each prototype counted a different number of cycles between two PPS. This was expected since the nominal 8 Mhz quartz feeding the 32 MHz clock (multiplied via the PLL) has clearly a certain degree of tolerance, so the oscillating frequency can be slightly different from the nominal value. As it is known, also the temperature impacts on the oscillator frequency. The trending of the counter values at each PPS pulse was registered for 4 minutes and it is shown in Fig. 4.2. The counter values were converted in seconds.

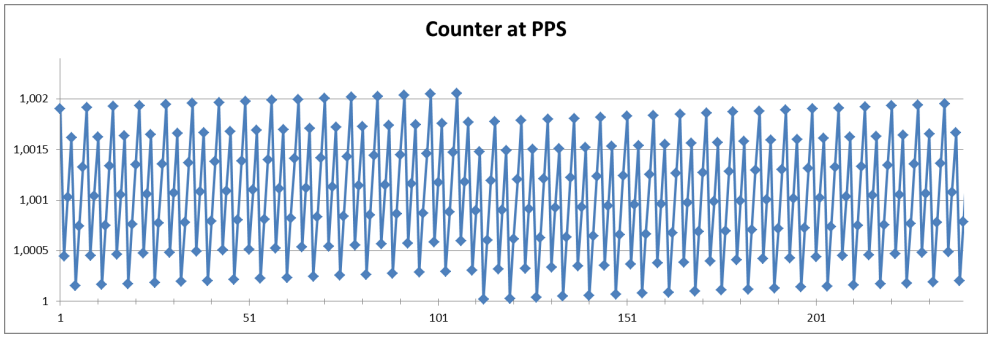

Figure 4.2: Counter value at each PPS pulse for 4 minutes.

These differences can be accounted and corrected by the following equation:

$$CNT_c = \frac{CNT \cdot CNT_{nom}}{CNT_{PPS}} \tag{4.1}$$

where:

CNT is the value of the counter when the fault pulse is detected;

CNT_{nom} is the theoretical nominal value of the counter for a perfectly calibrated oscillator (32000000 per 32Mhz or 64000000 per 64Mhz);

CNT_{PPS} is the value of the counter at the PPS signal, before resetting the counter.

An example is provided in Table 4.2. ΔT_C is given by multiplying the difference between the two CNT_C by the increment period of the counter ($1/T_{CLOCK}$) that in this example is 32MHz. For the spatial error it is supposed a propagation speed of $160\,m/us$.

Unit 1		
CNT	CNT_{PPS}	CNT_C
20657363	32000313	20657160.9
Unit 2		
CNT	CNT_{PPS}	CNT_C
20657229	32000106	20657160.5
Difference		
ΔCNT_C	ΔT_C	Spatial error
0.4	12.5 ns	2 m

Table 4.2: Example of corrected counter values for two Volo units.

4.2 Testing localization on a coaxial cable

A drum of coaxial cable, shown in Fig. 4.3, was used for evaluating the effectiveness of the proposed method. The coax cable was manually measured as 124.6 meter. A cut was made at x=84.6 m and the two sides jointed, enabling the possibility to inject an external signal from this position.

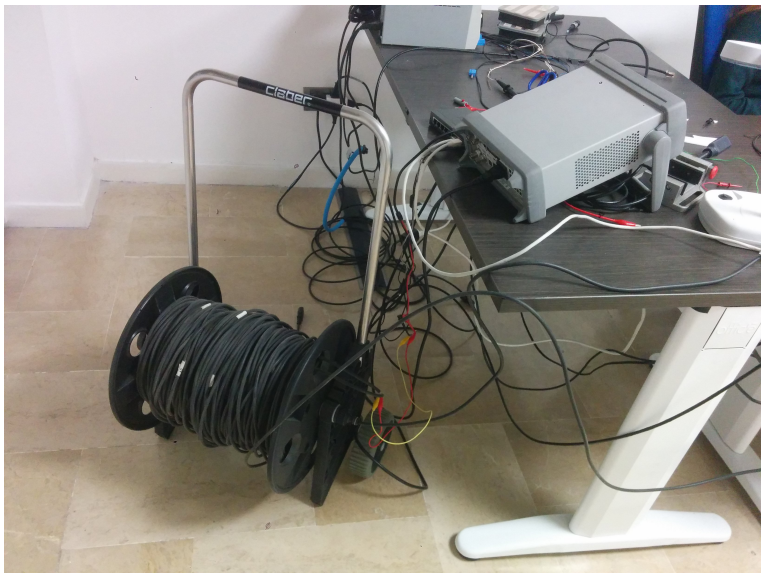

Figure 4.3: Coaxial cable drum.

4.2.1 Calibration

First of all the propagation speed was found. The two ends of the cable drum were connected to the oscilloscope (Tektronix DPO 2024 200MHz 1GS/s) and a pulse applied to one end of the cable. The external signal was supplied by the signal generator and, in the specific, a 1 us-width pulse was selected with an amplitude of 10V. The resulting acquisition of the oscilloscope is shown in Fig. 4.4. The yellow line represents the signal acquired at the first end of the cable drum (x=0 m), while the blue line is the signal taken from the second end (x=124.6 m). The time difference between the two peaks measured at the first and second end was 634 ns. The propagation speed estimation can be calculated as:

$$v_p = \frac{124.6\,m}{634\,ns} = 196.5\,m/us$$

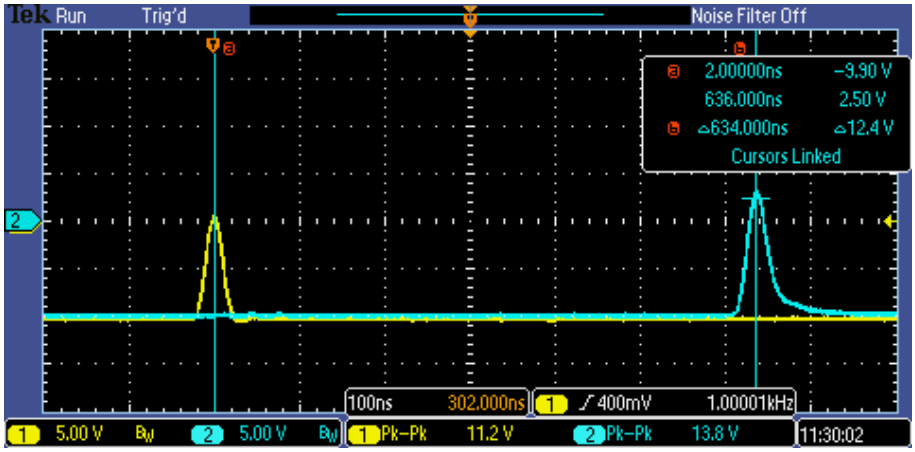

Figure 4.4: Scope acquisition for the calculation of the coax cable propagation speed.

By the knowledge of the propagation speed of this cable drum, the same pulse was injected from the "defect" of the cable (x=84.6 m). The acquisition of the oscilloscope is shown in Fig. 4.5. The time difference of the two acquired pulses was 228.4 ns. The defect location can be calculated by the expression used for Type D traveling wave localization approaches in Section 1.3.4.4.

$$x_F = \frac{L}{2} + \frac{1}{2} v_p \Delta t = \frac{124.6 + 196.5 \times 10^6 \cdot 228 \times 10^{-9}}{2} = 84.7\, m$$

By using the oscilloscope method, the estimation of the defect location is very precise, provided that the cursors (i.e. the two vertical lines in blue in Fig. 4.5) used for measuring the time interval are set accurately.

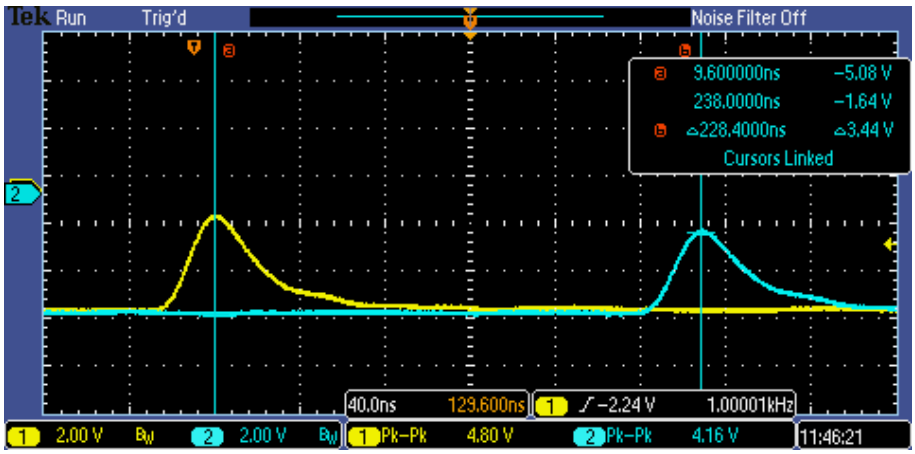

Figure 4.5: Scope acquisition for the calculation of the coax cable propagation speed.

Two Volo units were used, each connected directly to the two ends of the cable drum, that is $x_A = 0\, m$ and $x_B = 124.6\, m$. The Wings sensors have not been used in this test, so the the two ends of the cable were connected to the input of the two

prototypes, as shown in Fig. 4.6. The GPS receiver were not used initially so the PPS signal was also supplied by the second channel of the signal generator.

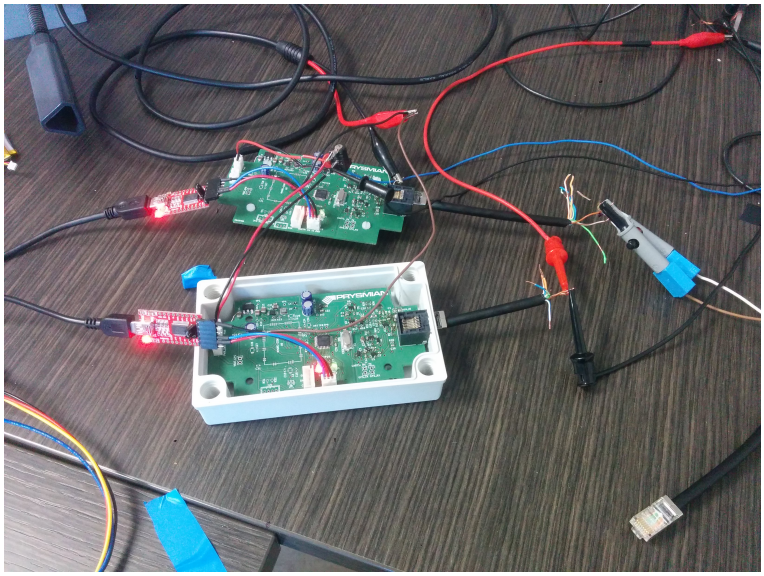

Figure 4.6: Two Volo units during test on the coaxial cable drum.

Initially, the clock frequency of the prototypes was set to 32 MHz and the normalization of the counter values was performed using the (4.1). The time difference obtained by combining the two Volo units was 204.4 ns, eventually providing a fault distance:

$$x_F = \frac{L}{2} + \frac{1}{2} v_p \Delta t = \frac{124.6 + 196.5 \times 10^6 \cdot 208.6 \times 10^{-9}}{2} = 82.8\, m$$

Unit 1		
CNT	CNT_{PPS}	CNT_C
24981530	32000361	24981248.2
Unit 2		
CNT	CNT_{PPS}	CNT_C
24981496	32000326	24981241.5
Difference		
ΔCNT_C	ΔT_C	Distance
6,7	208.6 ns	82.8 m

Table 4.3: Example of corrected counter values for two Volo units.

The result shown in Table 4.3 is approximately 2 meters less than the real defect position.

The test was repeated by setting the internal CPU clock at 64MHz. In this case the time difference was 224.7 ns, corresponding to:

$$x_F = \frac{L}{2} + \frac{1}{2} v_p \Delta t = \frac{124.6 + 196.5 \times 10^6 \cdot 225.5 \times 10^{-9}}{2} = 84.5\, m$$

Unit 1		
CNT	CNT_{PPS}	CNT_C
49913536	64000646	49913032.2
Unit 2		
CNT	CNT_{PPS}	CNT_C
49913226	64000228	49913046.6
Difference		
ΔCNT_C	ΔT_C	Distance
14.4	225.5 ns	84.5 m

Table 4.4: Example of corrected counter values for two Volo units.

As it is expected, the resolution of the timer mainly determines the precision of the measurements, hence higher counter frequency enables better distance estimation accuracy. Table 4.4 lists the results.

4.3 Test on a MV cable

A second tests session was performed inside Prysmian R&D HV laboratories in Milan. Here a MV cable drum was provided for testing the prototype on a typical cable for the distribution network. The cable length was measured in 240 m. The propagation speed was also calculated by means of a TDR instrument, the Intereng Interflex 130. Since the length of the cable was known, the propagation speed was adjusted until the exact cable length was measured. The obtained value was approximately 160 m/us. Fig. 4.7 shows both the cable drum and the TDR device. This MV cable drum has a "defect" at 95 m from the first end. This defect was made by inserting a screw deep into the cable to touch the conductor and another screw till the screen, as shown in Fig. 4.8. In this way it was possible to inject a signal from that position.

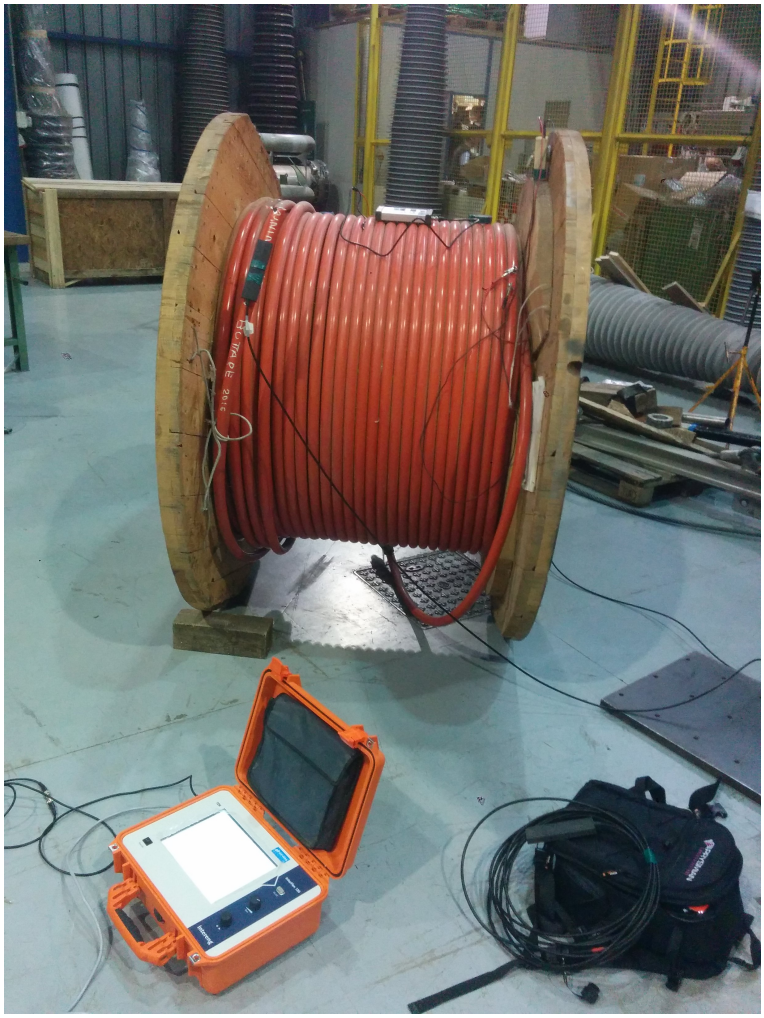

Figure 4.7: MV cable drum and TDR instrument.

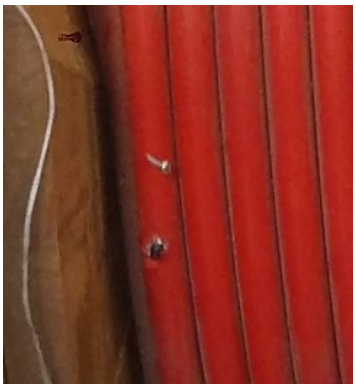

Figure 4.8: Screws inserted inside the cable to the screen (top) and to the conductor (bottom).

4.3.1 Localization of the defect with injected PD pulses

Two Wings sensor were attached to the two ends of the cable drum and each sensor was connected to the respective Volo unit. Even if the test was performed inside the R&D hangar, the GPS antennas were put outside so the GPS receivers could be enabled.

(a) (b)

Figure 4.9: Wings sensors attached to the two sides (a) and (b) of the cable drum.

A signal generator was used for injecting PD-like pulses from the "defect" of the cable, with an amplitude of 10V and 1Hz frequency. On each Volo unit the threshold for discriminating the fault pulse was set in order to sense the artificial injected pulse. The two Volos were connected to the same laptop PC and the measurements logged in different files. By using the propagation speed found thanks to the TDR device, the location of the defect was estimated as 92.9 m, that is 2.1 m different than the actual location.

$$x_{PD} = \frac{L}{2} + \frac{1}{2} v_p \Delta t = \frac{240 + 160 \times 10^6 \cdot 338.8 \times 10^{-9}}{2} = 92.9\, m$$

The time-difference used for computing the location of the defect was obtained by performing the average of multiple measurements, since the injected pulses were applied to the cable for about 2 minutes.

Unit 1		
CNT	CNT_{PPS}	CNT_C
20211012	64000940	10105357.6
Unit 2		
CNT	CNT_{PPS}	CNT_C
20210860	64000390	10105368.4
Difference		
ΔCNT_C	ΔT_C	Distance
21.7	338.8 ns	92.9 m

Table 4.5: Example of corrected counter values for two Volo units.

4.3.2 Localization of the fault section: test with DC voltage

Unfortunately, it was not possible to test the prototypes at typical voltages of distribution networks. However, the MV cable drum was feeded with 30V DC with an external power supply. At the defect position, the two screws connected the main conductor and to sheath, respectively, were shorted by a switch at different intervals. The resulting pulses were sensed by the two Volo units and the resulting time-stamps sent to the laptop by means of the UART link. The distance to the fault was found to be 94.6 m.

$$x_F = \frac{L}{2} + \frac{1}{2} v_p \Delta t = \frac{240 + 160 \times 10^6 \cdot 294.3 \times 10^{-9}}{2} = 96.46\, m$$

Unit 1		
CNT	CNT_{PPS}	CNT_C
41372804	64000936	41372198.9
Unit 2		
CNT	CNT_{PPS}	CNT_C
41372466	64000384	41372217.8
Difference		
ΔCNT_C	ΔT_C	Distance
18.8	294.3 ns	96.46 m

Table 4.6: Example of corrected counter values for two Volo units.

Also in this case, the time-difference used for the calculation was taken by averaging multiple measurements. The presence of noise could in fact impact the measured time-difference if a single sample from both the Volos is used. When just a single couple of samples is used for calculating the fault location, the error increased up

to 10 meters. As it was previously stated, also in case of faults, more than one measurement could be performed. In fact, different attempts of reenergizations are usually performed by the DSO/TSO, thus improving the distance estimation as in a two-ends Type E FL method.

4.4 Acquisition of PD patterns

As discussed, the Volo is capable of acquiring a PD pattern. The PD pattern is acquired on background and transmitted via UART, which can be in turn connected to a USB-UART, WiFi or LoRa interface. If a fault pulse is detected, this event has higher priority on the PD pattern acquisition.

In order to test the PD pattern acquisition, a standard PD calibrator was used. In particular tests were performed with an Omicron CAL 542. Different amplitudes were selected and the prototype was able to see down to 1pC. In Fig. 4.10 it is shown the PD pattern acquired by the Volo for 1pC and 10pC amplitude pulses. As it can be noted, the Omicron calibrator generates six pulses per cycle. The calibrator was synchronized by means of light source, while the Volo took the synchronization from the Wings sensor itself (the low voltage AC cable feeding the desktop lamp was put close to sensor).

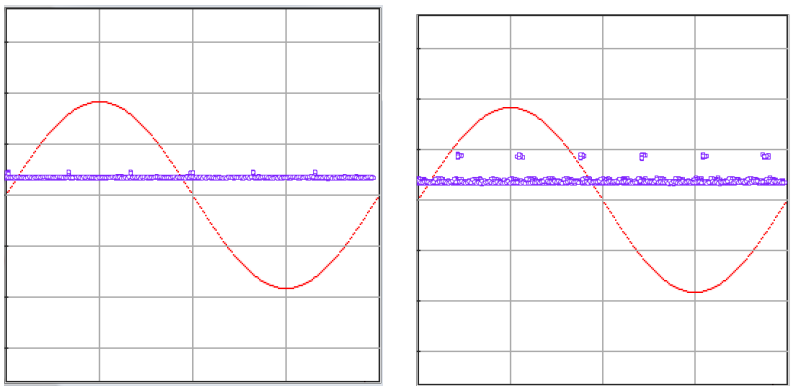

(a) (b)

Figure 4.10: Pattern acquired with a PD calibrator at 1pC (a) and 10pC (b).

A further test was performed by creating an artificial corona effect on a small 20kV cable loop. The test loop is shown in Fig. 4.11 where the sensor was circled in red. The corona effect was generated by connecting a short copper wire with a metal needle attached to the first end of the cable termination, where the generator was connected. The Wings sensor was attached to the cable near the termination and

connected to the Volo, which was put outside the test fence. Voltage was applied and at 5kV AC the resulting pattern is shown in Fig. 4.12.

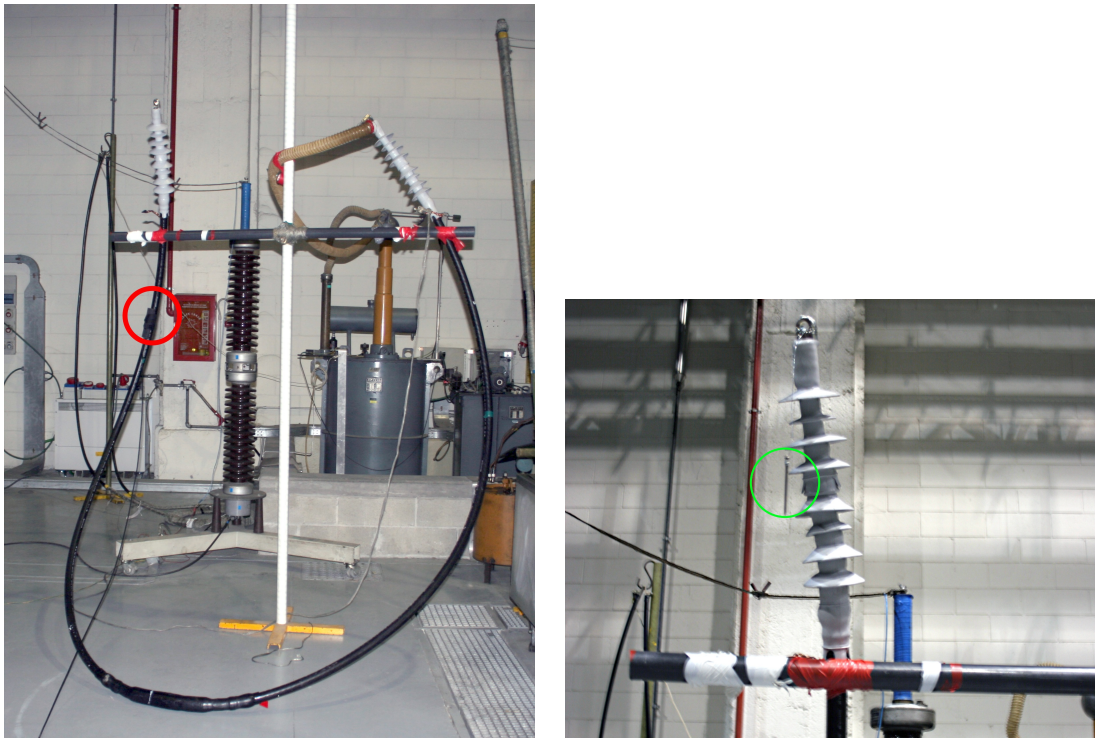

(a) (b)

Figure 4.11: Test setup for the acquisition of the corona effect: the cable loop with the sensor highlighted in red (a) and the needle in green (b).

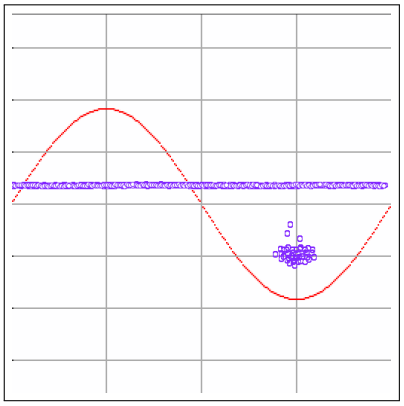

Figure 4.12: Corona generated on a 20kV cable.

Chapter 5

Conclusions

In this thesis, it was discussed the thematic of fault localization and condition based maintenance. Partial discharges measurements can be indeed exploited for locating defects on the cable system even before they become a fault. The major number of faults are in general related to a previous emission of partial discharge pulses from the defective point. These pulses travel on the line on the two directions at a certain propagation speed of the cable. At the same way, the fault event generates an abrupt voltage and current variation which in turn produces a fast traveling pulse. It was discussed how these two kind of pulses have similar characteristics, thus can be sensed by the same sensor and processed by the device proposed in the thesis, the Volo.

The traveling wave based methodology for localizing the defect or fault on the cable system proposed in this work requires at least two Volos installed on the same line. PD or fault generated pulses trigger the two devices at their arrival, producing precise time-stamps which can be used for computing the defect or fault location.

One particular feature of the device is that the pulse shape must not be acquired. On the contrary, a comparator threshold-based method is used for discriminating when a fault or PD pulse occurs and the precise time-stamp is provided by a high resolution timer. The time and date synchronization of the devices is enabled by GPS, which is used in turn for correcting the clock differences of the Volos.

Together with the estimation of the location of the defect or fault section, Volo is also capable to acquire the phase resolved partial discharge pattern, which is useful to understand the kind of defect insisting on the accessory of the power cable system, before it turns to a fault. All the principal PD patterns were introduced and their main features thoroughly discussed.

Furthermore, the temperature of the cable where the sensor is installed can be also

acquired by the Volo. This information can be thus correlated to the evolution of the PD pattern as well as the estimated location of defective part of the line.

All these capabilities are combined in a single device which was designed keeping the "low cost" as an important bullet of the specifications list. In fact, the idea is having a relative wide number of smart Volo devices installed in the MV/HV grid, as in the new paradigm of Industry 4.0. Those devices will provide "big data" which may be collected by a centralized monitoring server. Specialized algorithms can extract information relative to, as discussed, fault events and their location on the line, location of PDs source, PD patterns and temperature of the portion of the cable where the sensor is installed.

Efficient ways for the communication of the wide network of Volos were analyzed and discussed. In particular the LoRa wireless modulation was promoted as the most promising for covering extended areas with a minimum number of gateways, thus minimizing costs and power consumption of the devices. The tests performed with custom designed LoRa transmitters proved the effectiveness of this modulation in terms of area coverage.

The features offered by Volo were first tested in the laboratory in Palermo in order to characterize the device. Furthermore, other tests were performed in Prysmian R&D Energy Laboratory in Milan. The tests evidenced the correctness of the locating algorithm and it was shown that the estimation accuracy improves when performing multiple number of acquisitions for the same phenomenon. This is of course valid for PDs location being these a repetitive phenomenon per certain phase angle. In some circumstances, also in case of permanent fault multiple measurements could be performed, in particular when different attempts of reenergizations are performed by the DSO/TSO.

5.1 Recommendations for future developments

This thesis work was focused in particular on the design of a prototype which could prove the possibility to combine multiple features on the same device and asses the effectiveness of the proposed location method. The prototype confirmed, even quite surprisingly, to be working as expected by design.

Nonetheless, some improvements may be desired. For instance, it was discussed that the accuracy of the location estimation greatly depends on the resolution of the timer. For this reason, a microcontroller supporting higher clock frequencies could be adopted in the next device revision.

Even if tests on MV cable were performed by injecting external signals or by supplying it with a low voltage, some further tests in a real MV/HV circuit should be undertaken. For instance, a MV feeder line, historically particularly affected by faults, especially if old, may be offered by the local DSO for a permanent test monitoring. Another actual possibility was offered by CESI, in Milan, for installing two devices on one of the resident HV test loops.

Another aspect is related to the development of the software which should run on a a remote elaboration unit. This will collect data sent by the Volos, compute the required algorithm for the localization, visualization of the PD patterns, temperatures, etc... The same elaboration unit should also perform statistical analysis and relate the occurrence of PDs with other network features when available or the occurrence of faults, thus gaining insight into the degeneration phenomenon and the factors affecting its fast evolution into a fault. The prototypal LoRa transceivers, shown in this thesis, may be used for the devices and for the PC/server communications.

Appendix A

Remote synchronization

A.1 Introduction

Wireless PD instruments, available on the market since few years [51], overcome the limitations of traditional sensors and devices, thus enabling to perform PD measurements without any direct connection to the part under test and without switching off the electrical systems. Moreover, the measurement system portability enables performing measurements in different test sites of the MV or HV circuit, allowing the localization of the PD source by exploiting the sensitivity and directionality of the sensor.

As discussed in the previous chapters, one of the most peculiar parameters for identifying the different PD activities relies on the analysis of the phase resolved PD (PRPD) pattern, where the amplitude of the PD pulses is plotted versus the phase angle of the supplying line voltage [38].

PDs generated by different sources generate different PD patterns, where the phase angle is crucial for discriminating the source of the PD phenomenon. This parameter allows identifying the presence of internal, surface or corona discharges. For instance, PD patterns of corona effects are usually featured as a group of dots across the maximum of the positive or negative voltage curve. An error of 30° in the PD acquisition could lead to an erroneous interpretation of critical surface PDs as in Fig. A.1a – indicating a serious defect on the MV/HV accessory - as corona effect Fig. A.1b, which can be usually classified as a not dangerous phenomenon. An accurate phase angle measurement is thus extremely important for PD detection and classification. The use of wireless PD diagnosis tools thus requires reliable ways for synchronizing the instrument with the AC power supply voltage of the equipment under test.

The advantages of performing online measurements by means of wireless PD instrument are basically two:

1. Measurements are performed with the electric system working in his normal operation, thus is not required to switch off the line avoiding money and time loss.

2. There is no galvanic connection to the system under test, so the activity is completely safe for the operator.

The frequency/phase reference is usually acquired by means of sensors integrated in the wireless PD instrument or by using external sources, such as current clamp, rogowski coil, CT or even light source. For instance, Wings sensors enable to sense both PDs as well as line synchronization and their installation do not involve any dangerous action. However, since their synchronization sensor captures the electric field associated with the line supplying voltage, in some circumstances the strength of this electric filed may be significantly low. In other cases the influence of other MV/HV equipments nearby may produce a resulting electric field which is not perfectly in phase with the accessory under test. Thus, in some circumstances, shielded cables do not allow an easy detection of the supplying voltage frequency signal without using specialized sensors, which have some disadvantages.

In fact, CT needs to be clamped across the earthing cable of the equipment, exposing the operator to some danger if a breakdown occurs while the CT is being clamped (i.e. a high voltage may be induced to the cable leads of the CT during a fault).

In some cases, especially inside substations, artificial light can be used as frequency source. In this case, the phase information it is not straightforward to be obtained since the phase shift depends by many factors (i.e. the transformer group producing the low voltage which feeds the light source). Furthermore, when PD measurements are performed on a termination without any load on the line, the capacitive current flowing on the line leads to a 90 degrees phase shift if a current clamp is used as synchronization source.

For these reasons a significant aspect is avoiding any phase shift between the PD measuring system and the voltage supplying the test section under test.

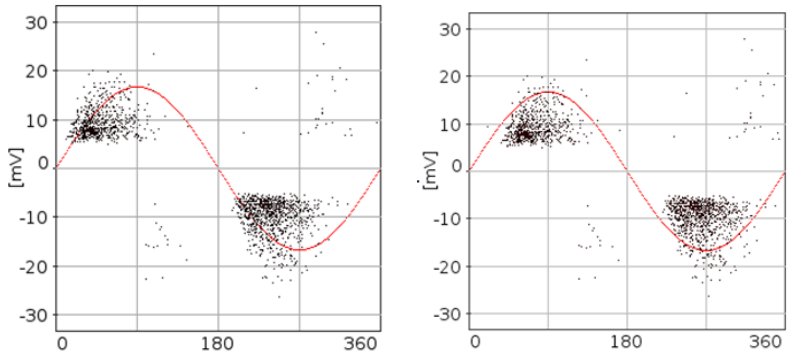

Figure A.1: (a) PD pattern of critical surface discharges; (b) same pattern affected by phase synchronization error mislead as corona discharges.

In this chapter, it is investigated the possibility to use, as reliable synchronization reference, the AC voltage feeding the line measured remotely on the same phase of the closest accessible substation [52, 53]. In the proposed method, a dedicated unit can be installed in few substations of the grid, acquiring the phase angle together with a precise time reference (i.e. derived from GPS). Where a Phasor Measurement Unit (PMU) [39, 54, 55] is already available at the substation, its time reference can be used, instead of using a separate GPS receiver and antenna. Phase angle and the precise time-stamp can be made accessible on a centralized synchronization server. In this way, PD measurements performed without proper synchronization can be corrected by correlating the time-stamp of the PD pulses with the synchronization server. The phase shift angle has to be calculated and may be compensated by the knowledge of the line length and load current. Different simulations in modeled real world test cases, showing various loading conditions and distances, are compared to actual measurements taken on the transmission network. In fact, thanks to a custom electronic device designed on purpose, henceforth called “PhaseCheck”, the voltage phase shift has been measured at the two ends of the considered HV overhead transmission lines. The measures on HV networks have been conducted with the support of the “Plants division” of Terna Rete Italia SpA (Italian Transmission System Operator) that has made available its facilities for validating the results obtained from the simulations and the “Phase Check” acquisitions. It is expected that the voltage phase shift in cable lines is greater than on overhead transmission lines. However, for this work, measurements have been performed on overhead lines only, due to the simpler authorization request process for accessing the substations.

A.2 Simulations

Initially, for evaluating the phase shift of the voltage in a transmission line, different EMTP simulations have been carried out. The first group of simulations was performed considering an overhead line and a cable line with a voltage rating of 220 kV. In order to evaluate the voltage wave propagation, the simulations were performed considering the following conditions:

- voltage generator with different voltage profiles at the two ends of the line (0.95 pu - 1 pu - 1.05 pu);
- line length of 100 km;
- power transmitted (70 MW - 150 MW - 200 MW);
- evaluation of the voltage wave propagation every 10 km and at the end of line.

The simulated overhead line consists of an ACSR conductor with diameter 31.5 mm (sections of aluminum 519,5 mm^2 and steel 65,80 mm^2), whose characteristics are shown in Table A.1. The cable used in the simulation is a three single phase aluminum conductors with Cross Linked Polyethylene (XLPE), cross section of 1000 mm^2 and designed to operate at a rated voltage of 245 kV. The main features and data of the cable line are shown in Table A.2 and Table A.3.

Primary parameters			
Positive sequence		Zero sequence	
r $[\Omega/km]$	5.487e-2	r_0 $[\Omega/km]$	3.089e-1
l $[H/km]$	1.274e-3	l_0 $[H/km]$	9.833e-2
c $[F/km]$	9.162e-9	$c_0[F/km]$	5,845e-9

Secondary parameters	
Surge impedance $[\Omega]$	374.637
Wavelength $[km]$	5840.6
Propagation speed $[km/s]$	292030
Complex propagation constant $[rad/km]$	0.0001+j 0.0011

Table A.1: ACSR Transmission line Data.

Conductor cross section	Al, 1000 mm^2
Insulation	XLPE, 19.1 mm
XLPE Relative Permittivity	2.3
Metallic sheath	Al, 1.2 mm
Plastic sheath	HDPE, 4 mm
Maximum working voltage	245 kV
Conductor DC resistance	29.1 $m\Omega/km$
Conductor AC resistance	40.51 $m\Omega/km$
Inductance per phase	0.382 mH/km
Capacitance per phase	0.205 $\mu F/km$
Positive sequence resistance	0.04053 Ω/km
Positive sequence reactance	0.119 Ω/km

Table A.2: Cable material properties.

Inductance L	323.2 $\mu H/km$
Capacitance C	154,4 nF/km
Surge impedance Z_C	47,525 Ω
Wavelength λ	2781.6 km
Propagation speed v	139080 km/s
Complex propagation constant γ	0.0004+0.0023 rad/km

Table A.3: Cable line data.

The simulation results are shown in Table A.4 and Table A.5, for the overhead and the cable line. They show, as it can be expected, the increase of the phase shift for increasing supplied power values, with different voltage rating for equal line length.

A comparison between the overhead and cable lines simulations shows that, per equal length and power supplied, the voltage wave phase shift is comparable. The higher reactive power engaged in cable line allows to partly compensate the voltage wave phase shift. From the simulation results, it can be noted that the maximum phase shift, in these conditions, on a HV line is around 10°. If PD measurements are acquired and phase sync corrected with such phase reference, an error up to 15° does not usually lead to misleading interpretation in the analysis of the PD pattern. Even if it is possible to correct this phase shift by the knowledge of the line length and the load current, in most of the cases this will not be necessary.

Overhead transmission line	250 MW		500 MW		1000 MW	
	$\delta[°]$ 100km	$\delta[°]$ 10km	$\delta[°]$ 100km	$\delta[°]$ 10km	$\delta[°]$ 100km	$\delta[°]$ 10km
380kV	2,72	0,27	5,35	0,53	10,47	1,06
Overhead transmission line	50 MW		100 MW		200 MW	
	$\delta[°]$ 100km	$\delta[°]$ 10km	$\delta[°]$ 100km	$\delta[°]$ 10km	$\delta[°]$ 100km	$\delta[°]$ 10km
220kV	2,42	0,23	4,74	0,47	9,25	0,94
Overhead transmission line	50 MW		100 MW		200 MW	
	$\delta[°]$ 100km	$\delta[°]$ 10km	$\delta[°]$ 100km	$\delta[°]$ 10km	$\delta[°]$ 100km	$\delta[°]$ 10km
150kV	5,09	0,51	7,53	0,76	9,91	1,01

Table A.4: Overhead transmission line simulation results.

Cable line	50 MW		100 MW		200 MW	
	$\delta[°]$ 100km	$\delta[°]$ 10km	$\delta[°]$ 100km	$\delta[°]$ 10km	$\delta[°]$ 100km	$\delta[°]$ 10km
220kV	3,66	0,27	6,08	0,49	10,73	0,94

Table A.5: Cable line simulation results.

A.2.1 Simulation of specific HV lines

In order to further understand how the transmission line determines a voltage phase shift, other simulations in PSCAD of different overhead transmission lines actually operating in Sicily, Italy, have been carried out. The first aim of these simulations is to see whether the phase shift introduced by standard operating conditions can be meaningful for PD diagnosis. The second aim is to provide, after validation with other measuring systems, a look up table to assess the phase shift or correct other available measures.

For evaluating the voltage phase shift introduced by a transmission line, the simulations were conducted on three overhead transmission lines with a rating voltage of 220 kV and 380 kV. The overhead transmission lines considered for the simulations consist in an ACSR conductor with diameter 31.5 mm (aluminum section 519.5 mm^2/steel section 65.80 mm^2). Fig. A.2a shows the 220 kV overhead transmission lines, in particular the lines from Bellolampo to Caracoli substations (BLL-CAR) and from Bellolampo to Partinico substations (BLL- PRT). The 380kV overhead transmission line (red line) from Chiaramonte Gulfi to Priolo stations (CHI-PRI) is shown in Fig. A.2b.

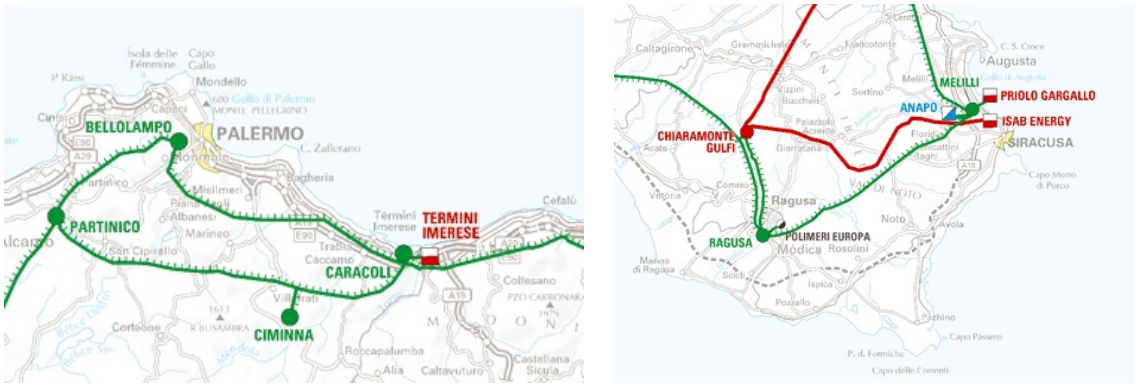

(a) (b)

Figure A.2: 220 kV overhead transmission lines (a) and 380 kV (b).

The simulations were performed considering the actual line length and the power level transmitted detected on site during measurements. Lines specifications were provided by the Italian TSO and are listed in Table A.6.

Line Parameter	BLL-CAR	BLL-PRT	CHI-PRI
Rating Voltage [kV]	220	220	380
r $[\Omega/km]$	0.549e-4	0.549e-4	0.182e-4
XL $[\Omega/km]$	0.400e-3	0.401e-3	0.270e-3
XC $[M\Omega \cdot km]$	347.961	347.876	233.843
ro $[\Omega/km]$	0.191e-3	0.3170e-3	0.251e-3
XL0 $[\Omega/km]$	0.100e-2	0.132e-2	0.110e-2
XC0 $[M\Omega \cdot km]$	452.859	540.443	440.414

Table A.6: Characteristic parameters of the overhead lines.

The simulations were conducted using the Bergeron model that is based on a distributed LC-parameter traveling wave line model, with lumped resistance. It represents the L and C elements of a PI Section in a distributed manner (i.e. it does not use lumped parameters). It is roughly equivalent to using an infinite number of PI Sections, except that the resistance is lumped (1/2 in the middle of the line, 1/4 at each end).

Simulations are reported in Table A.7a, which show that line CHI-PRI determines a higher voltage phase-shift with a higher transmitted power. In a transmission system with greater lines lengths and significant amounts of transported power, the phase error may become quite significant. For example, the simulations show that for a transmission line with the same characteristics and the same transmitted power of CHI-PRI, but with a length of 200 km, the voltage phase shift introduced by the

line would be approximately 13.72°. This phase error magnitude is quite high and could lead to a wrong assessment of the PD patterns.

Different simulations have been performed with the real geometric layout of the conductors. In this way, the simulator computes the constant values from the geometric layout by using the Bergeron model. The configuration layout for the transmission lines BLL-CAR and BLL-PRT at the rating voltage of 220 kV is a double three phase conductor in a vertical tower as shown in Fig. A.3a. In this configuration, each phase can carry 500 A with a three phase nominal power of 200 MVA. The geometric layout of the 380kV transmission line CHI-PRI consists in three conductors per phase in delta tower, as shown in Fig. A.3. In this configuration, each phase can carry 1500 A with a three phase nominal power of 1000 MVA.

(a) (b)

Figure A.3: (a) Double three phase conductor in vertical tower at voltage rating of 220kV; (b) three phase transmission line at three conductors per phase in delta tower at voltage rating of 380kV.

A greater power transport determines a higher current flow which results in a greater voltage phase shift. Table A.7b shows transmitted power and relevant phase shift for comparable line lengths. The simulations were performed considering the actual active and reactive power transit measured on site. The large reactive power transit in the case of the line BLL-PRT was due to a particular operating condition of the electrical system.

Line	Length [km]	Transmitted power [MW]	Reactive power [MVAR]	Phase shift [°]
BLL-CAR	50.9	48	-6.09	1.17°
BLL-PRT	26	45	-45	0.70°
CHI-PRI	60.9	690	-16.03	4.47°

(a)

Line	Length [km]	Transmitted power [MW]	Reactive power [MVAR]	Phase shift [°]
BLL-CAR	50.9	48	-7,07	1.05°
BLL-PRT	26	45	-45	0.68°
CHI-PRI	60.9	690	-10.84	4.11°

(b)

Table A.7: Simulation results with manually entered line parameters (a) and by using the actual geometric layout. (b)

A.3 Hardware

As anticipated, measurements on the three aforementioned lines have been performed. For this purpose, another custom electronic board, the PhaseCheck, was designed for comparing the phase angle between two points of a transmission line. The simplified block diagram is shown in Figure A.4.

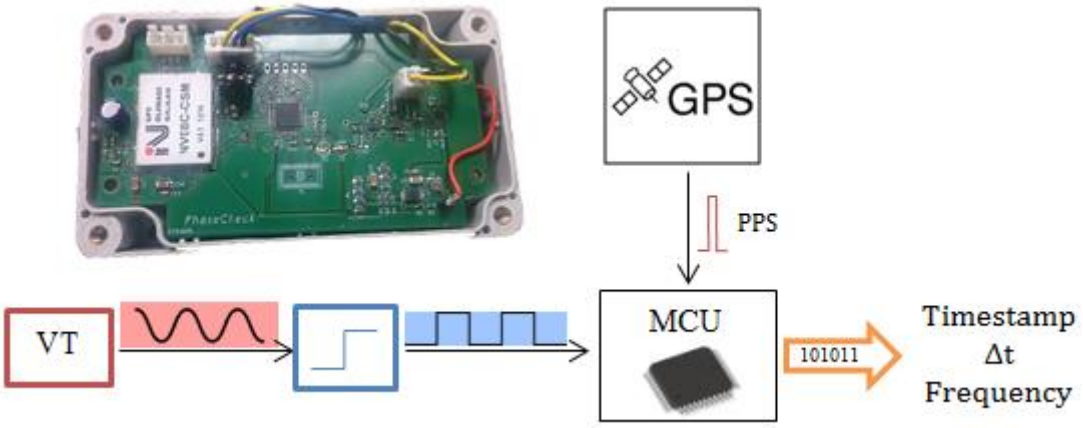

Figure A.4: Simplified block diagram of PhaseCheck and picture of the device.

The circuit design is made of an analog front-end that is connected to the voltage transformer (TV) output in the substation; this signal (in the range of 100V) is converted to a square wave by a diode clamping circuit. A GPS receiver and its

amplified antenna are used as time-reference circuit: when the GPS receiver acquires the minimum number of satellites, a 1-second pulse (PPS) is generated and acquired as interrupt by the 8-bit microcontroller ATMEGA8A (henceforth MCU). In the interrupt routine, the MCU calculates by means of an internal counter (1µs of resolution) the time difference between the received PPS and the next rising-edge of the square wave obtained from the AC voltage of the TV. For the sake of clarity, the same principle can be performed by using a 2-channel oscilloscope like in Figure A.5. It should be noted in blue the square wave obtained from the TV output, while the PPS generated by the GPS receiver of the PhaseCheck is depicted in yellow. The time-difference Δt between the rising-edge of the PPS and the next rising-edge of the square wave can be easily obtained.

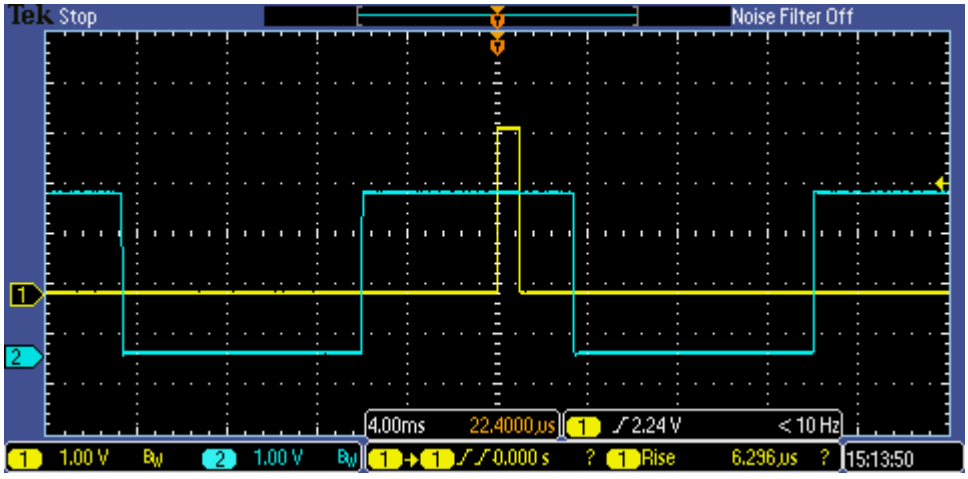

Figure A.5: Oscilloscope example of the measurement performed by the PhaseCheck.

The time-stamp and the value of the counter, representing the Δt, are locally stored and sent by a serial link to the PC. The frequency of the square wave is also calculated and transmitted to the PC.

It can be noted that PhaseCheck and Volo share part of the design and many components. It is actually possible to integrate PhaseCheck capabilities into the Volo.

A.4 Measurements

Through the collaboration with the "Plants division" of Terna Rete Italia SpA, the measurements on the overhead transmission lines have been carried out and the comparison with the simulation results have been done. In order to calculate the phase shift between two points in a transmission line, two twin PhaseCheck units

were used, each placed at one end of the line and connected to the respective TV on the same HV phase. The resulting files were saved on the two laptop computers connected to the PhaseCheck units at the two sites and then processed at the end of the measurement session. For the same time-stamp value, the difference of the counters in the two files was obtained, hence the resulting phase shift.

The measurements evaluated the voltage phase shift introduced by the transmission line in standard operating conditions for one particular phase. The results of the measurements are shown in Table A.9.

For the 50.9 km long 220 kV line BLL-CAR with a load of 48 MW the measured phase shift between the two ends of the line was 1.03° degrees. The simulated model of the line gives a result of 1.05°, in close accordance to the experimental results.

Line BLL-PRT was measured at the two ends, resulting in a phase shift of 0.74°, while the simulation with actual geometric layout provided 0.68°.

The other measurements were performed on the 60.9 km long 380 kV line CHI-PRI with a load of 690 MW. The phase shift in this case was of 4.24° while the simulated line model provided 4.11°. Also in this case, the experimental results are in good accordance with the simulation ones.

In Table A.8 the results of the measurement campaign are shown, and in Table A.9 simulations and measurements results are finally compared. From simulations, considering the geometric layout of the lines, the absolute error with respect to the measurement performed by the PhaseCheck turns to be below 0.23° in the worst case.

Line	Length [km]	Transmitted power [MW]	Reactive power [MVAR]	Phase shift [degrees]
BLL-CAR	50.9	48	-7,07	1.03°
BLL-PRT	26	45	-45	0.74°
CHI-PRI	60.9	690	-10.84	4.24°

Table A.8: Simulation results with geometric layout.

Line	Phase Check measurements	Simulation Manual Data Entry		Simulation Geometric Layout	
	phase-shift	phase-shift	Error	phase-shift	Error
BLL-CAR	1.03°	1.17°	0.14°	1.05°	0.02°
BLL-PRT	0.74°	0.70°	0.04°	0.68°	0.06°
CHI-PRI	4.24°	4.47°	0.23°	4.11°	0.13°

Table A.9: Comparison of the simulated and measured phase shift vaules.

A.5 Discussion and conclusion

Although the physics of the described phenomenon is well known, that is the voltage phasor angles increase with increasing active power being transmitted, the discussion presented in this chapter provides the basis for the implementation of a novel architecture enabling the synchronization by means of a centralized synchronization server and low cost phase measuring instruments.

Transmission lines up to 100 km were simulated in different load conditions and the resulting phase shift obtained. It was shown, in such cases, that the maximum obtainable phase shift is below 11°, which is minor than the phase shift error usually allowable by a PD expert who is analyzing the measurement in order to provide a reliable diagnosis about the system under test. This error is usually acceptable below 15° in real case PD measurements. On the other hand, the phase shift can be easily compensated by knowing the length of the line to the nearest monitored substation and the current load.

Furthermore, other simulations showed that phase shifts on the two ends of three studied transmission lines is usually far less than the maximum allowed error of 15°. Thus the average distance between the substations where to install the PhaseChecks could be chosen in order to have a phase shift error below the acceptable value. However, the knowledge of the electrical distance between the location where PD measurement is performed and the nearest PhaseCheck equipped substation, together with the information of current load, eventually the phase shift can be compensated.

A custom device for measuring the phase shift between two points of a transmission line was designed and used for performing measurements in three HV lines. The results agree with the simulations.

In Fig. A.6 a proposed overall architecture of the wireless PD diagnosis system using the Phase Check and the look up table is shown. The PhaseCheck device acquires the voltage phase angle at one end of the line and the absolute time reference by GPS; this data is sent to the Look Up Table Server via a internet gateway. When a PD measurements is acquired with a not reliable synchronization, the server calculates the phase shift by the knowledge of the line length between the closest PhaseCheck and where the measurement was taken. If the operating conditions are available, the server could also perform a simulation of the line and provide a more precise phase shift. In this way, the PD measurement in a different sites can be corrected to obtain a PD pattern with an accurate phase angle.

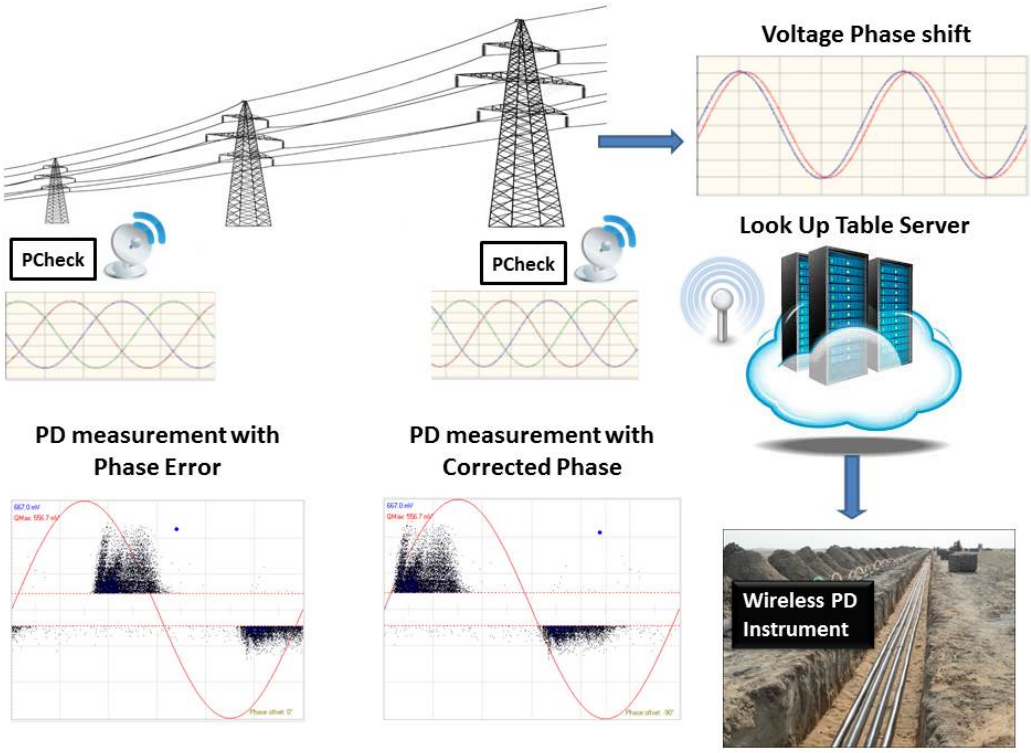

Figure A.6: Voltage phase shift compensation in PD measurement through Phase check and Look up tables.

Bibliography

[1] IEEE Power System Relaying Committee. *IEEE Guide for Determining Fault Location on AC Transmission and Distribution Lines*. The Institute of Electrical and Electronics Engineers, Inc, Jan 2015. 1, 1.2.1, 1.2.1, 1.3.4, 1.3.4.4

[2] Murari Mohan Saha, Jan Jozef Izykowski, and Eugeniusz Rosolowski. *Fault location on power networks*. Springer Science & Business Media, 2009. 256 cit. 1, 1.2.1, 1.3.4.5

[3] Kunjin Chen, Caowei Huang, and Jinliang He. Fault detection, classification and location for transmission lines and distribution systems: a review on the methods. *High Voltage*, 1:25–33(8), April 2016. 1, 1.1, 1.2

[4] M. Kezunovic. Smart fault location for smart grids. *IEEE Transactions on Smart Grid*, 2(1):11–22, March 2011. 159 cit. 1, 1.2

[5] J.B. Roberts, G. Benmouyal, and D. Tziouvaras. Multi-ended fault location system, July 3 2001. 1.1

[6] D. A. Tziouvaras, J. B. Roberts, and G. Benmouyal. New multi-ended fault location design for two- or three-terminal lines. In *Developments in Power System Protection, 2001, Seventh International Conference on (IEE)*, pages 395–398, 2001. 104 cit. 1.1, 1.2, 1.2.1

[7] N. Kashyap, C. W. Yang, S. Sierla, and P. G. Flikkema. Automated fault location and isolation in distribution grids with distributed control and unreliable communication. *IEEE Transactions on Industrial Electronics*, 62(4):2612–2619, April 2015. 1.2

[8] S. Das, S. Santoso, A. Gaikwad, and M. Patel. Impedance-based fault location in transmission networks: theory and application. *IEEE Access*, 2:537–557, 2014. 9 cit. 1.2, 1.2.1, 1.2.1

[9] Y. Dong, C. Zheng, and M. Kezunovic. Enhancing accuracy while reducing computation complexity for voltage-sag-based distribution fault location. *IEEE Transactions on Power Delivery*, 28(2):1202–1212, April 2013. 1.2

[10] T. Takagi, Y. Yamakoshi, J. Baba, K. Uemura, and T. Sakaguchi. A new algorithm of an accurate fault location for ehv/uhv transmission lines: Part ii - laplace transform method. *IEEE Transactions on Power Apparatus and Systems*, PAS-101(3):564–573, March 1982. 60 cit. 1.2.1

[11] T. Takagi, Y. .. Yamakoshi, M. Yamaura, R. Kondow, and T. Matsushima. Development of a new type fault locator using the one-terminal voltage and current data. *IEEE Transactions on Power Apparatus and Systems*, PAS-101(8):2892–2898, Aug 1982. 496 cit. 1.2.1, 1.2.1

[12] L. Eriksson, M. M. Saha, and G. D. Rockefeller. An accurate fault locator with compensation for apparent reactance in the fault resistance resulting from remore-end infeed. *IEEE Transactions on Power Apparatus and Systems*, PAS-104(2):423–436, Feb 1985. 300 cit. 1.2.1

[13] Jan Izykowski and Politechnika Wroclawska. *Fault location on power transmission lines*. Oficyna Wydawnicza Politechniki Wroclawskiej, 2008. 1.2.1

[14] K. Zimmerman and D. Costello. Impedance-based fault location experience. In *58th Annual Conference for Protective Relay Engineers, 2005.*, pages 211–226, April 2005. 1.2.1

[15] Rastko Živanović. 'evaluation of transmission line fault-locating techniques using variance-based sensitivity measures. In *Proc. 16th Power Syst. Comput. Conf*, pages 1–6, 2008. 1.2.1

[16] Z. Q. Bo, G. Weller, and M. A. Redfern. Accurate fault location technique for distribution system using fault-generated high-frequency transient voltage signals. *IEE Proceedings - Generation, Transmission and Distribution*, 146(1):73–79, Jan 1999. 1.3

[17] E. O. Schweitzer, A. Guzmán, M. V. Mynam, V. Skendzic, B. Kasztenny, and S. Marx. Locating faults by the traveling waves they launch. In *Protective Relay Engineers, 2014 67th Annual Conference for*, pages 95–110, March 2014. 1.3, 1.3.2, 1.3.3, 1.3.3

[18] E. O. Schweitzer, A. Guzmán, M. V. Mynam, V. Skendzic, B. Kasztenny, and S. Marx. A new traveling wave fault locating algorithm for line current differential relays. In *Developments in Power System Protection (DPSP 2014), 12th IET International Conference on*, pages 1–6, March 2014. 1.3

[19] M. Korkali, H. Lev-Ari, and A. Abur. Traveling-wave-based fault-location technique for transmission grids via wide-area synchronized voltage measurements. *IEEE Transactions on Power Systems*, 27(2):1003–1011, May 2012. 1.3

[20] Krzysztof Glik, Desire Dauphin Rasolomampionona, and Ryszard Kowalik. Detection, classification and fault location in hv lines using travelling waves. *Przegląd Elektrotechniczny (Electrical Review)*, 88(1A):269–275, 2012. 1.3

[21] N. Fischer, V. Skendzic, R. Moxley, and J. Needs. Protective relay traveling wave fault location. In *Developments in Power Systems Protection, 2012. DPSP 2012. 11th International Conference on*, pages 1–3, April 2012. 1.3

[22] A. Borghetti, M. Bosetti, C. A. Nucci, M. Paolone, and A. Abur. Integrated use of time-frequency wavelet decompositions for fault location in distribution networks: Theory and experimental validation. *IEEE Transactions on Power Delivery*, 25(4):3139–3146, Oct 2010. 1.3

[23] S. L. Zimath, M. A. Ramos, J. S. Filho, J. M. Beck, and N. Mueller. Traveling wave-based fault location experiences. In *Protective Relay Engineers, 2010 63rd Annual Conference for*, pages 1–7, March 2010. 1.3

[24] Harry Lee. Development of an accurate transmission line fault locator using the global positioning system satellites. *Spring Meeting of the Canadian Electrical Association*, 1993. 1.3

[25] H. Lee and A. M. Mousa. Gps travelling wave fault locator systems: investigation into the anomalous measurements related to lightning strikes. *IEEE Transactions on Power Delivery*, 11(3):1214–1223, Jul 1996. 1.3

[26] Edmund O Schweitzer, Bogdan Kasztenny, Armando Guzmán, Veselin Skendzic, and Mangapathirao V Mynam. Speed of line protection–can we break free of phasor limitations? In *41st Annual Western Protective Relay Conference, Spokane, Washington USA*, 2014. 1.3

[27] Bhag Singh Guru and Hüseyin R Hiziroglu. *Electromagnetic field theory fundamentals*. Cambridge university press, 2004. 1.3.2

[28] Lou Van der Sluis. *Transients in power systems*, volume 2001. Wiley New York, 2001. 1.3.2

[29] Edith Clarke. *Circuit Analysis of AC Power Systems...li*, volume 2. J. Wiley & sons, Incorporated, 1950. 1.3.3

[30] F. H. Magnago and A. Abur. Fault location using wavelets. *IEEE Transactions on Power Delivery*, 13(4):1475–1480, Oct 1998. 1.3.4.2

[31] Iec international standard 60270. high voltage test techniques - partial discharge measurements, 2000. 2.1, 2.2.5

[32] Teo Brescia, Sergio Bruno, Massimo La Scala, Silvia Lamonaca, Giuseppe Rotondo, and Ugo Stecchi. A fuzzy-logic approach to preventive maintenance of critical power transformers. In *20th International Conference on Electricity Distribution, CIRED*, pages 1–5, 2009. 2.1

[33] G. C. Montanari. Partial discharge measurements: becoming a fundamental tool for quality control and risk assessment of electrical systems? In *Conference Record of the 2006 IEEE International Symposium on Electrical Insulation*, pages 281–285, June 2006. 2.2

[34] PHF Morshuis. Partial discharge mechanisms in voids related to dielectric degradation. *IEE Proceedings-Science, Measurement and Technology*, 142(1):62–68, 1995. 2.2

[35] Len A Dissado and John C Fothergill. *Electrical degradation and breakdown in polymers*, volume 9. IET, 1992. 2.2.1, 2.2.2, 1

[36] Y Takahashi, S Kato, and Shigeo Kobayashi. Discharge voltage of dielectric gaps and the generalized secondary ionization coefficient γ of the dielectric cathode. In *Properties and Applications of Dielectric Materials, 1988. Proceedings., Second International Conference on Properties and Applications of*, pages 550–553. IEEE, 1988. 2.2.1

[37] GA Dawson and William Paul Winn. A model for streamer propagation. *Zeitschrift für Physik*, 183(2):159–171, 1965. 2.2.2

[38] Claude Hudon and Mario Belec. Partial discharge signal interpretation for generator diagnostics. *IEEE Transactions on Dielectrics and Electrical Insulation*, 12(2):297–319, 2005. 133 cit. 2.3, A.1

[39] J. De La Ree, V. Centeno, J. S. Thorp, and A. G. Phadke. Synchronized phasor measurement applications in power systems. *IEEE Transactions on Smart Grid*, 1(1):20–27, June 2010. 450. 2.3, A.1

[40] S Das and P Purkait. ϕ-qn pattern analysis for understanding partial discharge phenomena in narrow voids. In *Power and Energy Society General Meeting-Conversion and Delivery of Electrical Energy in the 21st Century, 2008 IEEE*, pages 1–7. IEEE, 2008. 2.3

[41] FH Kreuger, E Gulski, and A Krivda. Classification of partial discharges. *IEEE Transactions on Electrical Insulation, 28 (6)[see also IEEE Transactions on Dielectrics and Electrical Insulation]*, 1993. 2.4

[42] Rainer Patsch, Farhad Berton, and Djamel Benzerouk. Pd-source identification and characterization on the basis of pulse shape analysis. In *Electrical Insulation and Dielectric Phenomena, 2002 Annual Report Conference on*, pages 728–731. IEEE, 2002. 2.4

[43] Raji Ambikairajah, Bao Toan Phung, Jayashri Ravishankar, and Trevor Blackburn. Spectral features for the classification of partial discharge signals from selected insulation defect models. *IET Science, Measurement & Technology*, 7(2):104–111, 2013. 2.4

[44] C. Zachariades, R. Shuttleworth, R. Giussani, and R. MacKinlay. Optimization of a high-frequency current transformer sensor for partial discharge detection using finite-element analysis. *IEEE Sensors Journal*, 16(20):7526–7533, October 2016. 2.6.1

[45] F. P. Mohamed, W. H. Siew, J. J. Soraghan, S. M. Strachan, and J. McWilliam. Partial discharge location in power cables using a double ended method based on time triggering with gps. *IEEE Transactions on Dielectrics and Electrical Insulation*, 20(6):2212–2221, December 2013. 3

[46] PCJM Van der Wielen. *On-line detection and location of partial discharges in medium-voltage power cables*. PhD thesis, Technische Universiteit Eindhoven, 2005. 3

[47] A. Di Stefano, R. Candela, and G. Fiscelli. A partial discharge acquisition system comprising a capacitive coupling electric field sensor, November 19 2015. WO Patent App. PCT/EP2014/060,141. 3.1

[48] P. Wagenaars, P. A. A. F. Wouters, P. C. J. M. van der Wielen, and E. F. Steennis. Accurate estimation of the time-of-arrival of partial discharge pulses in cable systems in service. *IEEE Transactions on Dielectrics and Electrical Insulation*, 15(4):1190–1199, August 2008. 3.2.3

[49] C.A. Hornbuckle. Fractional-n synthesized chirp generator, November 20 2008. US Patent App. 12/122,635. 3.4.5

[50] H. G. S. Filho, J. P. Filho, and V. L. Moreli. The adequacy of lorawan on smart grids: A comparison with rf mesh technology. In *2016 IEEE International Smart Cities Conference (ISC2)*, pages 1–6, Sept 2016. 3.4.5

[51] R. Candela, E. R. Sanseverino, and P. Romano. Partial discharge on-line measures in cable's epr insulation. In *Proc. Annual Report Conf. Electrical Insulation and Dielectric Phenomena CEIDP '04*, pages 470–473, October 2004. A.1

[52] V. L. Vigni, A. Madonia, E. R. Sanseverino, P. Romano, and R. Candela. Overcoming synchronization issues in wireless technology partial discharge measurement. In *2016 IEEE 16th International Conference on Environment and Electrical Engineering (EEEIC)*, pages 1–4, June 2016. A.1

[53] A. Madonia, V. L. Vigni, E. R. Sanseverino, P. Romano, F. Viola, and R. Candela. Remote voltage synchronization for wireless partial discharge diagnostics. In immer, editor, *2016 IEEE International Conference on Dielectrics (ICD)*, volume 2, pages 947–950, July 2016. A.1

[54] V. Terzija, G. Valverde, D. Cai, P. Regulski, V. Madani, J. Fitch, S. Skok, M. M. Begovic, and A. Phadke. Wide-area monitoring, protection, and control of future electric power networks. *Proceedings of the IEEE*, 99(1):80–93, January 2011. A.1

[55] A. Bose. Smart transmission grid applications and their supporting infrastructure. *IEEE Transactions on Smart Grid*, 1(1):11–19, June 2010. A.1